HHS Public Access

Author manuscript

Phys Med Biol. Author manuscript; available in PMC 2016 April 21.

Published in final edited form as:

Phys Med Biol. 2015 April 21; 60(8): R155–R209. doi:10.1088/0031-9155/60/8/R155.

The physics of proton therapy

Wayne D Newhauser[1,2,3] and **Rui Zhang**[1,2]

[1]Medical Physics Program, Department of Physics and Astronomy, Louisiana State University, 202 Nicholson Hall, Baton Rouge, LA, 70803, USA

[2]Mary Bird Perkins Cancer Center, 4950 Essen Lane, Baton Rouge, LA, 70809, USA

Abstract

The physics of proton therapy has advanced considerably since it was proposed in 1946. Today analytical equations and numerical simulation methods are available to predict and characterize many aspects of proton therapy. This article reviews the basic aspects of the physics of proton therapy, including proton interaction mechanisms, proton transport calculations, the determination of dose from therapeutic and stray radiations, and shielding design. The article discusses underlying processes as well as selected practical experimental and theoretical methods. We conclude by briefly speculating on possible future areas of research of relevance to the physics of proton therapy.

Keywords

proton therapy; interaction mechanism; transport; Monte Carlo; dosimetry; shielding

1. Introduction

The history of proton therapy began in 1946 when Robert Wilson published a seminar paper in which he proposed to use accelerator-produced beams of protons to treat deep-seated tumors in humans (Wilson, 1946). In that paper, he explained the biophysical rationale for proton therapy as well as the key engineering techniques of beam delivery. In 1954, the first human was treated with proton beams at the Lawrence Berkeley Laboratory (Lawrence *et al*, 1958). In 1962, specialized radiosurgical proton treatments commenced at the Harvard Cyclotron Laboratory (Kjellberg *et al*, 1962a; Kjellberg *et al*, 1962b), followed in the mid 1970s by treatments for ocular cancers (Gragoudas*et al*, 1982) and larger tumors (Koehler *et al*, 1977). Physicists at Harvard, collaborating with clinical colleagues at Massachusetts General Hospital, the Massachusetts Eye and Ear Infirmary, and elsewhere, developed much of the physics and technology needed to treat patients with proton beams safely and effectively. Remarkably, the research and development program at Harvard continued for more than 40 years (Wilson, 2004). During the same period, physicists elsewhere were developing other key technologies, including accelerators, magnetically scanned beams,

[3]Corresponding author: Department of Physics and Astronomy, Louisiana State University, Baton Rouge, LA, USA *Tel.*: 225-578-2762; *Fax*: 225-215-1376 newhauser@lsu.edu (W. Newhauser)..

treatment planning systems, computed tomographic imaging (CT), and magnetic resonance imaging.

The widespread adoption of proton therapy has been slow in comparison to, for example, intensity-modulated photon therapy. There are several reasons for this slow adoption of proton therapy, including technical difficulty, cost, and lack of evidence of cost-competitiveness. Commercial proton delivery systems had been contemplated for decades before they finally appeared in 2001 after overcoming considerable difficulties. The cost of proton therapy equipment remains much higher than that of comparable conventional photon therapy equipment; the long-anticipated economies of scale have not, as yet, materialized. Even in times of relative prosperity, the allocation of scarce resources to proton therapy has been constrained by relatively sparse evidence of its cost-competitiveness and cost-effectiveness (Goitein and Jermann, 2003; Peeters *et al*, 2010; Lievens and Pijls-Johannesma, 2013).

Despite these obstacles, much progress has been made. Today there are 10 proton therapy centers in operation in the United States and 38 centers worldwide (PTCOG, 2013). The Particle Therapy Cooperative Group (PTCOG) reported that at least 93,895 patients had been treated worldwide by March, 2013 (PTCOG, 2013). The proton therapy community has stepped up efforts to conduct clinical trials that compare outcomes after proton therapy with those after other advanced technology radiation therapies (Duttenhaver *et al*, 1983; Shipley *et al*, 1995; Desjardins *et al*, 2003; Zietman *et al*, 2010).

The central rationale for proton therapy is its superior spatial dose distribution in the patient. In recent years, the advantage of protons over photons in providing a highly conformal and uniform dose to a tumor has been largely diminished by advances in photon therapies, such as intensity-modulated photon therapy and volumetric arc therapy (Weber *et al*, 2009). However, the relative advantage of proton therapy in sparing normal tissues has never been more apparent or important; in the United States, approximately 65% of adults and 80% of children survive 5 years after their cancer diagnosis (Valdivieso *et al*, 2012). About half of cancer patients receive radiotherapy as part of their treatment. Recent studies reported that the incidence of treatment-related morbidity, including second cancers, cardiovascular disease, fertility complications, and other late effects, is alarmingly high in long-term survivors of cancer (Wilson *et al*, 2005; Carver *et al*, 2007; Armstrong *et al*, 2009; Merchant, 2009; Sauvat *et al*, 2009; Newhauser and Durante, 2011; Olch, 2013). Presently, about 3% of the U.S. population are cancer survivors, corresponding to 11 million people, a figure projected to grow to 18 million by 2022 (de Moor *et al*, 2013) For these reasons, there is increasing interest in exploiting the tissue-sparing capabilities inherent to proton therapy to reduce the burden of treatment-related complications on patients and the healthcare system. An understanding of the physics and biology of radiogenic late effects from proton therapy has started to emerge in the literature in the last decade.

This paper reviews the basic, essential physics underlying proton therapy. The literature includes excellent reviews of various aspects of proton therapy physics, most notably the comprehensive works of Chu *et al.* (1993), and also those of Bonnett (Bonnett, 1993), Pedroni *et al.* (1995), Brahme (2004), Lomax (2009), Coutrakon (2007), and Schardt and

Elsasser (2010) In addition, several reports (ICRU, 1998, 2007) and textbooks (Scharf, 1994; Breuer and Smit, 2000; DeLaney and Kooy, 2008; Linz, 2012; Paganetti, 2012; Ma and Lomax, 2013) have covered various aspects of proton therapy physics. In recent years, many textbooks dealing with general radiation oncology have included relevant chapters on proton therapy (Van Dyk, 1999; Halperin *et al*, 2008; Pawlicki *et al*, 2011). Many of the older works on proton therapy have withstood the test of time and remain excellent literature resources of continued relevance. However, in this review we mainly focus on the well-established basic physics of proton therapy and on selected advances from the last 15 years or so that are important in clinical proton therapy. In choosing advances to cover in this review, considerable selectivity was necessary because of the huge expansion of the proton therapy literature, especially in recent years. To the authors of the many studies that we were not able to mention in this review because of space limitations, we apologize and we appreciate your understanding.

2. Proton interaction mechanisms

In this section, we briefly review the predominant types of interactions of protons in matter and why they are important. Figure 1 illustrates several mechanisms by which a proton interacts with an atom or nucleus: Coulombic interactions with atomic electrons, Coulombic interactions with the atomic nucleus, nuclear reactions, and Bremsstrahlung. To a first-order approximation, protons continuously lose kinetic energy via frequent inelastic Coulombic interactions with atomic electrons. Most protons travel in a nearly straight line because the proton mass is 1832 times greater than that of an electron. In contrast, a proton passing close to the atomic nucleus experiences a repulsive elastic Coulombic interaction which, owing to the large mass of the nucleus, deflects the proton from its original straight-line trajectory. Inelastic nuclear reactions between protons and the atomic nucleus are less frequent but, in terms of the fate of an individual proton, have a much more profound effect. In a nuclear reaction, the projectile proton enters the nucleus; the nucleus may emit a proton, deuteron, triton, or heavier ion or one or more neutrons. Finally, proton Bremsstrahlung is theoretically possible, but at therapeutic proton beam energies this effect is negligible. Table 1 summarizes the proton interaction types, interaction targets, principal ejectiles, influence on the proton beam, and dosimetric manifestations. We review these interaction mechanisms, except proton Bremsstrahlung, in the following sections.

2.1 Energy loss rate

The energy loss rate of ions, or linear stopping power, is defined as the quotient of dE and dx, where E is the energy and x is the distance. It is frequently more convenient to express the energy loss rate in a way that is independent of the mass density; the mass stopping power is defined as

$$\frac{S}{\rho} = -\frac{\mathrm{d}E}{\rho \mathrm{d}x}, \quad (1)$$

where ρ is the mass density of the absorbing material. Please note that stopping power is defined for a beam, not a particle.

The energy loss rate may be described by several mathematical formulae. The simplest, yet still remarkably accurate, formula is based on the Bragg-Kleeman (BK) Rule (Bragg and Kleeman, 1905), which was originally derived for alpha particles, and is given by

$$\frac{S}{\rho} = -\frac{\mathrm{d}E}{\rho \mathrm{d}x} \approx -\frac{E^{1-p}}{\rho \alpha p}, \quad (2)$$

where ρ is the mass density of the material, α is a material-dependent constant, E is the initial energy of the proton beam, and the exponent p is a constant that takes into account the dependence of the proton's energy or velocity. Values of α and p may be obtained by fitting to either ranges or stopping power data from measurements or theory.

A more physically complete theory, developed by Bohr (Bohr, 1915), is based on calculation of the momentum impulse of a stationary, unbound electron and the impact parameter. A more accurate formula, attributed to Bethe and Bloch (Bethe, 1930; Bloch, 1933), takes into account quantum mechanical effects and is given by

$$\frac{S}{\rho} = -\frac{\mathrm{d}E}{\rho \mathrm{d}x} = 4\pi N_A r_e^2 m_e c^2 \frac{Z}{A}\frac{z^2}{\beta^2}\left[ln\frac{2m_e c^2 \gamma^2 \beta^2}{I} - \beta^2 - \frac{\delta}{2} - \frac{C}{Z}\right], \quad (3)$$

where N_A is Avogadro's number, r_e is the classical electron radius, m_e is the mass of an electron, z is the charge of the projectile, Z is the atomic number of the absorbing material, A is the atomic weight of the absorbing material, c is speed of light, $\beta = v/c$ where v is the velocity of the projectile, $\gamma = (1-\beta^2)^{-1/2}$, I is the mean excitation energy of the absorbing material, δ is the density correction item arising from the shielding of remote electrons by close electrons and will result in a reduction of energy loss for higher energies, and C is the shell correction item, which is important only for low energies where the particle velocity is near the velocity of the atomic electrons. The two correction items in the Bethe-Bloch equation involve relativistic theory and quantum mechanics and need to be considered when very high or very low proton energies are used in calculations. Figure 2 plots proton stopping power as a function of proton energy in water calculated by using Equation (3).

It is instructive to observe in Equation (3) how the projectile's characteristics govern its energy loss rate: energy loss is proportional to the inverse square of its velocity ($1/v^2$ classically and $1/\beta^2$ relativistically) and the square of the ion charge ($z = 1$ for protons), and there is no dependence on projectile mass. Similarly, Equation (3) reveals that the absorber material can also strongly influence the energy loss rate. Specifically, the linear stopping power is directly proportional to the mass density. It is equivalent, but perhaps more physically meaningful, to state that the linear stopping power is proportional to the density of electrons in the absorber ($N_A \rho Z/A$), because the energy loss occurs by Coulombic interactions between the proton and atomic electrons. Z/A varies by only about 16%, from 0.5 for biologic elements such as carbon and oxygen to 0.42 for high-Z beamline components, such as lead. Hydrogen is an obvious exception to this; fortuitously, the concentration of hydrogen in the human body is low (only about 10%) and nearly uniform throughout the body. The stopping power also depends on a material's I value, and the I value depends in a monotonic way on the Z of the absorber, varying from about 19 eV for

hydrogen to about 820 eV for lead. However, the stopping power goes with the logarithm of I^{-1} value, so the dependence is diminished. Hence, putting these various dependencies in perspective, it is clear that the proton energy loss rate in the human body depends most strongly on the material density, which can vary by about three orders of magnitude, from air in the lung to cortical bone, and the ion velocity, which can cause the linear stopping power in water to vary by about a factor of 60 for proton energies between 1 MeV and 250 MeV.

The stopping power theory for protons and heavier ions was reviewed by Ziegler *et al.* (Ziegler *et al*, 1985; Ziegler, 1999; Ziegler *et al*, 2008) and in Report 49 of the International Commission on Radiation Units and Measurement (1993). Evaluated stopping power and range tables may be conveniently calculated with the SRIM code ("Stopping and Ranges of Ions in Matter," computer program, http://www.srim.org/.).

Thus far, we have described proton energy loss in an approximate way on the assumptions that a proton loses energy along a 2-dimensional line trajectory and that energy loss is continuous. Absorption of this same energy, however, occurs in a 3-dimensional volume. Furthermore, the ionization track of a proton has an irregular 3-dimensional structure caused by random fluctuations in the location and size of primary ionization events. This is caused mainly by proton-produced recoil electrons, some of which are sufficiently energetic to create small spur tracks of ionization emanating from the main track. Because the electrons are very much lighter than the protons, each interaction can reduce the proton energy only a little. The maximum possible energy transfer in a collision of an ion of mass *m* with an unbound stationary electron is

$$\Delta_1^{max} = \frac{2m_e c^2 \beta^2}{1-\beta^2}\left[1 + 2\frac{m_e}{M}\frac{1}{\sqrt{1-\beta^2}} + \left(\frac{m_e}{M}\right)^2\right], \quad (4)$$

where m_e is the mass of an electron, *M* is the mass of the target material, *c* is the speed of light, and $\beta = v/c$ where *v* is the velocity of the projectile.

Even for very energetic protons, the secondary electrons do not acquire enough energy to travel more than a few millimeters from the proton track. For example, at 200 MeV proton energy, the maximum secondary electron energy is around 500 keV, which corresponds to an electron range of approximately 2 mm in water. The probability of producing secondary electrons may be calculated with various total or differential cross-sections; these were reviewed in ICRU Report 55 (1995). Track structure models may be used to estimate the radial properties of ions (Kraft *et al*, 1999), although this has not found common application in clinical proton therapy. Regardless of the calculation method used, the spatial characteristics of secondary charged particles should, in principle, be taken into account near material interfaces (*e.g.*, buildup effects in transmission beam monitoring instruments, skin, air-tumor interfaces in the lung) and in cases where the radiation quality is of interest (*e.g.*, microdosimetric and nanodosimetric characterization of individual dose deposition events).

Finally, we note that in proton therapy water is considered an excellent tissue substitute because of its similar density, effective *Z*/*A*, and other properties. Furthermore, proton

energy loss and residual range in various materials are often expressed in terms of their water-equivalent values. We discuss this in detail in section 3.1, but until then, for simplicity, we consider water as being perfectly equivalent to tissue.

2.2 Range

Range is defined as the depth at which half of protons in the medium have come to rest, as shown in the range-number curve plotted in Figure 3. There are small variations in the energy loss of individual protons (an effect called range straggling, which is discussed in the following section). Consequently, the range is inherently an average quantity, defined for a beam and not for individual particles. By convention, this means half of the protons incident on the absorber are stopped, although in some cases this is taken instead to mean that half the protons survive to near the end of range (*i.e.*, neglecting protons removed by nuclear reactions).

The path of most protons in matter is a nearly straight line. On average, the proton's pathlength is very nearly equal to its projected pathlength and range. This simple but important fact renders many proton range calculations tractable with relatively simple numerical or analytical approaches.

Let us first consider a simple numerical calculation of proton beam range. We use proton stopping power data and perform a one-dimensional proton pathlength transport calculation on the assumptions that the ions travel only straight ahead (negligible lateral scattering) and that the protons lose energy in a continuous matter. (These assumptions are reasonable for many clinical calculations, but we examine then relax these assumptions in a later section.) In this case, the range (R) may be calculated as

$$R(E) = \int_0^E \left(\frac{\mathrm{d}E'}{\mathrm{d}x}\right)^{-1} \mathrm{d}E' \approx \sum_0^E \left(\frac{\mathrm{d}E'}{\mathrm{d}x}\right)^{-1} \mathrm{d}E', \quad (5)$$

where E is the ion's initial kinetic energy. The summation denotes that the continuous transport is approximated by calculations of discrete steps. In fact, as discussed above, this equation actually gives the pathlength, which is an excellent approximation of range in most clinical situations. Figure 2 plots proton range in water calculated by using Equation (5).

Next, we calculate the proton range using an analytical approach, which may be faster and more practical than the numerical approach for many clinical calculations. We begin by noting that the interval of proton range of interest typically extends from 1 mm (about the size of a voxel in an anatomic image of patient anatomy) to about 30 cm (about the midline of a large adult male's pelvis, the deepest site in the human body). These ranges correspond to 11 MeV and 220 MeV, respectively, as seen in Figure 2. More importantly, Figure 2 reveals that the relationship between the logarithm of range and logarithm of energy is almost linear. This is fortuitous because this means that the range follows a very simple power law, as realized by Bragg and Kleeman (1905) and others early in the last century. Thus, the range of a proton may be calculated using BK Rule, or

$$R(E) = \alpha E^p, \quad (6)$$

where, as before, α is a material-dependent constant, E is the initial energy of the proton beam, and the exponent p takes into account the dependence of the proton's energy or velocity.

The uncertainty in proton range depends on many factors. For example, the uncertainty in a range measurement depends on the precision and accuracy of the measurement apparatus and, in some cases, on the experimenter's skill. A common concern in clinical proton therapy is the uncertainty in calculated range, e.g., in calculating the settings of the treatment machine for a patient's treatment. The uncertainty in range may depend on the knowledge of proton beam energy distribution and on properties of all range absorbing materials in the beam's path. These include elemental composition, mass density, and linear stopping power. The linear stopping powers deduced from computed tomography scans have many additional sources of uncertainty, including imperfections in the calibration of CT scanners (i.e., the method used to convert image data from Hounsfield Units to linear stopping power), partial volume effects, motion artifacts, and streaks artifacts.

2.3 Energy and range straggling

In the preceding sections, we approximated the energy loss rate by assuming that the slowing of ions occurs in a smooth and continuous manner. In fact, we considered the mean energy loss rate and neglected variations in the energy loss rates of individual protons. For many clinical calculations, these assumptions are valid and lead to a reasonably good first-order approximation. However, the accumulation of many small variations in energy loss, termed energy straggling or range straggling, is one of the physical processes that strongly governs the shape of a proton Bragg curve, a subject that is covered in section 3.2. Thus, an understanding of range straggling is key to understanding the characteristics of proton dose distributions.

Figure 4 plots the relative energy loss probability density functions (PDF) for protons transmitted through water absorbers of various thickness. The curves have been normalized to enhance visual clarity. Apparently, thick absorbers result in a symmetric distribution of energy losses, whereas thin absorbers yield curves that are asymmetric with modes less than the mean and long tails of large energy losses. In principle, straggling PDFs may be calculated numerically from first principles, but usually theoretical approaches are used. Later in the section, three of the most commonly used straggling theories are described.

Having examined the mean energy loss rate in modest detail (section 2.1), and having conceptually introduced energy straggling, it is instructive to understand how these effects are related mathematically before delving into straggling theory. To understand these relationships, let us consider the moments of the ion energy PDF, or

$$M_n = \int_0^{\Delta_1^{max}} \Delta^n f(\Delta)\, \mathrm{d}\Delta, \quad (7)$$

where Δ is the energy loss of an ion in traversing an absorber, *f*(Δ)dΔ is the probability of energy loss occurring in the interval from Δ to Δ + dΔ, and *n* is the order of the moment. The zeroth moment is the total collision cross section, the first moment is the (mean) electronic stopping power, the second moment corresponds to the width (variance) of the energy straggling distribution, the third moment to its asymmetry (skewness), and the fourth to its kurtosis. The variance, sometimes denoted by σ_Δ^2, or second moment of the straggling distribution *f*(Δ), is

$$M_2(\Delta) = \sigma_\Delta^2 = \bar{v} \int_0^{\Delta_1^{max}} \Delta^n f_1(\Delta)\, \mathrm{d}\Delta. \quad (8)$$

A more detailed discussion of the straggling moments was given by Rossi and Zaider (1996).

Next we examine theories for calculating energy straggling proposed by Bohr (1915), Landau (1944), and Vavilov (1957). These theories are valid for thick, intermediate, and thin absorbers, respectively. The criterion for selecting a valid theory for a given absorber thickness is based on a reduced energy parameter,

$$k = \frac{\xi}{\Delta_1^{max}}, \quad (9)$$

where ξ is the approximate mean energy loss and Δ_1^{max} is the maximum energy loss possible in a single event.

According to Bohr's theory, the energy straggling distribution behaves according to a Gaussian PDF, or

$$f(\Delta)\, \mathrm{d}\Delta = \frac{1}{\sigma_\Delta \sqrt{2\pi}} exp \frac{-\left(\Delta - \bar{\Delta}\right)^2}{2\sigma_\Delta^2}, \quad (10)$$

where for non-relativistic ions the variance is given by

$$\sigma_\Delta^2 = 2\pi r_e^2 m_e c^2 z^2 \frac{NZ}{\beta^2} \Delta_1^{max} \rho x. \quad (11)$$

Bohr's theory assumes that the absorber is thick enough that there are many individual collisions (*i.e.*, the central limit theorem holds), that the ion velocity does not decrease much in crossing the absorber, and that the absorber is made of unbound electrons. For most applications in proton therapy, Bohr's theory provides adequate accuracy. Several authors have reported convenient power law approximations to estimate sigma as a function of the proton beam range (Chu *et al*, 1993), or

$$\sigma_\Delta \approx k R_0^m, \quad (12)$$

where R_0 is the range in water in centimeters for a mono-energetic proton beam, *k* is a material-independent constant of proportionality, and the exponent is empirically determined. For protons in water, *k* = 0.012 and *m* =0.935 (Bortfeld, 1997).

Landau's theory relaxed the assumption that the central limit holds, *i.e.*, there are relatively fewer individual collisions in an intermediate thickness absorber, and used an approximate expression for Δ_1.

In this case, we have

$$f(\Delta, \rho x)\,\mathrm{d}\Delta = \frac{1}{\xi}\phi_L(\lambda_L), \quad (13)$$

where the parameter $\phi_L(\lambda_L)$ roughly corresponds to the deviation from the mean energy loss and was defined by Landau as

$$\phi_L(\lambda_L) = \frac{1}{\pi}\int_0^\infty e^{-y\left(ln\, y - \lambda_L\right)} sin(\pi y)\,\mathrm{d}y. \quad (14)$$

Evaluation of the integral in Equation (14) is straightforward and the reader is referred to the literature for details (Seltzer and Berger, 1964).

Vavilov's theory is in essence a generalization of Landau's theory that utilizes the correct expression for Δ_1 and is given by

$$f(\Delta, \rho x)\,d\Delta = \frac{1}{\xi}\phi_V\left(\lambda_V, k, \beta^2\right)\mathrm{d}\lambda_V, \quad (15)$$

where

$$\phi_V\left(\lambda_V, k, \beta^2\right) = \frac{1}{\pi}e^{k\left(1+\beta^2\gamma\right)}\int_0^\infty e^{kf_1}\, cos\left(\lambda_V y + k f_2\right)\mathrm{d}y, \quad (16)$$

and

$$\lambda_V = \frac{\Delta - \bar{\Delta}}{\Delta_1^{max}} - k\left(1+\beta^2-\gamma\right), \quad (17)$$

where γ is Euler's constant. The evaluation of Vavilov's theory is computationally more expensive than that of Bohr's or Landau's. For additional details, the reader is referred to Vavilov's original work (Vavilov, 1957).

2.4 Multiple Coulomb scattering

As illustrated in Figure 5, a proton passing close to the nucleus will be elastically scattered or deflected by the repulsive force from the positive charge of the nucleus. While the proton loses a negligible amount of energy in this type of scattering, even a small change in its trajectory can be of paramount importance. In fact, it is necessary to take into account Coulomb scattering when designing beamlines and treatment heads (Gottschalk, 2010b) and in calculations of dose distributions in phantoms or patients, *e.g.*, with treatment planning systems (Hong *et al*, 1996; Pedroni *et al*, 2005; Schaffner, 2008; Koch and Newhauser, 2010).

To characterize the amount that a beam is deflected by scattering, we use the quantity of scattering power, which is defined as

$$T = \mathrm{d}\left\langle \theta^2 \right\rangle / \mathrm{d}x, \quad (18)$$

where $<\theta^2>$ is the mean squared scattering angle and x is the thickness of absorber through which the proton has traveled. Similarly, the mass scattering power is simply T/ρ, where ρ is the mass density of the absorber material. Notice that the definition of scattering power utilizes the mean square of the scattering angle; scattering is symmetric about the central axis, and therefore the mean scattering angle is zero and contains no useful information. Also, note that the value of the scattering power depends on the material thickness (*i.e.*, it depends on the material properties and dimensions of the absorber being considered).

Predictions of elastic Coulomb scattering are commonly classified according to the number of individual scattering events (N_s) that occur in a given absorber. For single scattering (N_s=1), Rutherford scattering theory applies. Plural scattering ($1 < N_s < 20$) is difficult to model theoretically and is not discussed further here. Multiple Coulomb scattering (MCS; $N_s \geq 20$), the combined effect of all N_s scattering events, may be modeled by using a statistical approach to predict the probability for a proton to scatter by a net angle of deflection, commonly denoted by θ (Figure 5).

It is instructive to briefly examine Rutherford's theory of single scattering (Rutherford, 1911). The differential cross section $\mathrm{d}\sigma$ for scattering into the solid angle $\mathrm{d}\Omega$ is given by

$$\frac{\mathrm{d}\Omega}{\mathrm{d}\Omega} = z_1^2 z_2^2 r_e^2 \frac{(m_e c/\beta p)^2}{4\, sin^4\,(\theta/2)}, \quad (19)$$

where z_1 is the charge of the projectile, z_2 is the atomic number of the absorber material, r_e is the classical electron radius, m_e is the mass of the electron, c is the speed of light, $\beta = v/c$, p is the ion momentum, and θ is the scattering angle of the proton. The angular dependence is governed by the term $1/\sin^4(\theta/2)$, *i.e.*, in individual scattering events, the proton is preferentially scattered in the forward direction, at very small angles.

In clinical proton therapy, most objects of interest are thick enough to produce a great many scattering events. Thus, for clinical proton therapy, we are usually more interested in the net effect that many small-angle scattering events have on many protons, *e.g.*, how beamline scattering in the treatment head influences the spatial distribution of dose in a patient.

Rigorous theoretical calculations of MCS are quite complex. The most complete theory was proposed by Molière (1948). Assuming that scattered particles are emitted at small deflection angles (*i.e.*, the small-angle approximation in which $\sin(\theta) \approx \theta$),

$$P\,(\theta) = \eta d\eta \left(2\, exp\left(-\eta^2\right) + \frac{F_1\,(\eta)}{B} + \frac{F_2\,(\eta)}{B^2} \cdots \right), \quad (20)$$

where $\eta = \theta / (\theta_1 B^{1/2})$, and $\theta_1 = 0.3965 (zZ/p\beta) \sqrt{\rho \delta x / A}$. The functions $F_k(\eta)$ are defined as

$$F_k(\eta) = \frac{1}{k!} \int J_0(\eta y) \; exp\left(\frac{-y^2}{4}\right) \left[\frac{y^2}{4} ln\left(\frac{y^2}{4}\right)\right]^k y \mathrm{d}y, \quad (21)$$

where $J_o(\eta\gamma)$ is a Bessel function. Values of F_i have been tabulated in the literature by several authors. Parameter B in Equation (20) may be found by numerical methods, by solving

$$g(B) = ln \quad B - B + ln \quad \gamma - 0.154 = 0, \quad (22)$$

where $\gamma = 8831 \; q \; z^2 \; \rho \delta x / (\beta^2 A \Delta)$ and $\Delta = 1.13 + 3.76 \; (Zz/137\beta)^2$. The following are symbols representing properties of the absorber: Z is the atomic number, A is the atomic mass, δx is the thickness, and ρ is the mass density. The proton momentum is denoted by p, $\beta = v/c$, and $z = 1$ is the proton charge. Even though we have not presented all of the details, clearly the evaluation of Molière's theory is indeed complex. Consequently, considerable attention has been paid in the literature to developing simpler formulae; the simplicity usually comes at the cost of reduced accuracy in modeling scattering at large angles. Gottschalk (1993) discussed several of these methods in detail. One approximation method takes the form of a Gaussian distribution,

$$P(\theta) \approx \frac{2\theta}{\langle \theta^2 \rangle} exp\left(\frac{-\theta \zeta^2}{\langle \theta^2 \rangle}\right) \mathrm{d}\theta, \quad (23)$$

where $(<\theta^2>)^{1/2}$ is the root mean square (*rms*) scattering angle or the width parameter of the Gaussian distribution.

Gottschalk (2010b) proposed a differential approximation to Molière's theory to predict the scattering power according to

$$T_{dM} = f_{dM}(pv, p_1 v_1) \times \left(\frac{E_S}{pv}\right)^2 \frac{1}{X_S}, \quad (24)$$

where $E_S = 15$ MeV, p is the momentum and v is the velocity of the proton, p_1 and v_1 are the initial momentum and velocity, X_S is scattering length of the material, and f_{dM} is a material-independent nonlocal correction factor given by

$$f_{dM} = 0.5244 + 0.1975 \; lg\left(1 - (pv/p_1 v_1)^2\right) + 0.2320 \; lg(pv) - 0.0098 \; lg(pv) \; lg\left(1 - (pv/p_1 v_1)^2\right) \quad (25)$$

The factor f_{dM} takes into account the accumulation of scattering that occurs as the proton slows from v_1 to v and is material independent. The scatter length is given by

$$\frac{1}{\rho X_S} = \alpha N r_e^2 \frac{Z^2}{A} \left(2 \; log(33219 \; (AZ)^{-1/3} - 1\right), \quad (26)$$

where α is the fine structure constant, N is Avogadro's number, r_e is electron radius, and Z, A, and ρ are the atomic number, atomic weight, and density of the target material.

It is sometimes convenient to project the expected scattering angle $<\theta>$ in three-dimensional space to the corresponding value in a plane, denoted $<\theta_x>$, according to

$$\langle\theta_x\rangle^2=\langle\theta\rangle^2/2, \quad (27)$$

Also, in proton therapy the lateral displacement (r) of a proton beam is typically calculated from the scattering angle. Under the Gaussian approximation, we have

$$P(r)\,\mathrm{d}r=6r\left(\left\langle\theta^2\right\rangle t^2\right)^{-1} exp\left(-3r^2/\left(\left\langle\theta^2\right\rangle t^2\right)\right)\mathrm{d}r, \quad (28)$$

where $t = x/L_{rad}$, and L_{rad} is the radiation length of the material, which can be calculated easily or looked up in tables. The mean square lateral displacement is given by

$$\left\langle r^2\right\rangle=\left\langle\theta^2\right\rangle t^2/3, \quad (29)$$

A power law approximation for rms of protons is

$$r_{rms}=a \quad R^b, \quad (30)$$

where a is a unitless material constant, R is the proton beam range (in the same units as r_{rms}), and the exponent b governs the range dependence. For protons in water, a = 0.0294 and b = 0.896 (Chu *et al*, 1993). Koehler and Preston derived a convenient expression to calculate r_{rms} as a function of depth in an absorber and knowledge of its maximum values, r_{max}, at the end of range (from an unpublished manuscript; some portions of their work were reported by Gottschalk (2010b)).

In proton therapy, MCS in the treatment head (*i.e.*, in the scattering foils) is helpful because it allows the beam to be spread laterally to useful dimensions, *e.g.*, to make a beam laterally large and flat so that a tumor may be completely covered with a uniform dose. Scattering foils in the nozzle are carefully designed to utilize MCS and energy loss to produce clinically useful beams (Koehler *et al*, 1977; Gottschalk, 2004) However, MCS in the treatment head and in the patient blurs lateral penumbral sharpness. This is manifested as penumbral growth at the edge of collimated beams and/or the growth of the lateral spot size of a scanned beam (Figure 6). Understanding and preserving penumbral sharpness is the key to realizing the full benefit of proton therapy for sparing healthy tissue.

Recent studies have revealed that MCS plays an important role in proton dose distribution around small implanted metal objects. Specifically, implanted fiducial markers for image-guided patient alignment have been used in proton therapy for many years (Gall *et al*, 1993; Welsh *et al*, 2004; Newhauser *et al*, 2007a; Newhauser *et al*, 2007c; Ptaszkiewicz *et al*, 2010; Matsuura *et al*, 2012). Substantial recent improvements in on-board imaging systems, patient positioning, and patient immobilization have led to increased use of radiopaque implanted fiducial markers in proton therapy to many disease sites, with the goal of

improving target coverage and/or normal tissue sparing. However, recent studies revealed that some commonly used markers, even those less than 1 mm in size, can cause severe cold spots (Figure 7), compromising target coverage (Newhauser *et al*, 2007a; Newhauser *et al*, 2007c; Carnicer *et al*, 2013). The severity of the cold spots varies with fiducial size, material composition, and mass density. These parameters, in turn, determine the amount of MCS and energy loss in the fiducial and, hence, perturbations to the dose distribution in surrounding tissue. In essence, MCS in the fiducial causes a downstream dose shadow that may be partially or fully filled in by MCS in the surrounding tissue. While MCS is important, energy loss in the fiducial (or its water-equivalent thickness), the proximity of the fiducial to the end of the proton beam range, and of course its size and orientation with respect to the beam also should be considered. The physics of dose perturbations is explained in detail elsewhere (Newhauser *et al.*, (2007a), and several subsequent studies (Giebeler *et al*, 2009; Lim *et al*, 2009; Cheung *et al*, 2010; Huang *et al*, 2011) have shown that it is possible to achieve good radiographic visibility using novel markers that do not significantly perturb the therapeutic dose distribution in tissue.

Others have examined the effects of MCS in larger metal objects on clinical proton beams and characterized the suitability of approximate methods to predict MCS in practical clinical applications (Herault *et al*, 2005; Stankovskiy *et al*, 2009; Newhauser *et al*, 2013).

2.5 Nuclear interactions

In addition to the mechanisms already described, protons may interact with the atomic nucleus via non-elastic nuclear reactions in which the nucleus is irreversibly transformed, *e.g.*, a reaction in which a proton is absorbed by the nucleus and a neutron is ejected, denoted by (p,n). The main effect of nuclear reactions within a therapeutic region of a proton field is a small decrease in absorbed dose due to the removal of primary protons, which is compensated to a large extent by the liberation of secondary protons and other ions. In this section, we discuss this and several other important aspects of nuclear reactions.

Before discussing reaction mechanisms, it is instructive to examine a range-number curve (Figure 3), which plots the remaining number of protons versus depth in an absorber as a beam comes to rest. The gradual depletion of protons from entrance to near the end of range is caused by removal of protons from nuclear reactions. The rapid falloff in the number of protons near the end of range is caused by ions running out of energy and being absorbed by the medium. The sigmoid shape of the distal falloff is caused by range straggling or by stochastic fluctuations in the energy loss of individual protons.

To enter the nucleus, protons need to have sufficient energy to overcome the Coulomb barrier of the nucleus, which depends on its atomic number. The total non-elastic cross-section for proton-induced nuclear reactions has a threshold, on the order of 8 MeV in the atomic nuclei of biologically relevant elements, which rises rapidly to a maximum at around 20 MeV, then asymptotically declines to about half the maximum value by about 100 MeV (Figure 8). Tabulated and graphical nuclear data may be obtained conveniently online from the Evaluated Nuclear Data File (ENDF) (http://wwwnds.iaea.org/exfor/endf.htm). ICRU Report 63 also provides extensive nuclear data for hadron therapy and radiation protection (ICRU, 2000).

Several nuclear reactions are particularly important to clinical proton therapy and proton therapy research. In a proton therapy beam, proton-induced reactions can produce energetic protons, deuterons, tritons, ^{3}He, ^{4}He, and other ions. Secondary protons comprise as much as about 10% of the absorbed dose in a high-energy proton treatment beam; they have a small but non-negligible impact on the spatial dose distribution in a patient (Medin and Andreo, 1997; Boon, 1998; ICRU, 1998; Paganetti, 2002; Wroe *et al*, 2005) Deuterons and heavier ions are present in much smaller proportions; collectively they comprise about 1% or less of the therapeutic absorbed dose (ICRU, 1998). Their energy and range are very small and they deposit their kinetic energy locally, *i.e.*, very near their point of creation.

Relatively high-current protons beams are incident on certain beam production and delivery equipment and on some patients. These proton beams produce neutrons that create significant potential safety hazards. Great care must be taken to limit exposures of personnel to neutrons (NCRP, 1971, 1990, 1993, 2005; Newhauser and Durante, 2011). Some electronic systems must also be hardened, shielded, or located so that neutron radiation does not cause soft upsets or permanent damage to semiconductor components. Attention must also be paid to neutron activation of beamline components, air, groundwater, and other materials (IAEA, 1988).

Neutrons are produced in copious quantities: they span 10 orders of magnitude in neutron energy, their energy distributions depend strongly on the proton beam energy and direction, they are extremely penetrating, and their relative biologic effectiveness is as much as about 20 times higher than that of proton radiation (ICRP, 2007). Thus they potentially increase the risk of radiogenic late effects (Hall, 2006; Brenner and Hall, 2008; Newhauser and Durante, 2011). Great care must be taken to ensure that patients and staff are adequately protected from neutron exposures. Several specific aspects of neutron exposures are considered in a later section of this paper.

Nuclear reactions inside the patient may provide a non-invasive approach to measure a variety of beam and patient properties, such as proton beam range, elemental composition of tissues, and even intra- or inter-fraction physiology. The basic approach is to detect gamma rays from proton-induced nuclear reactions, such as neutron capture reactions, denoted by (n,γ). Approaches are under development that detect photons from positron annihilation, prompt gammas, and delayed gammas. Gamma ray detection approaches have included positron emission tomography camera (Parodi *et al*, 2007; Moteabbed *et al*, 2011; Cho *et al*, 2013; Min *et al*, 2013), Compton camera (Peterson *et al*, 2010; Smeets *et al*, 2012), one-dimensional detector arrays (Min *et al*, 2012), and photon counting systems (Kim *et al*, 2012). These techniques are in various stages of research and development; none is routinely used in clinical practice. There remain many challenges to overcome, including instrument sensitivity and calibration; interpretation of measurements, including an understanding of managing measurement artifacts; and competition from alternative methods, *e.g.*, magnetic resonance imaging techniques (Krejcarek *et al*, 2007; Raaymakers *et al*, 2008; Gensheimer *et al*, 2010).

3. Proton transport calculations

In this section, we review several aspects of proton transport physics that are encountered frequently in clinical and research situations. We describe the one-dimensional water-equivalent thickness of an arbitrary material, the shapes of a pristine Bragg curve and a spread out Bragg peak (SOBP) curve, and stray radiation exposures.

3.1 Water-equivalent thickness

As we mentioned previously, in proton therapy water closely mimics the properties of human tissues in terms of energy loss, MCS, and nuclear interactions. As such, water is a recommended phantom material for dose and range measurements and reference material for reporting corresponding calculated quantities (ICRU, 1998; IAEA, 2000). For example, it is a common and convenient clinical practice to specify the penetrating power of a proton beam by its range in water (ICRU, 1998, 2007). In this way, range losses in various beamline objects and the patient may be easily added or subtracted from one another in a physically consistent way. Viewed another way, it is also convenient to specify the range-absorbing power of various objects in the beam path, *e.g.*, beam transmission monitors and immobilization devices, by their equivalent thickness if they were made of water.

Water-equivalent thickness (WET) is often used to characterize the beam penetration range; Figure 9 schematically illustrates the concept of WET and how it can be calculated or measured. For treatment sites with nearby critical structures, *e.g.*, an optic nerve, the range of the planned and delivered beams must agree within a few millimeters. To accomplish this, treatment planning systems are commonly configured with the WET values of all items not included in the planning CT images, such as components in the treatment head, immobilization devices not present during the CT scan, or a treatment couch (Newhauser *et al*, 2007b). Similarly, to determine the measurement geometry for patient-specific clinical quality assurance measurements, the WET of measurement instruments and possibly other devices must be determined (Newhauser, 2001b, a). Thus, it is important to have methods to calculate and measure WET. In this section, we emphasize recently developed calculation methods that are convenient and suitable for clinical calculations, using the energy loss theories presented in section 2. Our discussion of WET measurement methods is very brief, mainly because they are relatively simple and obvious. In practice, however, WET measurements remain very important (Andreo, 2009; Gottschalk, 2010a; Newhauser and Zhang, 2010; Zhang *et al*, 2010b; Besemer *et al*, 2013).

The IAEA (2000) proposed that WET can be approximated by

$$t_w = t_m \frac{\rho_m}{\rho_w} c_m, \quad (31)$$

where the depth scaling factor, c_m, can be calculated, to a good approximation, as the ratio of the continuous slowing down approximation (CSDA) range (in g cm^{-2}) in water to that in the target:

$$c_m = \frac{\rho_w R_w}{\rho_m R_m}. \quad (32)$$

Because the ranges in Equation (32) correspond to complete loss of ion energy, this approach is strictly valid only for stopping-length targets. An exact equation for WET that is applicable to thin targets was reported by Zhang and Newhauser (2009):

$$t_w = t_m \frac{\rho_m \overline{S_m}}{\rho_w \overline{S_w}}, \quad (33)$$

where ρ_w and ρ_m are the mass densities of water and material, respectively, and $\bar{S}_m$ and $\bar{S}_w$ are the mean proton mass stopping power values for the material and water, respectively, defined by

$$\bar{S} = \frac{\int_E S \mathrm{d}E}{\int_E \mathrm{d}E}. \quad (34)$$

For thin targets, where the proton loses a negligible fraction of its energy in the absorber material, we have

$$t_w \approx t_m (\rho_m / \rho_w)(S_m / S_w) = t_m \frac{\alpha_w p_w}{\alpha_m p_m} E^{p_w - p_m}, \quad (35)$$

where the reader will recognize α and p from the discussion of the BK Rule (see section 2.1). Values of α and p for commonly encountered materials in proton therapy are provided in Table 2. Zhang and Newhauser (2009) also reported a slightly more complex analytical formula to calculate WET for targets of arbitrary thickness.

As can be seen in the curves of the water-equivalent ratio (WER = t_w/t_m) plotted in Figure 10, taking into account the target thickness in calculating WER is most important for absorbers that are thick and made of high Z materials, *e.g.*, lead scattering foils, and for protons that are of comparatively low energy when impinging on the target. For low-Z materials, such as tissue and plastic, WER depends only very weakly on the target thickness and initial proton beam energy, and the approximate (thin and stopping length) analytical methods provide sufficient accuracy for most clinical applications.

3.2 Features of pristine and spread-out Bragg curves

The spatial dose distribution from clinical proton therapy beams is quite similar to those from photon and electron beams. The lateral profiles are generally quite flat in the central high-dose region, then fall off rapidly in the penumbral regions, where the penumbra width increases with depth in the patient. On the other hand, the central-axis depth-dose curve from protons is somewhat similar to that from electrons, but with a sharper distal falloff. Figures 11 and 12 compare the central-axis depth-dose curves from several radiation therapy beams, revealing the main dosimetric properties that are clinically advantageous in many cases, namely, relatively low entrance dose, large and uniform dose to cover the tumor, and

rapid falloff of dose near the end of range to spare normal tissues. These properties, together with a uniform lateral dose profile and a sharp lateral penumbral width, allow proton beams to treat a wide variety to tumor sizes and locations while providing superior sparing of normal tissues in many cases.

Having casually inspected the shape of proton depth-dose curves, we next examine their structure in greater detail, pointing out nomenclature and the physical processes that govern the shape of various regions. Figure 13 shows a pristine proton peak along with labels identifying several regions. In order of increasing depth, these are the regions of electronic buildup, protonic buildup, sub-peak, peak, and distal falloff (same as for peak). The figure also shows several characteristic depths (*e.g.*, the depth z_{BP} at which the Bragg peak occurs) and various characteristic lengths (*e.g.*, the 80%-to-20% distal-falloff length $l_{80\text{-}20}$ and the proximal-80%-to-distal-80% pristine-peak width).

The anatomic definitions of an SOBP are, in many ways, similar to those of a pristine Bragg curve, as seen in Figure 14. However, there are several unique difficulties in characterizing SOBPs because of their sometimes unusual shape. For example, SOBPs with two or more discrete pristine Bragg curves may have multiple dose maxima in the modulated-peak region (*e.g.*, the ripple shown in Figure 15). Because of such problems we introduce a few additional quantities that are defined only for SOBPs. To a large extent, however, we have defined quantities and terminology that are common to both modulated and pristine Bragg curves.

We have not yet mentioned how MSC affects the shape of the depth-dose curves. In fact, near the central region of a laterally “large” beam, or more correctly well inside the periphery of a large beam, there is an equilibrium in which lateral scattering away from the central axis is exactly compensated by scattering towards it. This effect is described in Figure 16, which is adapted from Koehler and Preston (Koehler and Preston, 1972). As the field size shrinks to the dimension of the rms lateral displacement due to MCS, lateral equilibrium is lost and MCS progressively depletes the proton fluence and dose along the central axis. Small proton beams have been investigated in several studies, including those by Takada (Takada, 1996), Moyers *et al*. (1999), Vatnitsky *et al.* (1999b), Bednarz *et al.* (2010), and Gottschalk (1999), as well as others, especially in the context of scanned beams and pencil beam dose algorithms.

Here, we use a Cartesian coordinate system with the *z* axis parallel to and centered about the proton beam central axis. The *x* and *y* axis are mutually orthogonal and perpendicular to the *z* axis. The coordinate system origin is located at the front face of the absorber, *e.g.*, the extended medium in which we consider the absorbed dose distribution.

Pristine Bragg curve—A depth-dose distribution in an absorber irradiated with a monoenergetic or nearly-monoenergetic proton beam. In other words, no device or technique has been intentionally deployed for modulating the proton fluence or spectral fluence.

Spread-out Bragg curve—A depth-dose distribution in an absorber irradiated with a beam that has been intentionally modified to increase the axial dimension of the peak region. This is accomplished by modulating the range and the fluence of the beam. Clinical systems accomplish this by combining multiple quasi-monoenergetic beams or with a continuously modulated beam.

Electronic buildup region—A small region near the surface of the absorber where the proton beam is incident. As discussed in section 2.1, high-energy proton beams liberate delta rays with sufficient kinetic energy to travel several millimeters in tissue. Under some circumstances, this region exhibits an increase of dose with increasing depth, asymptotically approaching absorbed dose in the sub-peak region within the depth corresponding to the range of the most penetrating recoil electron. In some cases, electronic buildup is not observed. There are several possible reasons for this: the presence of some material just upstream of the surface (*e.g.*, an immobilization device or a range compensator) may provide partial or full electronic charged particle equilibrium in the absorber, it may occur in combination with protonic buildup, it may be masked by changes in the proton energy loss rate near the end of range, or the wall of a cavity dosimeter may be sufficiently thick to present electronic equilibrium to the dosimeter's sensitive volume.

Protonic buildup region—A region near the surface of the absorber where the absorbed dose increases with depth because of the buildup of secondary protons that are attributable to proton-induced non-elastic nuclear interactions (*e.g.*, ^{16}O(p,xp) reactions). As with electronic buildup, the protonic buildup may not be observed in some cases, particularly at low incident proton beam energies.

Sub-peak region—The region extending from the surface of the absorber to the depth just proximal of the peak. The physical processes involved here are, in decreasing order of importance, the stopping power's dependence on the inverse-square of the proton velocity, the removal of some protons by nuclear reactions, the liberation of secondary particles from nuclear reactions, and for very small fields, the accumulation of lateral deflections from MCS leading to lateral protonic disequilibrium and reduction of the proton fluence on the central axis. The distal extent of the sub-peak region can be calculated from $z_m - 2\sigma$, where z_m is the depth at the pristine Bragg peak and σ is the width of the peak. The width parameter σ can be estimated from the incident proton beam spectral fluence and the range straggling accumulated in the absorber, as discussed in section 2.3.

Pristine Bragg peak—The pristine Bragg peak is simply the maximum (or mode) dose near the end of range, and is located at z_{BP}, which is defined next. The physical processes governing the location and/or height of the peak are mainly the proton stopping power and energy straggling, nuclear reactions to a much lesser extent and, for very small fields, MCS..

Pristine Bragg peak depth—The depth near the end of range of the primary protons at which the protons produce the maximum dose rate, denoted by z_{BP}. Although small proton beams are not yet widely used, it is helpful to define the location of z_{BP} in a way that is compatible with large and small beams. Figure 16 shows that the maximum dose for beams

of diameter larger than 6 mm is clearly single valued and located near the end of range. For smaller beams, however, the dose at the peak near the end of range may be less than the dose in the proximal regions, creating multiple maxima to choose from. Hence, the definition of z_{BP} restricts it to exist in the region of the $R\pm4\sigma$, where sigma is the distal falloff width, thereby preventing possible ambiguities, and makes z_{BP} conceptually independent of the beam cross-sectional area.

Distal falloff region—This region extends from depths greater than that of the pristine Bragg peak depth, z_{BP}. The width of this region is not restricted. In many practical situations, however, the distal falloff region terminates at a depth where the dose falls below a threshold value, *e.g.*, 1% of the dose at the Bragg peak, $D(z_{BP})$.

Distal-50% depth—The distalmost depth, denoted by z_{d50}, at which the absorbed dose is equal to half of the absorbed dose at the pristine Bragg peak depth, or $D(z_{BP})/2$. For an SOBP, it is defined as the distalmost depth at which the absorbed dose is equal to half of the absorbed dose at the SOBP dose in the modulated peak region. In many cases, the dose in the modulated peak region varies with depth (perhaps by design), making selection of the absorbed dose in the modulated peak region arbitrary. Since this clearly hinders an unambiguous definition of z_{d50}, we instead define z_{d50} for an SOBP as being equal to z_b. If the dose in the modulated peak region varies with depth, z_b may have to be determined with numerical methods. Physically, the value of z_b is closely related to the R_{CSDA} value of the mean proton energy corresponding to the most energetic peak in the SOBP. Definitions for various other distal depths are similarly defined, *e.g.*, the distal-90% depth z_{d90} , z_{d50}, and z_{d20},.

Proximal-50% depth—The second most distal depth, denoted by z_{p50}, at which the absorbed dose is equal to half of the absorbed dose at the pristine Bragg peak depth, or $D(z_{BP})/2$, provided that occurs within the absorber. (For very low-energy pristine Bragg curves, the entrance dose may be greater than half the peak dose). In such cases, and for SOBPs, it is defined as the most proximal depth at which the absorbed dose is equal to half of the absorbed dose in the modulated peak region. Because of problems that are analogous to those described in the z_{d50} definition above, z_{p50} is defined as the location at which the dose is equal to half the value at depth $z_a + \Delta/2$, where Δ is the width of the transition from the peak region to the sub-peak region. Δ is not a critical parameter and it may be estimated as the amount of range straggling at z_a or it can be determined from measured Bragg curves. Conceptually, z_a typically corresponds to the shallowest location that is expected to receive the maximum dose. Physically, the value of z_a is closely related to the R_{CSDA} value of the least energetic pristine peak in the SOBP curve (or the only peak in the Bragg curve for a pristine peak). In many cases, particularly for SOBPs with large modulated-peak regions, the absorbed dose throughout the sub-peak region exceeds 50% of the value at $z_a + \Delta$, in which case proximal 50% depth is undefined. In such cases, proximal depths at higher dose percentages, such as z_{p95} and z_{p90}, may be used. If the Bragg peak occurs at zero depth, as is commonly the case for treating superficial tumors, one may simply use $z_{p100} = 0$.

80%-to-20% distal-falloff length—The distance between the distal-80% and distal-20% depths, denoted by $l_{d80\text{-}d20}$. Other distal-falloff lengths are similarly defined, *e.g.*, the 90%-to-10% distal-falloff length $l_{d90\text{-}d10}$.

Proximal-80%-to-distal-80% pristine-peak width—The distance between the proximal-80% depth and the distal-80% depth, denoted by $l_{pristine\_d80\text{-}p80}$, where the proximal-80% and distal-80% depths are defined analogously to the distal-50% depth, z_{d50}, already defined. Other pristine peak widths are similarly defined, *e.g.*, the 80%-to-80% pristine peak width. In cases where the Bragg curve does not include a proximal 90 dose point, the methods described in “Proximal-50% depth” may be used.

Proximal-80%-to-distal-80% modulated peak width—The width of the modulated peak region is defined as $l_{mod\_d80\_p80} = z_{d80} - z_{p80}$. In cases where the Bragg curve does not include a proximal 80 dose point, the methods described in “Proximal-50% depth” may be used.

Modulated-peak region—The region extending from z_a to z_b. In general, the values of z_a and z_b are most reliably determined using iterative numerical fitting methods. Conceptually, they are closely related to the proton ranges of the most and least penetrating pristine peaks in the SOBP.

These definitions may initially appear pedantic and overly precise for a conceptual understanding of proton Bragg curves. However, experience has shown that these definitions facilitate quantitative analysis and reporting of the characteristics of a wide variety of Bragg peaks in clinical and research settings. The definitions were developed from experience in manual and algorithmic analyses of measured clinical pristine and spread-out Bragg curves (Newhauser, 2001b, a; Newhauser *et al*, 2002a; Newhauser *et al*, 2002b) and for developing and commissioning proton dose algorithms for treatment planning purposes (Koch and Newhauser, 2005; Newhauser *et al*, 2007b; Koch and Newhauser, 2010). Finally, we note that in some clinical situations, the practicing medical physicist may need to define and use additional parameters, *e.g.*, z_{p98} and z_{d98}, as appropriate to a particular clinical situation or protocol. Regardless of the particular parameters chosen, it is difficult to overstate the paramount importance of using the parameters in a consistent way and being clear about their meaning when reporting results.

3.3 Model of pristine Bragg curves

In the preceding sections, we described all the major physical processes that govern the shape of proton dose distributions. Pristine Bragg curves may be calculated using a wide variety of techniques, from look-up tables of measured data to Monte Carlo simulations to analytical models. In the early days of proton therapy, indeed through the 1990s, dose algorithms in most proton treatment planning systems included very few, if any, physical models in their dose calculation algorithms. However, in the last 15 years of so, much progress has been made in modeling proton dose distributions with increasing physical completeness, realism, and accuracy. In this section, we review a method to calculate a pristine Bragg curve using a physics-based analytical model. For brevity, we present only

one model, a model that describes many of the important physical processes, is computationally straightforward and fast, and is of considerable practical value in a clinical proton setting.

Bortfeld (1997) proposed an analytical equation to calculate the Bragg curve for proton energies between 10 and 200 MeV, as follows:

$$D(z) = \Phi_0 \frac{e^{-\zeta^2/4}\sigma^{1/p}\Gamma(1/p)}{\sqrt{2\pi}\rho p \alpha^{1/p}(1+\beta R_0)}\left[\frac{1}{\sigma}D_{-1/p}(-\zeta) + \left(\frac{\beta}{p}+\gamma\beta+\frac{\varepsilon}{R_0}\right)D_{-1/p-1}(-\zeta)\right], \quad (36)$$

where D(z) is the depth dose, z is the depth, Φ_0 is the primary fluence, R_0 is the range of the proton beam, σ is the standard deviation of the Gaussian distribution of the proton depth, $\zeta = (R_0 - z)/\sigma$, α and p are material-dependent constants (defined in Equation (2)), ε is the fraction of low-energy proton fluence to total proton fluence, Γ(x) is the gamma function, and $D_y(x)$ is the parabolic cylinder function. Very good agreement is found between measured and calculated curves, and this approach has been used for the analysis and characterization of clinical proton beams (Figure 17) (Newhauser *et al*, 2002b) and for treatment planning dose calculations (Szymanowski and Oelfke, 2003; Soukup *et al*, 2005; Rethfeldt *et al*, 2006; Li *et al*, 2008).

3.4 Model of spread-out Bragg curves

Spread-out Bragg curves may be designed by combining multiple pristine Bragg curves. This approach was described in Wilson's seminal paper and its implementation was described by Koehler *et al.* (Koehler *et al*, 1977). Figure 15 plots several pristine Bragg curves and their resultant sum, which was similar to the SOBPs used at Harvard from the early 1970s onwards. The fluence is also modulated, which can be seen in the same figure as variations in the relative peak dose of each pristine Bragg curve. The range is typically modulated in steps that are small compared with the width of the Bragg peak, so that the SOBP contains little or no ripple. The modulation step size may be fixed or variable; generally the smallest step increments are needed for the deepest peaks, *e.g.*, the amplitude of the ripple decreases with depth because an increasing fraction of dose is from the sub-peak region of the Bragg curves. Figure 18 plots several typical clinical SOBPs from a contemporary proton therapy system.

SOBPs can also be modeled with analytical methods. Bortfeld and Schlegel (1996) proposed a model of the form

$$D(z) = \begin{cases} \frac{3}{4} + \frac{\sqrt{3}}{4\pi} ln\frac{1+\hat{z}^2}{1-\hat{z}+\hat{z}^2} - \frac{3}{2\pi} arctan\frac{2\hat{z}-1}{\sqrt{3}} & : \quad for \quad z < z_a \\ 1 & : \quad for \quad z_a \le z \le z_b \\ 0 & : \quad for \quad z \ge z_b \end{cases}, \quad (37)$$

where the dimensionless depth $\hat{z}$ is given by

$$\hat{z} = \sqrt[3]{\frac{z_a - z}{z_b - z_a}}, \quad (38)$$

and where z_a and z_b denote the depths of the proximal and distal extents of the SOBP (see preceding section for details of their definitions) and z is the depth in water. The model was derived with several simplifying assumptions and approximations that limit its ability to predict real SOBPs. In particular, the proton energy loss rate is based on the CSDA (*i.e.*, energy straggling is neglected) and the converted energy per unit mass approximation (where the proton energy loss and the absorbed dose in the water are assumed proportional), and non-elastic interactions of the protons with the absorber nuclei were not considered. Consequently, it does not reproduce real SOBPs well.

To attain a more realistic model, one of us (WDN) introduced terms for the finite distal-falloff distance associated with range straggling, protonic buildup effects, arbitrary slope of the modulated-peak region, and a term for the ripple in the modulated peak. In addition, the piecewise use of the function for various regions was modified to allow for a transition region between the sub-peak and modulated-peak regions, which eliminated a pronounced discontinuity there. With these additional terms and modified regions, the model becomes

$$D(z) = c_0 \Lambda \beta_{BU} \gamma \begin{cases} c_1 + \frac{\sqrt{c_2}}{4\pi} ln \frac{1+\hat{z}^2}{1-\hat{z}+\hat{z}^2} - \frac{c_3}{2\pi} arctan \frac{c_4 \hat{z}-1}{\sqrt{c_5}} & : \quad for \quad z \leq z_a - \Delta \\ m_t z + b_t & : \quad for \quad z_a - \Delta < z < z_a + \Delta \\ (mz+b) + \mathrm{Y} & : \quad for \quad z \geq z_a + \Delta \end{cases}, \tag{39}$$

where $\hat{z}$ is defined as before, c_0 is a proportionality constant, Λ takes into account the dependence on the dose due to inverse-square-law reductions in the proton fluence, β_{BU} is the secondary-particle buildup term, $c_1 \sim c_5$ are coefficients that influence the shape of the sub-peak region, and m and b are the slope and intercept the of the modulated-peak region, respectively. The ripple in the modulated-peak region is described by the term Y. The distal falloff term is denoted by γ and is modeled with a cumulative normal PDF. The transition region is centered about z_a and is of width Δ, which is a non-critical parameter that can be estimated from the amount of range straggling expected at depth z_a (see previous section for detailed definition) or it may be empirically deduced from measured Bragg curves. The extended model agrees well with measured SOBPs, several of which are shown in Figure 18. This work was previously unpublished.

3.5 Analytical transport of therapeutic proton beams

Analytical models to predict therapeutic radiation are generally simple, fast, and accurate. Early treatment planning systems, many of which were still in use in the 1990s, used dose algorithms that looked up measured profiles of absorbed dose and/or used empirical formulas. Over the last 15 years, advances in our understanding of proton therapy physics, as well as huge gains in computer speed and memory capacity, have spurred the development and clinical use of increasingly realistic and complete physical models to predict absorbed dose in patients.

The basic approach underlying most analytical dose algorithms is that the proton beam's energy loss and lateral scattering may be modeled independently from one another. The physical basis for this assumption lies in the principle of conservation of momentum and energy. Lateral scattering, which is predominantly caused by MCS, occurs at small angles (see section 2.4). Hence, the energy loss associated with the vast majority of these small

scattering events is negligible. Conversely, the predominant proton energy-loss mechanism, namely inelastic Coulomb interactions with atomic electrons, only negligibly deflects the protons because the proton mass is 1832 times greater than that of an electron (see section 2.1). Consequently, for an excellent approximation, the three-dimensional distribution of absorbed dose in a phantom or patient may be cast in the form of

$$D(x,y,z) = D(z) \cdot OAR(x,y,z), \quad (40)$$

where *x* and *y* are lateral coordinates, *z* is the depth coordinate along the beam axis, *D*(*z*) is the large-field Bragg curve (*i.e.*, with lateral protonic equilibrium, described in section 3.2), and OAR(*x, y, z*) is a term that takes into account the lateral properties of the dose distribution. Broad beam algorithms use Equation (40) with simple ray-casting techniques (Siddon, 1985) to determine the energy loss and range along each ray. Similarly, to determine the lateral extent of the therapeutic field, the rays are terminated in target-shaped final collimators by approximating them as black-body absorbers (Hong *et al*, 1996). Carefully designed broad beam algorithms are simple, fast, and accurate in media that are of relatively uniform mass density and material composition. Recently, Koch and Newhauser (2010) developed an analytical broad beam algorithm of the form

$$\frac{D(x,y,z)}{MU} = \sum_{i=1}^{N} \frac{DD_i(z_{eff})}{MU} \omega_i^{SAF} \omega_i^{RMW} \left(\frac{SSD + z_{eff}}{SSD + z} \right)^2 OAR_i \cdot \Gamma_i, \quad (41)$$

where *N* is the number of range modulation steps, ω^{SAF} is the scatter and attenuation fluence weighting factor, ω^{RMW} is the range modulator wheel (RMW) fluence weighting factor, *OAR* is off-axis ratio, and Γ is collimation modifier. This algorithm explicitly took into account edge-scattered protons and range straggling, predicted absolute dose per monitor unit (*D*/*MU)* values, and provided excellent agreement with measurements in homogeneous media, *e.g.*, for ocular treatments. In highly heterogeneous media, however, the dose at some locations may depend strongly on the material properties of the heterogeneities in the overlying tissue, and therefore the approach of casting a single ray does not, in general, provide sufficient dosimetric accuracy.

To improve the dosimetric accuracy in heterogeneous media, the dose may be calculated at a point as the superposition of multiple pencil beams. A pencil beam is, in essence, a mathematical construct that has no exact and direct analogy in the physical world, but it is resembles a beam of infinitesimally small lateral size. By superposing enough pencil beams, the physical dose distribution can be modeled. Fortunately, as we shall see, many of the physical principles and algorithmic aspects from the broad beam approach are directly applicable to the pencil beam algorithm.

Hogstrom *et al.* (1981) originally proposed a pencil beam algorithm for electron therapy. Basically, an ion beam is divided into a number of finite pencil beams and the dose distribution of each pencil beam is described by the multiplication of a central-axis term and an off-axis term. The final relative absorbed dose to any point in the patient (D_p (*x, y, z*)) is the summation of the dose contributions from all the pencil beams:

$$D_p(x,y,z) = \int\int \mathrm{d}x'\mathrm{d}y' S\left(x',y'\right) PDD\left(z_{eff}\right) \left(\frac{SSD+z_{eff}}{SSD+z}\right)^2 \frac{1}{2\pi\sigma_{tot}^2(z)} exp\left(-\frac{\left(x'-x\right)^2+\left(y'-y\right)^2}{2\sigma_{tot}^2(z)}\right), \quad (42)$$

where $S(x', y')$ is the relative intensity of the pencil beam at x', y', $PDD(z)$ is the central-axis percentage depth dose, SSD is the source-to-surface distance, z_{eff} is the effective depth of the point, and σ_{tot}^2 describes the final lateral distribution of a pencil beam by taking into account the MCS contributions from each beam-modifying device and from the patient. Many other groups have subsequently adapted and extended this concept for application in proton therapy (Petti, 1992; Hong *et al*, 1996; Schaffner *et al*, 1999; Szymanowski and Oelfke, 2002; Ciangaru *et al*, 2005; Schaffner, 2008; Westerly *et al*, 2013). Contemporary proton pencil beam algorithms provide excellent accuracy (Newhauser *et al*, 2007b), especially in homogeneous media, superior to that of broad beam algorithms in heterogeneous media. The improvement in accuracy comes mostly at the cost of greater computation times. Because of approximations in the pencil beam algorithm, it may not provide sufficient accuracy in extremely heterogeneous media, at material and/or density interfaces, or in other complex situations.

Currently, most proton therapy clinics utilize commercial treatment planning systems that contain pencil beam algorithms for calculation of therapeutic dose distributions. Computation speeds are generally sufficiently fast for most routine planning.

3.6 Monte Carlo transport of therapeutic proton beams

Monte Carlo transport technique has been used increasingly in radiation therapy (Seco and Verhaegen, 2013). It is more accurate than analytical models in that it takes into account the physical processes during particle transport. The most commonly used general purpose Monte Carlo codes for proton therapy research are MCNPX (Pelowitz, 2011), Geant 4 (Agostinelli *et al*, 2003), and FLUKA (Ferrari *et al*, 2005). Several groups have developed special purpose Monte Carlo codes, *e.g.*, a treatment planning dose engine (Tourovsky *et al.*, (2005); Yepes *et al.*, (2009a)), typically with faster computation speed but fewer features than general purpose codes. Here we focus mainly on applications that use the MCNPX code because it is representative of most general purpose codes, we are most familiar with it of any of the codes, and constraints on journal space do not allow discussion of all codes.

The main components of a Monte Carlo simulation model are a source of protons, a treatment head, and a patient or phantom (figure 19). The proton source is typically taken as being incident on the treatment head (beamline transport is not usually simulated), where the source parameters are deduced from dose profile measurements (Newhauser *et al*, 2005) or taken from other beam properties, *e.g.*, from the manufacturer (Newhauser *et al*, 2007b). The model of a treatment head typically includes all major mechanical components, *e.g.*, a vacuum window, a beam profile monitor, a range modulator wheel, a second scatter, shielding plates, a range shifter assembly, backup and primary monitors, the snout and the brass collimator, and a patient-specific range compensator (Zheng *et al*, 2007b; Perez-Andujar *et al*, 2009). Models of scanned beams may model the magnetic field and transport the proton beam deflection (Peterson *et al*, 2009; Dowdell *et al*, 2012), or the proton source

may be pointed, *e.g.*, using the “thin lens” approximation to increase computation speed (Lee, 2004). The patient may be represented in voxels whose material composition and mass density are deduced from three-dimensional CT images of the patient (Taddei *et al*, 2009). The matrix of Hounsfield unit values in these voxels may be converted into corresponding matrices of material composition and mass density values based on a tri-linear calibration curve (Newhauser *et al*, 2008a). A simulation capability to accommodate time-dependent geometry was reported by Paganetti *et al.* (2005). Some useful applications of the Monte Carlo method are described here:

1) Alternative or complimentary source of dosimetric data for developing, configuring, and validating analytical dose algorithms in clinical treatment planning systems. At least two studies revealed that, after a significant development effort, a Monte Carlo model of a proton therapy apparatus is sufficiently accurate and fast for prospective commissioning of an ocular treatment planning system (Koch and Newhauser, 2005; Newhauser *et al*, 2005) and a large-field treatment planning system (Newhauser *et al*, 2007b). This prospective capability reduced the time required for preclinical work by several months, resulting in substantial cost savings. Studies about scanning proton beam configuration have also been reported (Tourovsky *et al*, 2005; Sawakuchi *et al*, 2010; Dowdell *et al*, 2012).

2) Alternative dose engine to calculate absorbed dose in phantoms or patient. In clinical practice, there frequently arise challenging cases where the accuracy of analytical models is unknown or suspected to be insufficient. In many such cases, measurements are not possible or practical, *e.g.*, intracranial *in vivo* range verification. Multiple groups have developed Monte Carlo treatment planning engines (Tourovsky *et al*, 2005; Newhauser *et al*, 2008b; Perl *et al*, 2012; Mairani *et al*, 2013) based on various Monte Carlo codes, independently proving the technical feasibility of this approach. The physics of general purpose Monte Carlo codes for this purpose has been exhaustively validated against benchmark measurements in therapeutic proton beam data (Polf JC, 2007; Kimstrand *et al*, 2008; Titt *et al*, 2008a; Randeniya *et al*, 2009). Just 10 years ago, the slow execution times, memory constraints, unknown accuracy, and unknown technical feasibility of a full-blown Monte Carlo engine were serious research challenges. Today, the only major remaining obstacle to routine use of Monte Carlo engines for treatment planning is their slow execution times. For example, a proton craniospinal treatment simulation took more than 10^4 CPU hours (Taddei *et al*, 2009). Encouragingly, however, algorithmic improvements have increased speeds dramatically; Zhang *et al.* (2013a) found that using lattice tally in MCNPX can speed up dose simulations by one order of magnitude compared to mesh tally, especially for dose reconstructions involving large numbers of voxels. The physics of the radiation transport are identical for the lattice and mesh tallies, *i.e.*, there was no loss of accuracy. Yepes *et al.* (2009b) recently reported on a fast dose calculator, a Monte Carlo track-repeating algorithm that uses a database of precomputed proton trajectories in water and applies these trajectories to heterogeneous media by scaling the proton range and scattering

angles. This approach reduced the computation time for dose reconstruction in voxelized patient geometry by more than two orders of magnitude compared to MCNPX and GEANT4 (Yepes *et al*, 2009a; Yepes *et al*, 2010a). The use of low-cost alternative parallel computer architectures also appears promising, including the use of graphics processing units (Yepes *et al*, 2010b; Jia *et al*, 2012) and grid technologies (Vadapalli *et al*, 2011).

3) Assessment of beam perturbation due to objects implanted in patients and development of mitigating strategies. The proportion of cancer patients with implanted devices is probably less than 10%, but it is increasing along with the aging of the population, increasing life expectancies, and increasing use of implanted devices. Examples include cardiac pacemakers, defibrillators, fiducial markers for radiotherapy localization, permanent radioactive seed implants, stents, prostheses, surgical reconstructive devices, and foreign bodies such as gunshot and shrapnel. Analytical dose algorithms in contemporary clinical treatment planning systems lack the capability to reliably assess dose perturbations from most implants. Several studies reported that implanted metallic fiducials can cause dose shadows that may compromise local tumor control for certain diseases, *e.g.*, prostate carcinoma and uveal melanoma (Newhauser *et al*, 2007a; Newhauser *et al*, 2007c; Giebeler *et al*, 2009; Cheung *et al*, 2010; Huang *et al*, 2011; Matsuura *et al*, 2012; Zhang *et al*, 2012; Carnicer *et al*, 2013).

4) Investigation of characteristics of therapeutic beams and beamlines. For example, edge-scattered protons can degrade the dose distribution, and the effect is difficult to model with current analytical models. Accurate predictions of D / MU require taking into account the dose from protons scattered from the edge of the patient-specific collimator, particularly for small field sizes and large depths (Titt *et al*, 2008b). Currently available spot scanning system only offer few options for adjusting beam spot properties like lateral and longitudinal size, and Monte Carlo simulations was used to optimize scanned beam spot (Titt *et al*, 2010). Because the Monte Carlo simulation technique is inherently general, it can be applied to virtually any problem involving the transport of protons or secondary radiation. Space constraints prevent us from reviewing more than a few illustrative examples. In later sections we briefly mention roles for Monte Carlo methods in research on stray radiation exposures to patients (section 5) and shielding barriers to protect staff (section 6).

4. Therapeutic absorbed dose determination

4.1 Reference dosimetry

By reference dosimetry, we mean the determination of absorbed dose in a manner that allows it to be directly related or referred to an accurate and uniform standard of absorbed dose. Clinical reference dosimetry comprises the measurement of absorbed dose in a clinic, which is related to the absorbed dose at a primary or secondary standards laboratory. This approach ensures that clinical reference dosimetry is accurate and uniform across participating institutions. Typically, clinical reference dosimetry is established by first

calibrating a clinic's dosimeter at a standards laboratory, then “transferring” the calibration to the clinic's treatment beams. To minimize systematic errors introduced by this transfer process, both irradiations are made with the same dosimeter and under identical (or very similar) “reference conditions”. Therefore, reference conditions must be reproducible and clinically relevant. However, national or international calibration laboratories do not yet produce proton calibration beams of relevance to proton therapy (presumably due to prohibitively high costs, low demand, and limited resources). Because of this limitation, the proton therapy community developed alternative methods for proton reference dosimetry.

For many decades, the reference fields for calibrating proton dosimeters were characterized using a Faraday cup (Verhey *et al*, 1979) to measure the proton fluence in air. Today, most proton therapy institutions implement reference proton dosimetry utilizing an ionization chamber technique to measure the absorbed dose to water. With the latter technique, an ionization chamber is calibrated using reference conditions for photon therapy (*i.e.*, ^{60}Co radiation fields that are widely available at calibration laboratories) and a correction factor is applied that corrects the differences in the chamber's response to ^{60}Co and proton beams. When implemented properly, the techniques agree within uncertainties (Newhauser *et al*, 2002a; Newhauser *et al*, 2002b).

Several advisory bodies have published dosimetry protocols for reference dosimetry, such as the American Association of Physicists in Medicine (AAPM, 1986), the European Clinical Heavy Particle Dosimetry Group (ECHED) (Vynckier *et al*, 1991, 1994), the International Commission on Radiation Units and Measurements (ICRU, 1998, 2007), and the International Atomic Energy Agency (IAEA, 2000). Vatnitsky *et al.* (1999a) perfomed an international proton dosimetry inter-comparison based on the ICRU Report 59 protocol (ICRU, 1998) and reported that absorbed dose to water can be delivered within 3%.

4.2 Patient field–specific dosimetry

The determination of absolute absorbed dose per monitor unit for each patient and treatment field, denoted by *D/MU*, rests upon the foundation of reference dosimetry. Recall that reference dosimetry is performed under simple and reproducible conditions, *e.g.*, using a dosimeter in a water-box phantom. In contrast, dosimetry in a patient should take into account the full complexity of a patient's anatomy, *e.g.*, irregular surface shapes, heterogeneous elemental composition and mass density, and treatment field size and shape. These additional complexities call for a conceptual framework and measurement techniques for performing routine *D/MU* determinations for patient treatment fields.

For several decades, *D/MU* values for passively scattered treatment beams were typically measured at depth in a water-box phantom the range compensator present. However, a systematic study by Fontenot *et al.* (2007) that measuring *D*/*MU* without the range compensator present provided more reliable results because use of the range compensator increased the severity of dose gradients near the calibration point and this resulted in larger overall uncertainties in *D/MU*. It is not known if this finding holds for special cases, *e.g.*, small diameter treatment beams, large air gaps, and moving targets. In many practical situations, it is convenient or necessary to predict the absolute dose in a patient based on the corresponding dose under reference conditions (*e.g.*, a water phantom). Because an exact

theoretical approach is not possible, all approaches have utilized approximate methods, numerical calculations, measurements, or a combination of these. On the basis of previous studies, Newhauser *et al.* (2014a, b) reported the following method to calculate proton dose in a patient $(D/MU)_{\mathrm{p}}$:

$$\begin{aligned}\left(\frac{D}{MU}\right)_{\mathrm{p}} &= \left(\frac{D}{MU}\right)_{\mathrm{w}} \cdot F_{CSPS} \\ &= \left(\frac{D}{MU}\right)_{\mathrm{w}}^{ref} \cdot F_{OF} \cdot F_{RS} \cdot F_{SOBP} \cdot F_{InvSq} \cdot F_{FS} \cdot F_{ColS} \cdot F_{CSPS},\end{aligned} \tag{43}$$

where $(D/MU)_{\mathrm{w}}$ is the D/MU in a water phantom under patient-specific field conditions; F_{CSPS} is the compensator scatter and patient scatter factor, which takes into account differences in the scattering and attenuation of the patient and range compensator together relative to that of water and no range compensator; $(D/MU)^{\mathrm{ref}}{}_{\mathrm{w}}$ is the D/MU in a water phantom under reference conditions and is 1 cGy/MU; F_{OF} corrects for proton beam energy spectrum relative to the reference condition; F_{RS} corrects for range shifter effect; F_{SOBP} corrects for SOBP relative to the reference field; F_{InvSq} corrects for beam divergence relative to the reference condition; F_{FS} corrects for field size effect; and F_{ColS} corrects for differences in scatter from the reference aperture (10 cm × 10 cm) to the patient-specific aperture. They found that for prostate treatment fields, found that uncertainty in F_{CSPS}, which is the least well understood factor, was clinically acceptable for prostate treatment (Newhauser *et al*, 2014b). In a companion study, the same group reported the variability in F_{CSPS} was clinically significant for some lung treatment fields (Newhauser *et al*, 2014a).

For scanning proton beams, it is important to calibrate individual spot beam because patient specific collimating apertures or range compensators are not typically used in the beam line. First the number of protons per MU for each beam energy is calibrated by Faraday-cup measurements or Monte Carlo simulations. Then, either physical model or Monte Carlo simulation can be used to calculate absolute dose normalized to the number of incident protons. A simple nuclear halo model was developed at Paul Scherrer Institute (PSI) (Pedroni *et al*, 2005) to include secondary dose around the primary pencil beam and can predict precisely the dose directly from treatment planning without renormalization measurements.

In addition to the physical effects already discussed above, there are many additional effects that contribute to the uncertainty in *D/MU* that arise from imperfections in anatomic images used for treatment planning, organ motion, and in the case of scanned beams, the interplay of organ motion and the moving beam, etc. Such uncertainties may depend strongly on anatomical site, approximations utilized by the treatment planning system, beam delivery system, and experimenter's skill. Ideally, clinical treatment planning systems would provide accurate estimates of $(D/MU)^{\mathrm{ref}}{}_{\mathrm{w}}$ and $(D/MU)_{\mathrm{p}}$ with known and small uncertainties, methods for determining and reporting $(D/MU)_{\mathrm{p}}$ would be standardized, and secondary methods (*e.g.*, hand calculations similar to Eq. 43 or fast Monte Carlo simulations) would be available to independently verify $(D/MU)_{\mathrm{p}}$ values determined with the primary method. In principal, it appears to be adequate knowledge of basic proton interaction physics and transport physics to reach or approach these clinical ideals. In addition, recent research studies report encouraging results for a variety of special cases, *e.g.*, for a particular

treatment technique, treatment planning system, or treatment delivery systems. As mentioned in section 3.5, Koch and Newhauser (2010) developed an analytical broad beam algorithm to predict absolute dose per monitor unit (*D* / *MU)* values with good accuracy in water for ocular proton treatments, but the ability to predict *D* / *MU* in the heterogeneous patient body still needs improvement. To date, the methods for determining $(D/MU)_p$ in the literature have not yet been validated for general application or standardized.

5. Stray Radiation

As with other forms of external-beam radiation beams, proton beams unavoidably produce stray radiation that impinges on the patient's entire body (Fig. 20). In the 1990s, very little was known about the exposure of patients to stray radiation produced by therapeutic proton beams. By the mid 2000s, concerns about stray radiation had become a matter of considerable speculation and controversy, particularly regarding the suitability of proton beams for treating children with cancer because of concerns about the risks from stray neutron exposures (Hall, 2006; Brenner and Hall, 2008). By the late 2000s, research on stray radiation exposures from proton and other radiation therapies had intensified and some questions have been partially or fully answered. However, many questions remain open. In this section, we review selected developments and discuss a few open questions.

In a study using Monte Carlo simulations, Agosteo *et al*. (1998) reported that neutron exposures were the principal concern among the various types of stray radiation from proton therapy. Comprehensive measurements in clinical proton therapy beams were reported by Yan *et al.* (2002), including neutron spectral fluences and dose-equivalent data for large-field, radiosurgery, and ocular beamlines. That study included measurements of neutron energy spectra and neutron dose-equivalent values. Several other groups have measured neutron exposures, including Roy and Sandison (2004), Tayama *et al.* (2006), Mesoloras *et al.* (2006), Schneider *et al*. (2002) and Wroe *et al*. (2007). The early measurements were important because they suggested that the neutron exposures, while generally small in comparison to therapeutic doses, should not be neglected.

Several groups developed neutron dose reconstruction systems based on general purpose Monte Carlo codes for a wide variety of clinical proton beamlines (Siebers, 2000; Fontenot *et al*, 2005b; Jiang *et al*, 2005; Polf and Newhauser, 2005; Newhauser *et al*, 2007b; Zheng *et al*, 2007b; Moyers *et al*, 2008; Newhauser *et al*, 2008b). A wide variety of simulation approaches have been used, with varying degrees of clinical realism, assumptions, and approximation, and not surprisingly, rather disparate results. Some of the literature on measurements and simulations of neutron exposures was reviewed in NCRP Report 170 (2011). In the remainder of this section, we emphasize progress subsequent to that report.

Research methods of relevance to stray radiation estimation have progressed dramatically since Agosteo *et al* (1998) published their pioneering study using Monte Carlo simulation to study neutron fluence and dose in air or in a simple water box phantom. One key advance was the validation of Monte Carlo predictions against benchmark neutron measurements, for example the studies of Tayama *et al.* (2006), Fontenot *et al*. (2005a), and Polf *et al*. (2005). High-performance computing techniques, such as using massively parallel computing

clusters, allows fast simulations of whole-body dose reconstructions involving complex treatment techniques, *e.g.*, craniospinal irradiation (CSI) (Newhauser *et al*, 2009; Taddei *et al*, 2009; Taddei *et al*, 2010b; Perez-Andujar *et al*, 2013a; Zhang *et al*, 2013c), which is widely considered one of the most challenging treatments to simulate. Another key advance was increasing the level of realism in modeling anatomy. Methods have progressed in 1998 from simple water-box phantoms to stylized anthropomorphic phantoms to generic voxelized phantoms in the mid 2000s to patient-specific personalized phantoms by the late 2000s (*i.e.*, by retrospectively using treatment planning CT scans). In fact, this year a study was completed comprising a 17-patient *in silico* clinical trial comparing proton CSI and photon CSI, according to the contemporary standards of care, including full Monte Carlo simulations of stray and therapeutic exposures (Zhang *et al*, 2014).

Another research result of considerable clinical relevance is that it is possible and indeed feasible to dramatically reduce exposures from stray neutrons that leak out of the treatment apparatus. For example, Taddei *et al.* (2008) found that modest modifications of the treatment unit (adding shields near the patient, using a tungsten-alloy collimator, and adding an upstream collimator near the range shifter assembly) substantially reduced the neutron dose (by 66%) for patients receiving passively scattered proton therapy for prostate cancer. Similarly, Brenner *et al.* (2009) investigated various precollimator/collimator combinations with different geometries and materials and concluded that an optimized design can be achieved to significantly reduce the stray neutron dose.

Despite the rapid growth of research on stray neutron radiation exposures to patients, the literature is mainly limited to a few case studies and anatomical sites. In general, the knowledge of stray radiation from proton therapy is still largely incomplete. The gaps in knowledge received considerable attention following the cautionary paper by Hall *et al* (2006), who suggested that the use of advanced radiotherapy modalities like proton therapy may not be justified because of incomplete knowledge of stray neutron exposures and second cancer induction. From subsequent studies, a coherent picture is gradually emerging: second cancer risk following proton therapy is lower than that after photon therapy for patients, the risk differential depends strongly on anatomic site and other host and treatment factors, the risk posed by stray radiation is small but not negligible, and the largest reductions in risk are achieved by using scattered- or scanned-proton beams instead of photon beams. Furthermore, the majority of risk of radiogenic second cancer is from in-field radiation, not out-of-field radiation. Consequently, the difference in predicted total risk (from both in-field and out-of-field radiation) from scanned *versus* scattered proton treatments is small and clinically negligible. At the risk of oversimplification, the theoretical risk advantage of proton therapy derives mainly from its ability to spare healthy tissues that are distal and lateral to the target volume. With judicious treatment techniques (*e.g.*, beam orientations, location of field junctions, etc.), it is possible in many cases to utilize the rapid distal and lateral dose falloff of proton beams to reduce the dose to sensitive organs and tissues to below levels achievable with technologically comparable photon treatments.

It is worth underscoring that our knowledge and understanding of this topic in incomplete and likely to evolve substantially in the future. Current dose and risk assessments are mostly based on standard-of-care treatment plans, i.e., using clinical planning and research systems

that not attempt to algorithmically minimize risk of radiation side effects. As clinical treatment planning systems are incrementally extended with these capabilities, the standards of care for proton and photon therapies will continue to evolve. This evolution will likely render our current understanding of radiation risks obsolete.

5.1 Monte Carlo simulations

During the transport of proton beams through the treatment unit to the patient, not only is therapeutic radiation deposited in the patient but also stray radiation is generated because of nuclear interactions (as explained in section 2.4). In proton therapy, secondary neutrons are dominant among this stray radiation and are a major concern (Agosteo *et al*, 1998; Fontenot *et al*, 2008). Estimation of stray neutron dose can be challenging and time consuming, and the variations in measurement or calculation results can be large (Xu *et al*, 2008).

The inherent accuracy of Monte Carlo simulation makes it an irreplaceable tool for stray neutron dose estimation, and indeed this technique has been used by many investigators studying stray neutrons generated during proton therapy (Agosteo *et al*, 1998; Jiang *et al*, 2005; Zheng *et al*, 2007a; Moyers *et al*, 2008; Zacharatou Jarlskog and Paganetti, 2008; Zheng *et al*, 2008; Newhauser *et al*, 2009; Taddei *et al*, 2009; Athar *et al*, 2010; Taddei *et al*, 2010a; Taddei *et al*, 2010b; Zhang *et al*, 2013b). Using MCNPX, both external neutrons (neutrons generated in the treatment unit) and internal neutrons (neutrons generated within the patient's body) can be accurately simulated (Taddei *et al*, 2009).

Polf and Newhauser (2005) found that neutron dose equivalent per therapeutic absorbed dose (H / D) at different locations around a passively scattered proton therapy unit increased with increasing range modulation and that the major source of neutrons shifted from the final collimator to the range modulation wheel. Zheng *et al.* (2007a; 2007b) reported that H/D generally increased with decreasing collimating aperture size, increasing proton beam energy, and increasing SOBP width, while it decreased with snout distance from the isocenter and increasing distance from the treatment unit. More than 50% of the neutron dose at all locations was from neutrons with energies higher than 10 MeV. Zheng *et al.* (2008) also reported that neutron spectral fluence contained two pronounced peaks, a low-energy peak around 1 MeV and a high-energy peak that ranged from around 10 MeV up to the proton energy. The mean neutron radiation weighting factors varied only slightly, from 8.8 to 10.3, with proton energy and location for a closed-aperture configuration.

5.2 Analytical model

Because of the complexity associated with Monte Carlo simulation and measurement, a simple analytical model to predict stray neutron dose in proton therapy is desirable. Zheng *et al.* (2007b) proposed an exponential decay model to predict H / D in air with good accuracy. This largely empirical model was extended by Zhang *et al.* (2010a) to predict H / D both in air and in the patient's body by taking into account off-axis effect, phantom attenuation effect, and low/high energy peaks observed in neutron spectral fluence. Perez-Andujar *et al.* (2013b) subsequently enhanced the model by replacing empirical components with physics-based components, obtaining

$$(H|D)_d=(H|D)_{iso}(d|d_{iso})^{-p}\left[\begin{array}{ll} C_1e^{-\alpha_1\left(d'-d'_{iso}\right)}e^{-\left(x^2+y^2\right)d_{iso}^2/2\sigma_1^2z^2}+C_2e^{-\alpha_2\left(d'-d'_{iso}\right)}e^{-\left(x^2+y^2\right)d_{iso}^2/2\sigma_2^2z^2} & \cdots \\ C_3e^{-\alpha_3\left(d'-d'_{iso}\right)}e^{-\left(x^2+y^2\right)d_{iso}^2/2\sigma_3^2z^2}+C_4e^{-\alpha_4\left(d'-d'_{iso}\right)}e^{-\left(x^2+y^2\right)d_{iso}^2/2\sigma_4^2z^2} & \end{array}\right], \quad (44)$$

where $(H/D)_{iso}$ is the neutron equivalent dose per therapeutic absorbed dose at isocenter. C_1, C_2, C_3, and C_4 apportion the *H/D* contributions from intranuclear cascade, evaporation, epithermal, and thermal neutrons, respectively. $(d / d_{iso})^{-p}$ represents the power law that governs the neutron dose falloff as a function of distance from the effective neutron source, which is independent of the proton beam energy, d represents the distance from the neutron source in the treatment nozzle to the detecting volume and d_{iso} is the distance from the neutron source to isocenter. α_1, α_2, α_3, and α_4 denote the attenuation coefficients of intranuclear cascade, evaporation, epithermal, and thermal neutrons, respectively. d'_{iso} is the distance from the phantom surface to the isocenter, and d' is the distance from the phantom surface to the detecting volumes. The lateral distribution of neutrons is governed by σ_1 for intranuclear cascade, σ_2 for evaporation, σ_3 for epithermal, and σ_4 for thermal neutrons. z is the vertical coordinate for the neutron dose receptor and is used to scale the width parameters.

The accuracy of this model is comparable to the accuracy of typical Monte Carlo simulations or measurements of neutron dose (Figure 21). Taddei *et al*. (2013) modified the model reported by Zhang *et al.* (2010a) and used a simplified double-Gaussian model to calculation out-of-field dose in photon therapy and they also had good agreement between measurement data and model-based values.

This model and the follow-up research from our group (to extend the model for multiple energies and to implement this model in commercial treatment planning systems) push the possibility of calculating the plan-specific out-of-field dose delivered to the patient during both proton and photon therapy.

6. Shielding Design

In this section, we will briefly review the design of shielding to protect humans from stray radiation. In particular, we will focus on the bulk shielding barriers (*e.g.*, walls, ceilings) and mazes. Bulk shielding is an extremely important aspect of facility design because proton therapy equipment is capable of producing lethal levels of stray radiation. In addition, bulk shielding intrudes on space available for equipment and personnel and it is expensive. In many ways, the design of bulk shielding is a classical engineering problem; one develops a solution that comprises an acceptable balance of the competing attributes of safety, utility, and cost.

Broadly, to design shielding one must have knowledge of the stray radiation production, transport, and attenuation in shielding barriers. In addition, the shielding design goals, *i.e.*, the predicted exposure rate at an occupied location, depend on the fraction of time an area is occupied, its designation as a controlled or uncontrolled area, and the type of individuals present, *i.e.*, patients, staff (radiation workers) and the general public. There are typically multiple design goals to be satisfied, *e.g.*, one for short term exposures (averaged over one

hour) and one for long term exposures (averaged over one year). In general, one does not know *a priori* which design goal will ultimately govern the shielding design, necessitating shielding calculations that represent multiple scenarios.

Before discussing the basic physics of shielding design, we digress briefly to point out that shielding barriers are one of several necessary components of an effective radiation protection program. Shielding barriers alone do not ensure safety. It is impractical, not to mention prohibitively expensive, to build shields that by themselves provide adequate protection for unrestricted usage of contemporary proton therapy systems. Administrative controls on beam usage are therefore necessary and, for obvious reasons, the anticipated beam usage must be taken into account in the shielding design process. Knowledge of the proton beam usage is often difficult to predict, particularly for first-of-kind treatment units where neutron production in the beam production and delivery systems are poorly known. In addition, the future outcome of a clinical trial or a change in health care policy may dramatically change proton beam usage. Leaving these uncertainties aside, one needs to know not only the beam usage (energies, charges and currents, and directions of travel) at each of the treatment locations, but also all of the corresponding proton loss rates in the accelerator, energy selection system, beam transport system, and treatment head. The loss proton losses and neutron production vary strongly on the proton beam energy and other factors (see Fig. 22), necessitating separate calculations for several proton beam energies (Newhauser *et al*, 2002d). Many aspects of shielding of proton therapy facilities are similar to those for photon therapy facilities, which have be reviewed in detail elsewhere (NCRP, 2008).

On the assumption that the beam usage, occupancy factors, and other aspects are known, one may calculate the neutron dose equivalent rate at a point of interest behind a slab shielding barrier (*e.g.*, wall, ceiling, *etc.*) that is parallel to and at a distance *a* the proton beam according to

$$H\left(E_p,\theta,\frac{d}{\lambda(\theta)}\right)=\frac{H_o(E_p,\theta)}{r^2}exp\left[\frac{d}{\lambda(\theta)\ cos(\alpha)}\right], \quad (45)$$

where $H(E_p, \theta, d/\lambda)$ is the ambient dose equivalent beyond the shield, E_p is the proton beam energy, θ is the emission angle from the proton loss point and the point of interest, r is the distance between the proton loss point and the point of interest, d is the thickness of the shield, $\lambda(\theta)$ is the attenuation length of the shield material, $H_o(E_p, \theta)$ is the source term, α is the angle of incidence of the radiation impinging on the shield (Agosteo, 2009). This semi-empirical approach, based on the work of Moyer (Moyer, 1962), has many attractive attributes, including the inclusion of major dependencies, simplicity, and computational speed. Five decades on, in spite of its limitations, the Moyer model still is widely used, especially in cases where speed and convenience are more important than accuracy.

Personnel must be able to ingress to and egress from access shielded vaults quickly, *e.g.*, for efficient routine clinical operation, in emergencies such as attending to a sick patient, and to maintain and repair the accelerator and beam transport system. This necessitates large openings in the bulk shielding walls. Obviously such openings result in a reduction in

attenuation that must be restored. Typically the required attenuation is restored by fitting the opening with a long and curved shielding tunnel, commonly referred to as a maze or labyrinth. The maze attenuates radiation that is incident upon it in two ways: its walls attenuate the deeply penetrating radiation that is incident on the maze walls, and it attenuates the less-penetrating radiation that enters the opening of the maze by a combination of scattering and absorption processes as the radiation propagates through of the maze.

Typically the mazes of treatment rooms are not equipped with massive shielded doors because they can significantly increase access times. On the other hand, infrequently accessed vaults (*e.g.*, for the accelerator and beam transport system) commonly utilize a maze equipped with a massive shielding door.

The dose equivalent rate outside the maze (without a door) from scattered radiation that enters the maze entrance (inside the vault) is given by

$$H\left(r_1, r_2, r_3, \ldots, r_n\right) = \frac{2a^2 H_o\left(a\right)}{r_1^2} \prod_{i=2}^{n} f_i\left(r_i\right), \quad (46)$$

where r_1 is the line of sight distance from the source to the point of interest in the first (closest to the source) leg of the maze maze, H_o(a) is the dose equivalent at distance a from the source, a is distance from the source to the entrance of the first leg, and $f_i(r_i)$ are attenuation factors for the subsequent legs of the maze (Tesch, 1982). These are given by

$$f\left(r_i\right) = \frac{e^{-r_i/0.45} + 0.022 A_i^{1.3} e^{-r_i/2.35}}{1 + 0.022 A_i^{1.3}} \quad (47)$$

where r_i is the distance from entrance of the i^{th} leg to the point of interest in that leg, and where A_i is the cross sectional area of the i^{th} leg of the maze (Agosteo, 2009). In addition, one must still (separately) consider attenuation of radiation impinging upon the outside of the maze walls (*e.g.*, using the Moyer model) and the attenuation in maze doors, in cases where they are used. The attenuation of the maze increases with the number and length of the legs, the thickness of the maze walls, and decreases with cross sectional area. It would be difficult to overemphasize the high relative importance of the design of the mazes. Fortunately, there are available several design methods that are well understood, accurate, and that have been validated with measurements in clinical proton therapy facilities.

Materials used for the bulk shielding barriers and mazes vary somewhat, depending on the cost and availability of the shielding materials and the cost of space occupied by the shielding barriers. Typically, ordinary concrete with steel reinforcement is utilized because of its large hydrogen content and mass density (2.35 g/cm^3), high strength, good availability, and low cost. Contemporary proton therapy centers use concrete shielding barriers of up to several meters thick (Newhauser *et al.*, 2002; Titt and Newhauser, 2005). The neutron attenuation length, or the thickness required to reduce the incident fluence by a factor of 1/e, is plotted in Figure 23 for ordinary concrete. At the high-energy limit, the attenuation length is approximately 50 cm of ordinary concrete (Moritz, 2001). The density and attenuating properties of concrete can be increased substantially by utilizing high-density aggregate material, but cost prohibitive in most cases. Some facilities have utilized comparatively

small “local” shields, e.g., to shield beamline components that produce copious quantities of neutrons, to lessen the attenuation requirements of larger bulk shields. In some cases, higher density materials such as alloys of iron (7.9 g/cm^3) or tungsten (19.25 g/cm^3) may be advantageous for shielding against high-energy neutrons because they can be made more compact than with concrete or other bulk shielding materials. Proton beam stoppers, which prevent the primary proton beam from impinging on the bulk shielding, have been made from a variety of materials, including plastic and steel.

The shielding design methods most often used for proton therapy facilities are analytical methods and Monte Carlo simulations. The knowledge of the uncertainties in predictions from both of these methods is incomplete. Newhauser *et al.* (2002c) measured, calculated (using semi-empirical analytical models that were developed for slab and maze shielding geometrics), and simulated neutron dose rates at a 235-MeV proton therapy center, and they found that the analytical model overestimated neutron dose at most positions compared to measurements, while Monte Carlo simulations agreed more closely with the measurements. However, the Monte Carlo method is considerably more challenging because of the need to obtain convergence of solutions; generalized and automated variance reduction techniques are lacking. Titt and Newhauser (2005) evaluated the uncertainty associated with Monte Carlo shielding technique by comparing the analytical predictions with detailed Monte Carlo simulations of neutron equivalent doses at various receptor locations. They found the optimum rejection criterion to be 10% statistical uncertainty for the Monte Carlo simulations. This rejection criterion provided additional confidence because virtually all accepted simulated results had converged.

In an unpublished study, one of us (WN) estimated the cost of concrete and steel used for shielding a typical multi-room proton therapy at approximately 6M USD, with the potential to reduce shielding costs by almost one third through improved neutron shielding designs. Evidently there is considerable potential to achieve cost savings and other benefits by developing improved shielding design methods and to optimize shield designs.

Although we have not discussed small local shields of beamline components in this section, there is considerable overlap with the material presented in the previous section, for brevity we shall not consider stray radiation inside of a treatment room here.

7. Challenges and Future of Proton Therapy

The future utilization of proton therapy is difficult to predict. There are some tentative indications that it will continue to become more widely available in developed countries, perhaps owing to the clear theoretical dosimetric advantages associated with proton beam dose distributions. Perhaps the strongest argument in favor of protons is actually an indirect counter argument: there is only sparse evidence of beneficial effect from unnecessary irradiation of healthy tissues (*i.e.*, from the exit dose of photon beams) (Terasawa *et al*, 2009). Other arguments in favor include an excellent record of treatment safety and efficacy. Furthermore, over the past 15 years, many arguments against proton therapy have been largely or fully disproved, *e.g.*, it is too complex and too difficult for most clinical

organizations, manufacturers cannot be counted upon to deliver systems on schedule, the range uncertainty is too large, and the risks from stray neutron doses are too great.

Nonetheless, skepticism and controversy remain regarding the likely ultimate role of proton therapy in radiation oncology. Especially in the last few years, the debate seems to focus on cost-effectiveness and cost-competitiveness. Basically, the argument goes, the cost and value of proton therapy has not been proven with evidence of improved patient outcomes, which are presumed to offset some or all of the higher costs of proton therapy systems. If the price differential between proton and photon therapies were to substantially shrink or disappear, *e.g.*, due to economies of scale, many clinics would replace at least some photon treatment units with proton units.

For all these reasons, there are many urgent research questions of relevance to proton therapy. Some of these are enumerated here, with an emphasis on those questions that will require physics research and development to reduce cost, improve treatment quality and efficiency, and create previously new treatment capabilities of clinical importance.

1) Can novel techniques, such as proton arc therapy (Sandison *et al*, 1997; Sengbusch *et al*, 2009; Rechner *et al*, 2012), be developed to improve the quality of treatment, reduce treatment time, and increase cost-competitiveness and -effectiveness?

2) Can cost-competitiveness or treatment capability be increased significantly through incremental improvements to existing accelerator technologies, *e.g.*, fixed-field alternating gradient synchrotron (Johnstone *et al*, 1999) and superconducting cyclotron accelerators (Blosser *et al*, 1997), or novel linear accelerators, *e.g.*, wakefield laser accelerators (Schwoerer *et al*, 2006) and dielectric wall accelerators (Caporaso *et al*, 2008)?

3) Can ultra-compact low-energy proton accelerators provide hand-held or robotically mounted radiation sources for treating superficial tumors or intra-operative treatment of deep-seated tumors?

4) How can range uncertainties be quantified and minimized? In cases where uncertainties are presently too large, what roles will prospective imaging play, including proton CT (Schulte *et al*, 2004) and megavoltage photon CT (Langen *et al*, 2005; Newhauser *et al*, 2008a; De Marzi*et al*, 2013)? Similarly, what role will real-time or post-treatment imaging play, including prompt gamma imaging (Peterson *et al*, 2010; Gueth *et al*, 2013), positron emission tomography (Parodi *et al*, 2007; Cho *et al*, 2013; Min *et al*, 2013), proton radiography (Schneider and Pedroni, 1995), and magnetic resonance imaging (Krejcarek *et al*, 2007)?

5) In the future, what out-of-field dose algorithms should be developed for treatment planning systems used for research or routine clinical practice? Techniques for the calculation and measurement of therapeutic dose are reasonably well established (with a few exceptions mentioned below). In most cases, intensity-modulation techniques have enabled the clinician to provide essentially identical dose distributions to the target volumes using either proton

or photon therapy. Consequently, it appears that comparative treatment planning studies of the future will mainly focus on the radiation exposure of healthy tissues and on the feasibility of delivering novel treatments. Knowledge of the physics of stray radiation exposures is incomplete, and most commercial treatment planning systems neglect or very crudely approximate the out-of-field dose.

6) What are the optimal strategies for treating moving tumors, especially in the thorax and abdomen? For example, will scanned beam treatments with target tracking be beneficial? How should organ motion be measured during treatment? Do the benefits of incremental margin shrinkage justify increased risk of interplay dose defects? Are there cases where passively scattered beams are superior?

7) As the use of on-board imaging is expected to increase, how will additional radiation exposures to patients be monitored and minimized? Are the radiogenic risks of future imaging schemes justified by their benefit to the patient?

8) What is the role of future multimodality radiation therapies that include protons? The objectives of such protocols include reducing skin dose, sharpening penumbral widths and distal falloff lengths, and reducing dose delivery errors. Important sources of errors include temporal interplay of the organ motion and beam location and range uncertainties due to image artifacts caused by metal implants. Possible implementations could include a source of protons and other particles, *e.g*., photons, on a single rotational gantry.

9) Is there a need for a national or international primary standards laboratory to provide reference proton beams to support a standard for dose absorbed to water?

In the preceding 15 years or so, much progress has been made toward a complete understanding of the physics of proton therapy. In particular, today there exist analytical models and simulation techniques to design and model most of the major aspects of clinical proton therapy systems currently in operation, several of which we have reviewed in this paper. However, even with today's state of the art knowledge of proton therapy, the answers to many questions of scientific interest and economic importance remain tantalizingly beyond the reach of current research capabilities. As in the past, clinical needs and economic forces will likely define many of the future research frontiers in proton therapy.

To fully exploit the advantages of proton beams to improve patient outcomes, it is clear that additional research is need to optimize the current generation of proton therapy systems, to make new discoveries and translate breakthroughs into novel prototype research systems, to obtain a deeper and clinically applicable understanding of the relevant aspects of radiation biology, to improve the efficiency clinical operations (*e.g.*, industrial and process engineering), and to generate theoretical and observational evidence to assess the comparative effectiveness and cost of proton therapy relative to other comparable treatments for a wide variety of diseases, anatomical sites, and outcome endpoints. The relative priority

of these goals is a matter of subjective judgment and speculation, which we shall leave to the reader.

Much of the important research will require experts and specialists from disciplines such as accelerator physics, imaging physics, various engineering specialties, oncology, biology, biostatistics and epidemiology, and computer science. Many basic and applied research studies are well suited to purely academic or clinical research environments and research teams. Other research studies will benefit from the formation of collaborative teams comprising members drawn from the academy, medicine, and industry.

Acknowledgements

This work was supported in part by the National Cancer Institute (award 1R01 CA131463-01A1), Department of Defense (award W81XWH-10-1-0170), and the Bella Bowman Foundation.

References

AAPM. American Association of Physicists in Medicine Task Group 20: Protocol for heavy charged-particle therapy beam dosimetry. New York, NY: 1986.

Agosteo S. Radiation protection constraints for use of proton and ion accelerators in medicine. Radiation Protection Dosimetry. 2009; 137:167–86. [PubMed: 19770208]

Agosteo S, Birattari C, Caravaggio M, Silari M, Tosi G. Secondary neutron and photon dose in proton therapy. Radiother Oncol. 1998; 48:293–305. [PubMed: 9925249]

Agostinelli S, Allison J, Amako K, Apostolakis J. Geant4 - A simulation toolkit. Nuclear Instruments and Methods A. 2003; 506:250–303.

Andreo P. On the clinical spatial resolution achievable with protons and heavier charged particle radiotherapy beams. Phys Med Biol. 2009; 54:N205–15. [PubMed: 19436099]

Armstrong GT, Liu Q, Yasui Y, et al. Late mortality among 5-year survivors of childhood cancer: a summary from the Childhood Cancer Survivor Study. J Clin Oncol. 2009; 27:2328–38. [PubMed: 19332714]

Athar BS, Bednarz B, Seco J, Hancox C, Paganetti H. Comparison of out-of-field photon doses in 6 MV IMRT and neutron doses in proton therapy for adult and pediatric patients. Phys Med Biol. 2010; 55:2879–91. [PubMed: 20427856]

Bednarz B, Daartz J, Paganetti H. Dosimetric accuracy of planning and delivering small proton therapy fields. Phys Med Biol. 2010; 55:7425–38. [PubMed: 21098920]

Besemer A, Paganetti H, Bednarz B. The clinical impact of uncertainties in the mean excitation energy of human tissues during proton therapy. Phys Med Biol. 2013; 58:887–902. [PubMed: 23337713]

Bethe H. Zur theorie des durchgangs schneller korpuskularstrahlen durch materie. Ann. Phys. 1930; 5:324–400.

Bloch F. Zur bremsung rasch bewegter teilchen beim durchgang durch materie. Ann. Phys. 1933; 16:285–320.

Blosser, H.; Johnson, D.; Lawton, D., et al. Particle Accelerator Conference Proceedings. Vancouver, BC: 1997. A compact superconducting cyclotron for the production of high intensity protons.; p. 1054-6.

Bohr N. On the decrease of velocity of swiftly moving electrified particles in passing through matter. Philosophical Magazine. 1915; 30:581–612.

Bonnett DE. Current developments in proton therapy: a review. Phys Med Biol. 1993; 38:1371–92. [PubMed: 8248286]

Boon, S. Ph.D. thesis. Rijksuniversiteit Groningen; Ponsen & Looijen BV: 1998. Dosimetry and quality control of scanning proton beams..

Bortfeld T. An analytical approximation of the Bragg curve for therapeutic proton beams. Med Phys. 1997; 24:2024–33. [PubMed: 9434986]

Bortfeld T, Schlegel W. An analytical approximation of depth-dose distributions for therapeutic proton beams. Phys Med Biol. 1996; 41:1331–9. [PubMed: 8858723]

Bragg W, Kleeman R. On the alpha particles of radium and their loss of range in passing through various atoms and molecules. Phil. Mag. 1905; 10:318–40.

Brahme A. Recent advances in light ion radiation therapy. Int J Radiat Oncol Biol Phys. 2004; 58:603–16. [PubMed: 14751534]

Brenner DJ, Elliston CD, Hall EJ, Paganetti H. Reduction of the secondary neutron dose in passively scattered proton radiotherapy, using an optimized pre-collimator/collimator. Phys Med Biol. 2009; 54:6065–78. [PubMed: 19779218]

Brenner DJ, Hall EJ. Secondary neutrons in clinical proton radiotherapy: a charged issue. Radiother Oncol. 2008; 86:165–70. [PubMed: 18192046]

Breuer, H.; Smit, BJ. Proton Therapy and Radiosurgery. Springer; Berlin: 2000.

Caporaso GJ, Mackie TR, Sampayan S, et al. A compact linac for intensity modulated proton therapy based on a dielectric wall accelerator. Phys Med. 2008; 24:98–101. [PubMed: 18430600]

Carnicer A, Angellier G, Thariat J, et al. Quantification of dose perturbations induced by external and internal accessories in ocular proton therapy and evaluation of their dosimetric impact. Med Phys. 2013; 40:061708. [PubMed: 23718587]

Carver JR, Shapiro CL, Ng A, et al. American Society of Clinical Oncology clinical evidence review on the ongoing care of adult cancer survivors: cardiac and pulmonary late effects. J Clin Oncol. 2007; 25:3991–4008. [PubMed: 17577017]

Cheung J, Kudchadker RJ, Zhu XR, Lee AK, Newhauser WD. Dose perturbations and image artifacts caused by carbon-coated ceramic and stainless steel fiducials used in proton therapy for prostate cancer. Phys Med Biol. 2010; 55:7135–47. [PubMed: 21076190]

Cho J, Ibbott G, Gillin M, et al. Determination of elemental tissue composition following proton treatment using positron emission tomography. Phys Med Biol. 2013; 58:3815–35. [PubMed: 23681070]

Chu WT, Ludewigt BA, Renner TR. Instrumentation for treatment of cancer using proton and light-ion beams. Review of Scientific Instruments. 1993; 64:2055–122.

Ciangaru G, Polf JC, Bues M, Smith AR. Benchmarking analytical calculations of proton doses in heterogeneous matter. Med Phys. 2005; 32:3511–23. [PubMed: 16475750]

Coutrakon GB. Accelerators for heavy-charged-particle radiation therapy. Technol Cancer Res Treat. 2007; 6:49–54. [PubMed: 17668952]

De Marzi L, Lesven C, Ferrand R, et al. Calibration of CT Hounsfield units for proton therapy treatment planning: use of kilovoltage and megavoltage images and comparison of parameterized methods. Phys Med Biol. 2013; 58:4255–76. [PubMed: 23719506]

de Moor JS, Mariotto AB, Parry C, et al. Cancer survivors in the United States: prevalence across the survivorship trajectory and implications for care. Cancer Epidemiol Biomarkers Prev. 2013; 22:561–70. [PubMed: 23535024]

DeLaney, T.; Kooy, H. Proton and charged particle radiotherapy. LWW; Philadelphia, PA: 2008.

Desjardins L, Lumbroso L, Levy C, et al. [Treatment of uveal melanoma with iodine 125 plaques or proton beam therapy: indications and comparison of local recurrence rates]. Journal francais d'ophtalmologie. 2003; 26:269–76.

Dowdell SJ, Clasie B, Depauw N, et al. Monte Carlo study of the potential reduction in out-of-field dose using a patient-specific aperture in pencil beam scanning proton therapy. Phys Med Biol. 2012; 57:2829–42. [PubMed: 22513726]

Duttenhaver JR, Shipley WU, Perrone T, et al. Protons or megavoltage X-rays as boost therapy for patients irradiated for localized prostatic carcinoma. An early phase I/II comparison. Cancer. 1983; 51:1599–604. [PubMed: 6299503]

Ferrari, A.; Fasso, A.; Ranft, J.; Sala, P. FLUKA: a multi-particle transport code. CERN; 2005. SLAC-R-773

Fontenot J, Newhauser W, Titt U. Design tools for proton therapy nozzles based on the double-scattering technique. Radiat. Prot. Dosim. 2005a; 116:211–5.

Fontenot J, Taddei P, Zheng Y, et al. Equivalent dose and effective dose from stray radiation during passively scattered proton radiotherapy for prostate cancer. Phys Med Biol. 2008; 53:1677–88. [PubMed: 18367796]

Fontenot JD, Newhauser WD, Bloch C, et al. Determination of output factors for small proton therapy fields. Med Phys. 2007; 34:489–98. [PubMed: 17388166]

Fontenot JD, Newhauser WD, Titt U. Design tools for proton therapy nozzles based on the double-scattering foil technique. Radiat Prot Dosimetry. 2005b; 116:211–5. [PubMed: 16604629]

Gall KP, Verhey LJ, Wagner M. Computer-assisted positioning of radiotherapy patients using implanted radiopaque fiducials. Med Phys. 1993; 20:1153–9. [PubMed: 8413025]

Gensheimer MF, Yock TI, Liebsch NJ, et al. In vivo proton beam range verification using spine MRI changes. Int J Radiat Oncol Biol Phys. 2010; 78:268–75. [PubMed: 20472369]

Giebeler A, Fontenot J, Balter P, et al. Dose perturbations from implanted helical gold markers in proton therapy of prostate cancer. J Appl Clin Med Phys. 2009; 10:63–70.

Goitein M, Jermann M. The relative costs of proton and X-ray radiation therapy. Clin Oncol (R Coll Radiol). 2003; 15:S37–50. [PubMed: 12602563]

Gottschalk, B. Physical parameters of small proton beams.. Handout on PTCOG 31st Conference; Bloomington, IN, USA. 1999.

Gottschalk, B. Passive beam spreading in proton radiation therapy. 2004. unpublished book available at http://huhepl.harvard.edu/~gottschalk

Gottschalk B. Comments on 'Calculation of water equivalent thickness of materials of arbitrary density, elemental composition and thickness in proton beam irradiation'. Phys Med Biol. 2010a; 55:L29–30. author reply L1-2. [PubMed: 20371910]

Gottschalk B. On the scattering power of radiotherapy protons. Med Phys. 2010b; 37:352–67. [PubMed: 20175498]

Gottschalk B, Koehler A, Schneider R, Sisterson J, Wagner M. Multiple Coulomb scattering of 160 MeV protons. Nucl. Instr. Methods. 1993; B74:467–90.

Gragoudas ES, Goitein M, Verhey L, et al. Proton beam irradiation of uveal melanomas. Results of 5 1/2-year study. Archives of ophthalmology. 1982; 100:928–34. [PubMed: 6284097]

Gueth P, Dauvergne D, Freud N, et al. Machine learning-based patient specific prompt-gamma dose monitoring in proton therapy. Phys Med Biol. 2013; 58:4563–77. [PubMed: 23771015]

Hall EJ. Intensity-modulated radiation therapy, protons, and the risk of second cancers. Int J Radiat Oncol Biol Phys. 2006; 65:1–7. [PubMed: 16618572]

Halperin, EC.; Perez, CA.; Brady, LW. Perez and Brady's Principles and Practice of Radiation Oncology. 5th Edition. LWW; Philadelphia, PA: 2008.

Herault J, Iborra N, Serrano B, Chauvel P. Monte Carlo simulation of a protontherapy platform devoted to ocular melanoma. Med Phys. 2005; 32:910–9. [PubMed: 15895573]

Hogstrom KR, Mills MD, Almond PR. Electron beam dose calculations. Phys Med Biol. 1981; 26:445–59. [PubMed: 6787621]

Hong L, Goitein M, Bucciolini M, et al. A pencil beam algorithm for proton dose calculations. Phys Med Biol. 1996; 41:1305–30. [PubMed: 8858722]

Huang JY, Newhauser WD, Zhu XR, Lee AK, Kudchadker RJ. Investigation of dose perturbations and the radiographic visibility of potential fiducials for proton radiation therapy of the prostate. Phys Med Biol. 2011; 56:5287–302. [PubMed: 21799236]

IAEA. Radiological Safety Aspects of the Operation of Proton Accelerators. Vienna, Austria: 1988.

IAEA. International Atomic Energy Agency Technical Report Series No. 398: Absorbed Dose Determination in External Beam Radiotherapy. Vienna, VA: 2000.

ICRP. Ann ICRP. 2007. The 2007 Recommendations of the International Commission on Radiological Protection. ICRP publication 103.; p. 1-332.

ICRU. Stopping Powers and Ranges for Protons and Alpha Particles ICRU Report 49. Bethesda, MD: 1993.

ICRU. Secondary Electron Spectra from Charged Particle Interactions ICRU Report 55. Oxford University Press; Oxford: 1995.

ICRU. Clinical proton dosimetry part I: Beam production, beam delivery, and measurement of absorbed dose ICRU Report 59. Bethesda, MD: 1998.

ICRU. Nuclear Data for Neutron and Proton Radiotherapy and for Radiation Protection ICRU Report 63. Bethesda, Maryland: 2000.

ICRU. Prescribing, Recording, and Reporting Proton-Beam Therapy ICRU Report 78. Oxford University Press; Oxford: 2007.

Jia X, Schumann J, Paganetti H, Jiang SB. GPU-based fast Monte Carlo dose calculation for proton therapy. Phys Med Biol. 2012; 57:7783–97. [PubMed: 23128424]

Jiang H, Wang B, Xu XG, Suit HD, Paganetti H. Simulation of organ-specific patient effective dose due to secondary neutrons in proton radiation treatment. Phys Med Biol. 2005; 50:4337–53. [PubMed: 16148397]

Johnstone, C.; Wan, W.; Garren, A. Particle Accelerator Conference. New York, USA: 1999. Fixed field circular accelerator designs.; p. 3068-70.

Kim JS, An SJ, Chung YH. New concept of a range verification system for proton therapy using a photon counting detector. Nucl Instrum Meth A. 2012; 677:18–21.

Kimstrand P, Tilly N, Ahnesjo A, Traneus E. Experimental test of Monte Carlo proton transport at grazing incidence in GEANT4, FLUKA and MCNPX. Phys Med Biol. 2008; 53:1115–29. [PubMed: 18263962]

Kjellberg RN, Koehler AM, Preston WM, Sweet WH. Stereotaxic instrument for use with the Bragg peak of a proton beam. Confinia neurologica. 1962a; 22:183–9. [PubMed: 14033248]

Kjellberg RN, Sweet WH, Preston WM, Koehler AM. The Bragg peak of a proton beam in intracranial therapy of tumors. Transactions of the American Neurological Association. 1962b; 87:216–8. [PubMed: 14033249]

Koch N, Newhauser W. Virtual commissioning of a treatment planning system for proton therapy of ocular cancers. Radiat Prot Dosimetry. 2005; 115:159–63. [PubMed: 16381705]

Koch NC, Newhauser WD. Development and verification of an analytical algorithm to predict absorbed dose distributions in ocular proton therapy using Monte Carlo simulations. Phys Med Biol. 2010; 55:833–53. [PubMed: 20071765]

Koehler AM, Preston WM. Protons in radiation therapy. Comparative dose distributions for protons, photons, and electrons. Radiology. 1972; 104:191–5. [PubMed: 4624458]

Koehler AM, Schneider RJ, Sisterson JM. Flattening of proton dose distributions for large-field radiotherapy. Med Phys. 1977; 4:297–301. [PubMed: 407436]

Kraft G, Scholz M, Bechthold U. Tumor therapy and track structure. Radiation and environmental biophysics. 1999; 38:229–37. [PubMed: 10654344]

Krejcarek SC, Grant PE, Henson JW, Tarbell NJ, Yock TI. Physiologic and radiographic evidence of the distal edge of the proton beam in craniospinal irradiation. Int J Radiat Oncol Biol Phys. 2007; 68:646–9. [PubMed: 17449195]

Landau L. On the energy loss of fast particles by ionization. J. Phys. (USSR). 1944; 8:201–5.

Langen KM, Meeks SL, Poole DO, et al. The use of megavoltage CT (MVCT) images for dose recomputations. Phys Med Biol. 2005; 50:4259–76. [PubMed: 16148392]

Larsson, B. The new radiations in cancer therapy.. In: Amaldi, U.; Larsson, B., editors. Hadrontherapy in Oncology:Proceedings of the First International Symposium on Hadrontherapy, October 18-21, 1993. Elsevier Science B.V., Amsterdam; Como, Italy: 1993.

Lawrence JH, Tobias CA, Born JL, et al. Pituitary irradiation with high-energy proton beams: a preliminary report. Cancer research. 1958; 18:121–34. [PubMed: 13511365]

Lee, SY. Accelerator Physics. 2nd edition. World Scientific Publishing Co.; Singapore: 2004.

Leo, WR. Techniques for Nuclear and Particle Physics Experiments - A How-to Approach. Springer-Verlag; Berlin: 1994.

Li HS, Romeijn HE, Fox C, Palta JR, Dempsey JF. A computational implementation and comparison of several intensity modulated proton therapy treatment planning algorithms. Med Phys. 2008; 35:1103–12. [PubMed: 18404945]

Lievens Y, Pijls-Johannesma M. Health economic controversy and cost-effectiveness of proton therapy. Semin Radiat Oncol. 2013; 23:134–41. [PubMed: 23473691]

Lim YK, Kwak J, Kim DW, et al. Microscopic gold particle-based fiducial markers for proton therapy of prostate cancer. Int J Radiat Oncol Biol Phys. 2009; 74:1609–16. [PubMed: 19616746]

Linz, U. Ion Beams Therapy: Fundamentals, Technology, Clinical Applications. Springer; Heidelberg: 2012.

Lomax AJ. Charged particle therapy: the physics of interaction. Cancer J. 2009; 15:285–91. [PubMed: 19672144]

Ma, CM.; Lomax, T. Proton and Carbon Ion Therapy. CRC Press; Boca Baton, FL: 2013.

Mairani A, Bohlen TT, Schiavi A, et al. A Monte Carlo-based treatment planning tool for proton therapy. Phys Med Biol. 2013; 58:2471–90. [PubMed: 23514837]

Matsuura T, Maeda K, Sutherland K, et al. Biological effect of dose distortion by fiducial markers in spot-scanning proton therapy with a limited number of fields: a simulation study. Med Phys. 2012; 39:5584–91. [PubMed: 22957624]

Medin J, Andreo P. Monte Carlo calculated stopping-power ratios, water/air, for clinical proton dosimetry (50-250 MeV). Phys Med Biol. 1997; 42:89–105. [PubMed: 9015811]

Merchant TE. Proton beam therapy in pediatric oncology. Cancer J. 2009; 15:298–305. [PubMed: 19672146]

Mesoloras G, Sandison GA, Stewart RD, Farr JB, Hsi WC. Neutron scattered dose equivalent to a fetus from proton radiotherapy of the mother. Med Phys. 2006; 33:2479–90. [PubMed: 16898451]

Min CH, Lee HR, Kim CH, Lee SB. Development of array-type prompt gamma measurement system for in vivo range verification in proton therapy. Med Phys. 2012; 39:2100–7. [PubMed: 22482631]

Min CH, Zhu X, Winey BA, et al. Clinical application of in-room positron emission tomography for in vivo treatment monitoring in proton radiation therapy. Int J Radiat Oncol Biol Phys. 2013; 86:183–9. [PubMed: 23391817]

Molière G. Theorie der streuung schneller geladener teilchen II, mehrfach-und vielfachstreuung Z. Naturforsch. A. 1948; 3A:78–97.

Moritz LE. Radiation protection at low energy proton accelerators. Radiat Prot Dosimetry. 2001; 96:297–309. [PubMed: 11843080]

Moteabbed M, Espana S, Paganetti H. Monte Carlo patient study on the comparison of prompt gamma and PET imaging for range verification in proton therapy. Phys Med Biol. 2011; 56:1063–82. [PubMed: 21263174]

Moyer, BJ. Proceedings of the First International Conference on Shielding Around High Energy Accelerators. Press Universitaires de France, Paris; Saclay, France: 1962. Method of calculation of the shielding enclosure for the Berkeley Bevatron.; p. 65-70.

Moyers MF, Benton ER, Ghebremedhin A, Coutrakon G. Leakage and scatter radiation from a double scattering based proton beamline. Med Phys. 2008; 35:128–44. [PubMed: 18293570]

Moyers MF, Galindo RA, Yonemoto LT, et al. Treatment of macular degeneration with proton beams. Med Phys. 1999; 26:777–82. [PubMed: 10360542]

NCRP. NCRP Report 38. National Council on Radiation Protection and Measurements; Bethesda, MD: 1971. Protection against neutron radiation..

NCRP. NCRP Report 107. Bethesda, MD: 1990. Implementation of the principle of As Low As Reasonably Achievable (ALARA) for medical and dental personnel..

NCRP. NCRP Report 116. Bethesda, MD: 1993. Limitation of exposure to ionizing radiation (supersedes NCRP Report No. 91)..

NCRP. NCRP Report 144. Bethesda, MD: 2005. Radiation protection for particle accelerator facilities..

NCRP. Report No.151: Structural Shielding Design and Evaluation for Megavoltage X- and Gamma-Ray Radiotherapy Facilities. Bethesda, MD: 2008.

NCRP. Report No. 170: Second primary cancers and cardiovascular disease after radiation therapy. Bethesda, MD: 2011.

Newhauser W, Burns J, Smith A. Dosimetry for ocular proton beam therapy at the Harvard Cyclotron Laboratory based on the ICRU Report 59. Med Phys. 2002a; 29:1953–61. [PubMed: 12349914]

Newhauser W, Fontenot J, Koch N, et al. Monte Carlo simulations of the dosimetric impact of radiopaque fiducial markers for proton radiotherapy of the prostate. Phys Med Biol. 2007a; 52:2937–52. [PubMed: 17505081]

Newhauser W, Fontenot J, Zheng Y, et al. Monte Carlo simulations for configuring and testing an analytical proton dose-calculation algorithm. Phys Med Biol. 2007b; 52:4569–84. [PubMed: 17634651]

Newhauser W, Koch N, Hummel S, Ziegler M, Titt U. Monte Carlo simulations of a nozzle for the treatment of ocular tumours with high-energy proton beams. Phys Med Biol. 2005; 50:5229–49. [PubMed: 16264250]

Newhauser W, Myers K, Rosenthal S, Smith A. Proton Beam Dosimetry for Radiosurgery: Implementation of the ICRU Report 59 at the Harvard Cyclotron Laboratory. Phys. Med. Biol. 2002b; 47:1369–89. [PubMed: 12030561]

Newhauser WD. Dosimetry for the Gantry Beams at the Northeast Proton Therapy Center (NPTC) Part I: Dimensions and Geometric Relationships. NPTC Internal Report. 2001a

Newhauser WD. Proton Field Calibration Measurements and Analysis with the CalibrationSetUp Program (CSU) Version 1.1. Internal Report. 2001b

Newhauser WD, Durante M. Assessing the risk of second malignancies after modern radiotherapy. Nat Rev Cancer. 2011; 11:438–48. [PubMed: 21593785]

Newhauser WD, Fontenot JD, Mahajan A, et al. The risk of developing a second cancer after receiving craniospinal proton irradiation. Phys Med Biol. 2009; 54:2277–91. [PubMed: 19305036]

Newhauser, WD.; Giebeler, A.; Guo, B.; Zhang, R. Uncertainty in dose permonitor unit estimates for passively scattered proton therapy, part II: The role of compensator and patient scatter. 2014a. in thoracic cases in preparation

Newhauser WD, Giebeler A, Langen KM, Mirkovic D, Mohan R. Can megavoltage computed tomography reduce proton range uncertainties in treatment plans for patients with large metal implants? Phys Med Biol. 2008a; 53:2327–44. [PubMed: 18421122]

Newhauser, WD.; Giebeler, A.; Zhu, R., et al. Uncertainty in dose per monitor unit estimates for passively scattered proton therapy, part I: The role of compensator and patient scatter in prostate cases. 2014b. in preparation

Newhauser WD, Koch NC, Fontenot JD, et al. Dosimetric impact of tantalum markers used in the treatment of uveal melanoma with proton beam therapy. Phys Med Biol. 2007c; 52:3979–90. [PubMed: 17664589]

Newhauser WD, Rechner LA, Mirkovic D, et al. Benchmark measurements and simulations of dose perturbations due to metallic spheres in proton beams. Radiation Measurements. 2013; 58:37–44. [PubMed: 25147474]

Newhauser WD, Titt U, Dexheimer D, Yan X, Nill S. Neutron shielding verification measurements and simulations for a 235-MeV proton therapy center. Nucl Instrum Meth A. 2002c; 476:80–4.

Newhauser, WD.; Titt, U.; Dexheimer, DT. Shielding Aspects of Accelerators, Targets and Irradiation Facilities-SATIF 6. Nuclear Energy Agency; Stanford, CA: 2002d. A perspective on shielding design methods for future proton therapy facilities..

Newhauser WD, Zhang R. In reply to Dr. Gottschalk's comment on “Calculation of water equivalent thickness of materials of arbitary density, elemental composition and thickness in proton beam irradiation”. Physics in medicine and biology. 2010; 55:L31–2.

Newhauser WD, Zheng Y, Taddei PJ, et al. Monte Carlo proton radiation therapy planning calculations. Trans. Am. Nucl. Soc. 2008b; 99:63–4.

Olch, AJ. Pediatric Radiotherapy - Planning and Treatment. CRC Press; Boca Raton, FL: 2013.

Paganetti H. Nuclear interactions in proton therapy: dose and relative biological effect distributions originating from primary and secondary particles. Phys Med Biol. 2002; 47:747–64. [PubMed: 11931469]

Paganetti, H. Proton therapy physics. CRC Press; Boca Raton, FL: 2012.

Paganetti H, Jiang H, Trofimov A. 4D Monte Carlo simulation of proton beam scanning: modelling of variations in time and space to study the interplay between scanning pattern and time-dependent patient geometry. Phys Med Biol. 2005; 50:983–90. [PubMed: 15798270]

Parodi K, Paganetti H, Cascio E, et al. PET/CT imaging for treatment verification after proton therapy: a study with plastic phantoms and metallic implants. Med Phys. 2007; 34:419–35. [PubMed: 17388158]

Pawlicki, T.; Dunscombe, PB.; Mundt, AJ.; Scalliet, P. Quality and Safety in Radiotherapy. CRC Press; Boca Raton, FL: 2011.

Pedroni E, Bacher R, Blattmann H, et al. The 200-MeV proton therapy project at the Paul Scherrer Institute: conceptual design and practical realization. Med Phys. 1995; 22:37–53. [PubMed: 7715569]

Pedroni E, Scheib S, Bohringer T, et al. Experimental characterization and physical modelling of the dose distribution of scanned proton pencil beams. Phys Med Biol. 2005; 50:541–61. [PubMed: 15773729]

Peeters A, Grutters JP, Pijls-Johannesma M, et al. How costly is particle therapy? Cost analysis of external beam radiotherapy with carbon-ions, protons and photons. Radiother Oncol. 2010; 95:45–53. [PubMed: 20106540]

Pelowitz. MCNPX User's Manual, Version 2.7.0. Los Alamos National Laboratory; 2011.

Perez-Andujar A, Newhauser WD, Deluca PM. Neutron production from beam-modifying devices in a modern double scattering proton therapy beam delivery system. Phys Med Biol. 2009; 54:993–1008. [PubMed: 19147903]

Perez-Andujar A, Newhauser WD, Taddei PJ, Mahajan A, Howell RM. The predicted relative risk of premature ovarian failure for three radiotherapy modalities in a girl receiving craniospinal irradiation. Phys Med Biol. 2013a; 58:3107–23. [PubMed: 23603657]

Perez-Andujar A, Zhang R, Newhauser W. Monte Carlo and analytical model predictions of leakage neutron exposures from passively scattered proton therapy. Med Phys. 2013b; 40:121714. [PubMed: 24320500]

Perl J, Shin J, Schumann J, Faddegon B, Paganetti H. TOPAS: an innovative proton Monte Carlo platform for research and clinical applications. Med Phys. 2012; 39:6818–37. [PubMed: 23127075]

Peterson SW, Polf J, Bues M, et al. Experimental validation of a Monte Carlo proton therapy nozzle model incorporating magnetically steered protons. Phys Med Biol. 2009; 54:3217–29. [PubMed: 19420426]

Peterson SW, Robertson D, Polf J. Optimizing a three-stage Compton camera for measuring prompt gamma rays emitted during proton radiotherapy. Phys Med Biol. 2010; 55:6841–56. [PubMed: 21048295]

Petti PL. Differential-pencil-beam dose calculations for charged particles. Med Phys. 1992; 19:137–49. [PubMed: 1320182]

Polf JCHM, Titt U, Newhauser WD, Smith AR. Initial beam size study for passive scatter proton therapy – Part I: Monte Carlo Verification. Med Phys. 2007; 34:4213–8. [PubMed: 18072485]

Polf JC, Newhauser WD. Calculations of neutron dose equivalent exposures from range-modulated proton therapy beams. Phys Med Biol. 2005; 50:3859–73. [PubMed: 16077232]

Polf JC, Newhauser WD, Titt U. Patient neutron dose equivalent exposures outside of the proton therapy treatment field. Radiat Prot Dosimetry. 2005; 115:154–8. [PubMed: 16381704]

Preston, WM.; Koehler, AM. Proton beam dosimery, Harvard Cycloron Laboratory. 1998. unpublished manuscript. Obtained by personal communication

Ptaszkiewicz M, Weber A, Swakon J, et al. Dose perturbation behind tantalum clips in ocular proton therapy. Radiat. Meas. 2010; 45:694–7.

PTCOG. PTCOG patient statistics of particle therapy centers per end of 2012. 2013.

Raaymakers BW, Raaijmakers AJ, Lagendijk JJ. Feasibility of MRI guided proton therapy: magnetic field dose effects. Phys Med Biol. 2008; 53:5615–22. [PubMed: 18799829]

Randeniya SD, Taddei PJ, Newhauser WD, Yepes P. Intercomparision of Monte Carlo Radiation Transport Codes MCNPX, GEANT4, and FLUKA for Simulating Proton Radiotherapy of the Eye. Nucl Technol. 2009; 168:810–4. [PubMed: 20865141]

Rechner LA, Howell RM, Zhang R, et al. Risk of radiogenic second cancers following volumetric modulated arc therapy and proton arc therapy for prostate cancer. Phys Med Biol. 2012; 57:7117–32. [PubMed: 23051714]

Rethfeldt C, Fuchs H, Gardey KU. Dose distributions of a proton beam for eye tumor therapy: hybrid pencil-beam ray-tracing calculations. Med Phys. 2006; 33:782–91. [PubMed: 16878580]

Rossi, HH.; Zaider, M. Microdosimetry and Its Applications. Springer; Berlin: 1996.

Roy SC, Sandison GA. Scattered neutron dose equivalent to a fetus from proton therapy of the mother. Radiat. Phys. Chem. 2004; 71:997–8.

Rutherford E. The scattering of α and β particles by matter and the structure of the atom. Philosophical Magazine. 1911; 21:669–88.

Sandison GA, Papiez E, Bloch C, Morphis J. Phantom assessment of lung dose from proton arc therapy. Int J Radiat Oncol Biol Phys. 1997; 38:891–7. [PubMed: 9240659]

Sauvat F, Binart N, Poirot C, Sarnacki S. Preserving fertility in prepubertal children. Hormone research. 2009; 71(Suppl 1):82–6. [PubMed: 19153513]

Sawakuchi GO, Mirkovic D, Perles LA, et al. An MCNPX Monte Carlo model of a discrete spot scanning proton beam therapy nozzle. Med Phys. 2010; 37:4960–70. [PubMed: 20964215]

Schaffner B. Proton dose calculation based on in-air fluence measurements. Phys Med Biol. 2008; 53:1545–62. [PubMed: 18367787]

Schaffner B, Pedroni E, Lomax A. Dose calculation models for proton treatment planning using a dynamic beam delivery system: an attempt to include density heterogeneity effects in the analytical dose calculation. Phys Med Biol. 1999; 44:27–41. [PubMed: 10071873]

Schardt D, Elsasser T. Heavy-ion tumor therapy: physical and radiobiological benefits. Reviews of Modern Physics. 2010; 82:383–425.

Scharf, WH. Biomedical Particle Accelerators. AIP Press; Woodbury, NY: 1994.

Schneider U, Agosteo S, Pedroni E, Besserer J. Secondary neutron dose during proton therapy using spot scanning. Int J Radiat Oncol Biol Phys. 2002; 53:244–51. [PubMed: 12007965]

Schneider U, Pedroni E. Proton radiography as a tool for quality control in proton therapy. Med Phys. 1995; 22:353–63. [PubMed: 7609715]

Schulte R, Bashkirov V, Li T, et al. Conceptual design of a proton computed tomography system for applications in proton radiation therapy. IEEE Transactions on Nuclear Science. 2004; 51:866–72.

Schwoerer H, Pfotenhauer S, Jackel O, et al. Laser-plasma acceleration of quasi-monoenergetic protons from microstructured targets. Nature. 2006; 439:445–8. [PubMed: 16437110]

Seco, J.; Verhaegen, F. Monte Carlo Techniques in Radiation Therapy. CRC Press; Boca Raton, FL: 2013.

Seltzer, SM.; Berger, MJ. Studies in the Penetration of Charged Particles in Matter. National Academy of Sciences; 1964. Energy Loss Straggling and of Protons and Mesons: Tabulations of Vavilov Distribution". Publication 1133, Nuclear Science Series Report No. 39

Sengbusch E, Perez-Andujar A, DeLuca PM Jr. Mackie TR. Maximum proton kinetic energy and patient-generated neutron fluence considerations in proton beam arc delivery radiation therapy. Med Phys. 2009; 36:364–72. [PubMed: 19291975]

Shipley WU, Verhey LJ, Munzenrider JE, et al. Advanced prostate cancer: the results of a randomized comparative trial of high dose irradiation boosting with conformal protons compared with conventional dose irradiation using photons alone. Int J Radiat Oncol Biol Phys. 1995; 32:3–12. [PubMed: 7721636]

Siddon RL. Fast calculation of the exact radiological path for a three-dimensional CT array. Med Phys. 1985; 12:252–5. [PubMed: 4000088]

Siebers, J. Application of Monte Carlo to proton beam radiation therapy.. In: Kling, A., et al., editors. Advanced Monte Carlo for Radiation Physics, Particle Transport Simulation, and Applications. Springer; Lisbon: 2000. p. 1051-6.

Smeets J, Roellinghoff F, Prieels D, et al. Prompt gamma imaging with a slit camera for real-time range control in proton therapy. Phys Med Biol. 2012; 57:3371–405. [PubMed: 22572603]

Soukup M, Fippel M, Alber M. A pencil beam algorithm for intensity modulated proton therapy derived from Monte Carlo simulations. Phys Med Biol. 2005; 50:5089–104. [PubMed: 16237243]

Stankovskiy A, Kerhoas-Cavata S, Ferrand R, Nauraye C, Demarzi L. Monte Carlo modelling of the treatment line of the Proton Therapy Center in Orsay. Phys Med Biol. 2009; 54:2377–94. [PubMed: 19321923]

Szymanowski H, Oelfke U. Two-dimensional pencil beam scaling: an improved proton dose algorithm for heterogeneous media. Phys Med Biol. 2002; 47:3313–30. [PubMed: 12375823]

Szymanowski H, Oelfke U. CT calibration for two-dimensional scaling of proton pencil beams. Phys Med Biol. 2003; 48:861–74. [PubMed: 12701891]

Taddei PJ, Fontenot JD, Zheng Y, et al. Reducing stray radiation dose to patients receiving passively scattered proton radiotherapy for prostate cancer. Phys Med Biol. 2008; 53:2131–47. [PubMed: 18369278]

Taddei PJ, Howell RM, Krishnan S, et al. Risk of second malignant neoplasm following proton versus intensity-modulated photon radiotherapies for hepatocellular carcinoma. Phys Med Biol. 2010a; 55:7055–65. [PubMed: 21076199]

Taddei PJ, Jalbout W, Howell RM, et al. Analytical model for out-of-field dose in photon craniospinal irradiation. Phys Med Biol. 2013; 58:7463–79. [PubMed: 24099782]

Taddei PJ, Mahajan A, Mirkovic D, et al. Predicted risks of second malignant neoplasm incidence and mortality due to secondary neutrons in a girl and boy receiving proton craniospinal irradiation. Phys Med Biol. 2010b; 55:7067–80. [PubMed: 21076189]

Taddei PJ, Mirkovic D, Fontenot JD, et al. Stray radiation dose and second cancer risk for a pediatric patient receiving craniospinal irradiation with proton beams. Phys Med Biol. 2009; 54:2259–75. [PubMed: 19305045]

Takada Y. Study of small proton beam field. Particles. 1996; 18:A35.

Tayama R, Fujita Y, Tadokoro M, et al. Measurement of neutron dose distribution for a passive scattering nozzle at the Proton Medical Research Center (PMRC). Nucl Instrum Meth A. 2006; 564:532–6.

Terasawa T, Dvorak T, Ip S, et al. Systematic review: charged-particle radiation therapy for cancer. Ann Intern Med. 2009; 151:556–65. [PubMed: 19755348]

Tesch K. The attenuation of the neutron dose equivalent in a labyrinth through an accelerator shield. Particle Accelerators. 1982; 12:169–75.

Titt U, Mirkovic D, Sawakuchi GO, et al. Adjustment of the lateral and longitudinal size of scanned proton beam spots using a pre-absorber to optimize penumbrae and delivery efficiency. Phys Med Biol. 2010; 55:7097–106. [PubMed: 21076194]

Titt U, Newhauser WD. Neutron shielding calculations in a proton therapy facility based on Monte Carlo simulations and analytical models: criterion for selecting the method of choice. Radiat. Prot. Dosim. 2005; 115:144–8.

Titt U, Sahoo N, Ding X, et al. Assessment of the accuracy of an MCNPX-based Monte Carlo simulation model for predicting three-dimensional absorbed dose distributions. Phys Med Biol. 2008a; 53:4455–70. [PubMed: 18670050]

Titt U, Zheng Y, Vassiliev ON, Newhauser WD. Monte Carlo investigation of collimator scatter of proton-therapy beams produced using the passive scattering method. Phys Med Biol. 2008b; 53:487–504. [PubMed: 18185001]

Tourovsky A, Lomax AJ, Schneider U, Pedroni E. Monte Carlo dose calculations for spot scanned proton therapy. Phys Med Biol. 2005; 50:971–81. [PubMed: 15798269]

Vadapalli R, Yepes P, Newhauser WD, Lichti R. Grid-enabled treatment planning for proton therapy using Monte Carlo simulations. Nucl Technol. 2011; 175:16–21. [PubMed: 25505349]

Valdivieso M, Kujawa AM, Jones T, Baker LH. Cancer survivors in the United States: a review of the literature and a call to action. International journal of medical sciences. 2012; 9:163–73. [PubMed: 22275855]

Van Dyk, J. The Modern Technology of Radiation Oncology: A Compendium for Medical Physicists and Radiation Oncologists. Medical Physics Publishing; Wisconsin: 1999.

Vatnitsky S, Moyers M, Miller D, et al. Proton dosimetry intercomparison based on the ICRU report 59 protocol. Radiother Oncol. 1999a; 51:273–9. [PubMed: 10435822]

Vatnitsky SM, Miller DW, Moyers MF, et al. Dosimetry techniques for narrow proton beam radiosurgery. Phys Med Biol. 1999b; 44:2789–801. [PubMed: 10588285]

Vavilov PV. Ionization losses of high-energy heavy particles. Soviet Physics JETP. 1957; 5:749–51.

Verhey LJ, Koehler AM, McDonald JC, et al. The determination of absorbed dose in a proton beam for purposes of charged-particle radiation therapy. Radiat Res. 1979; 79:34–54. [PubMed: 472125]

Vynckier S, Bonnett DE, Jones DT. Code of practice for clinical proton dosimetry. Radiother Oncol. 1991; 20:53–63. [PubMed: 2020756]

Vynckier S, Bonnett DE, Jones DT. Supplement to the code of practice for clinical proton dosimetry. ECHED (European Clinical Heavy Particle Dosimetry Group). Radiother Oncol. 1994; 32:174–9. [PubMed: 7972911]

Weber DC, Wang H, Cozzi L, et al. RapidArc, intensity modulated photon and proton techniques for recurrent prostate cancer in previously irradiated patients: a treatment planning comparison study. Radiat Oncol. 2009; 4:34. [PubMed: 19740429]

Welsh JS, Berta C, Borzillary S, et al. Fiducial markers implanted during prostate brachytherapy for guiding conformal external beam radiation therapy. Technol Cancer Res Treat. 2004; 3:359–64. [PubMed: 15270586]

Westerly DC, Mo X, Tome WA, Mackie TR, Deluca PM. A generalized 2D pencil beam scaling algorithm for proton dose calculation in heterogeneous slab geometries. Med Phys. 2013; 40:061706. [PubMed: 23718585]

Wilson, R. A Brief History of The Harvard University Cyclotrons. Harvard University Press; Cambridge, MA: 2004.

Wilson RR. Radiological use of fast protons. Radiology. 1946; 47:487–91. [PubMed: 20274616]

Wilson VC, McDonough J, Tochner Z. Proton beam irradiation in pediatric oncology: an overview. Journal of pediatric hematology/oncology. 2005; 27:444–8. [PubMed: 16096529]

Wroe A, Rosenfeld A, Schulte R. Out-of-field dose equivalents delivered by proton therapy of prostate cancer. Med Phys. 2007; 34:3449–56. [PubMed: 17926946]

Wroe AJ, Cornelius IM, Rosenfeld AB. The role of nonelastic reactions in absorbed dose distributions from therapeutic proton beams in different medium. Med Phys. 2005; 32:37–41. [PubMed: 15719952]

Xu XG, Bednarz B, Paganetti H. A review of dosimetry studies on external-beam radiation treatment with respect to second cancer induction. Phys Med Biol. 2008; 53:R193–241. [PubMed: 18540047]

Yan X, Titt U, Koehler AM, Newhauser WD. Measurement of neutron dose equivalent to proton therapy patients outside of the proton radiation field. Nucl Instrum Meth A. 2002; 476:429–34.

Yepes P, Randeniya S, Taddei PJ, Newhauser WD. Monte Carlo fast dose calculator for proton radiotherapy: application to a voxelized geometry representing a patient with prostate cancer. Phys Med Biol. 2009a; 54:N21–8. [PubMed: 19075361]

Yepes P, Randeniya S, Taddei PJ, Newhauser WD. A Track-Repeating Algorithm for Fast Monte Carlo Dose Calculations of Proton Radiotherapy. Nucl Technol. 2009b; 168:736–40. [PubMed: 20865140]

Yepes PP, Brannan T, Huang J, et al. Application of a fast proton dose calculation algorithm to a thorax geometry. Radiat Meas. 2010a; 45:1367–8. [PubMed: 21544230]

Yepes PP, Mirkovic D, Taddei PJ. A GPU implementation of a track-repeating algorithm for proton radiotherapy dose calculations. Phys Med Biol. 2010b; 55:7107–20. [PubMed: 21076192]

Zacharatou Jarlskog C, Paganetti H. Risk of developing second cancer from neutron dose in proton therapy as function of field characteristics, organ, and patient age. Int J Radiat Oncol Biol Phys. 2008; 72:228–35. [PubMed: 18571337]

Zhang M, Kim SH, Chen T, et al. Dose perturbations of gold fiducial markers in the prostate cancer intensity modulated proton radiation therapy. International Journal of Medical Physics, Clinical Engineering and Radiation Oncology. 2012; 1:8–13.

Zhang R, Fontenot J, Mirkovic D, Hendricks J, Newhauser D. Advantages of MCNPX-based lattice tally over mesh tally in high-speed Monte Carlo dose reconstruction for proton radiotherapy. Nucl Technol. 2013a; 183:101–6. [PubMed: 25435594]

Zhang R, Howell RM, Giebeler A, et al. Comparison of risk of radiogenic second cancer following photon and proton craniospinal irradiation for a pediatric medulloblastoma patient. Phys Med Biol. 2013b; 58:807–23. [PubMed: 23322160]

Zhang R, Howell RM, Homann K, et al. Predicted risks of radiogenic cardiac toxicity in two pediatric patients undergoing photon or proton radiotherapy. Radiat Oncol. 2013c; 8:184. [PubMed: 23880421]

Zhang R, Howell RM, Taddei PJ, et al. A comparative study on the risks of radiogenic second cancers and cardiac mortality in a set of pediatric medulloblastoma patients treated with photon or proton craniospinal irradiation. Radiother Oncol. 2014

Zhang R, Newhauser WD. Calculation of water equivalent thickness of materials of arbitrary density, elemental composition and thickness in proton beam irradiation. Phys Med Biol. 2009; 54:1383–95. [PubMed: 19218739]

Zhang R, Perez-Andujar A, Fontenot JD, Taddei PJ, Newhauser WD. An analytic model of neutron ambient dose equivalent and equivalent dose for proton radiotherapy. Phys Med Biol. 2010a; 55:6975–85. [PubMed: 21076197]

Zhang R, Taddei PJ, Fitzek MM, Newhauser WD. Water equivalent thickness values of materials used in beams of protons, helium, carbon and iron ions. Phys Med Biol. 2010b; 55:2481–93. [PubMed: 20371908]

Zheng Y, Fontenot J, Taddei P, Mirkovic D, Newhauser W. Monte Carlo simulations of neutron spectral fluence, radiation weighting factor and ambient dose equivalent for a passively scattered proton therapy unit. Phys Med Biol. 2008; 53:187–201. [PubMed: 18182696]

Zheng Y, Newhauser W, Fontenot J, Koch N, Mohan R. Monte Carlo simulations of stray neutron radiation exposures in proton therapy. J. Nucl. Matl. 2007a; 361:289–97.

Zheng Y, Newhauser W, Fontenot J, Taddei P, Mohan R. Monte Carlo study of neutron dose equivalent during passive scattering proton therapy. Phys Med Biol. 2007b; 52:4481–96. [PubMed: 17634645]

Ziegler JF. Stopping of energetic light ions in elemental matter. Journal of Applied Physics. 1999; 85:1249–72.

Ziegler, JF.; Biersack, JP.; Littmark, U. The Stopping and Range of Ions in Solids. Pergamon; New York: 1985.

Ziegler, JF.; Biersack, JP.; Ziegler, MD. SRIM - The Stopping and Range of Ions in Matter. SRIM Co.; Chester, MD: 2008.

Zietman AL, Bae K, Slater JD, et al. Randomized trial comparing conventional-dose with high-dose conformal radiation therapy in early-stage adenocarcinoma of the prostate: long-term results from proton radiation oncology group/american college of radiology 95-09. J Clin Oncol. 2010; 28:1106–11. [PubMed: 20124169]

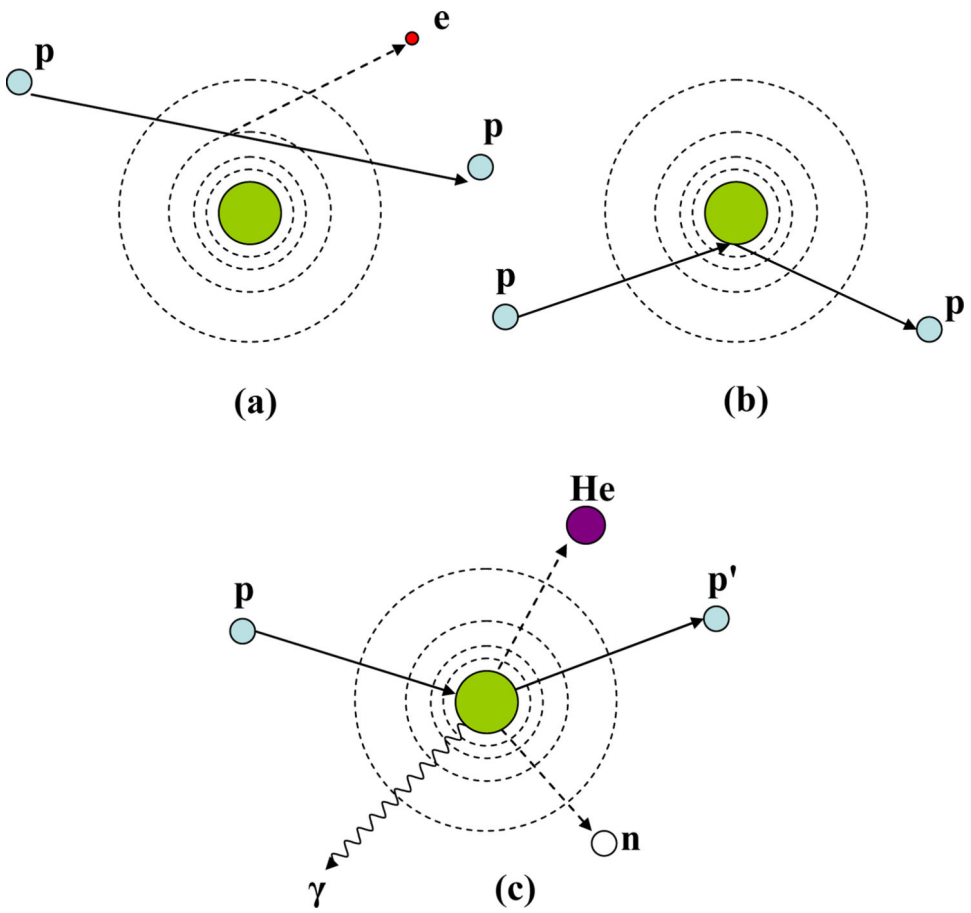

Figure 1.

Schematic illustration of proton interaction mechanisms: (a) energy loss via Coulombic interactions, (b) deflection of proton trajectory by repulsive Coulomb scattering with nucleus, (c) removal of primary proton and creation of secondary particles via non-elastic nuclear interaction. (p: proton, e: electron, n: neutron, He: Helium, γ: gamma rays)

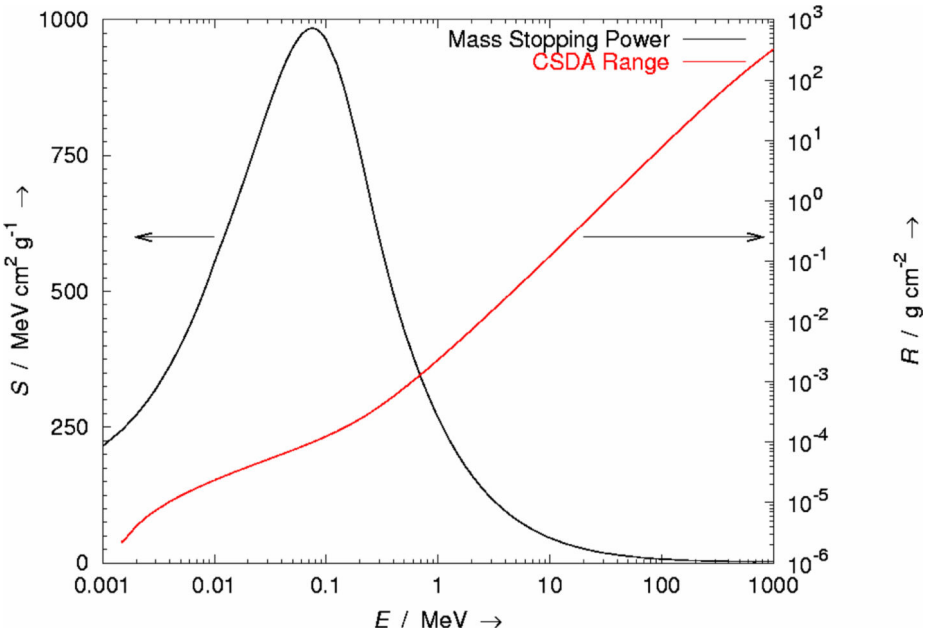

Figure 2.

Mass stopping power (*S*) versus ion energy (*E*) for protons in liquid water. The corresponding range (*R*), calculated using the plotted *S* values and on the assumption of the continuous slowing down approximation (CSDA), is also plotted.

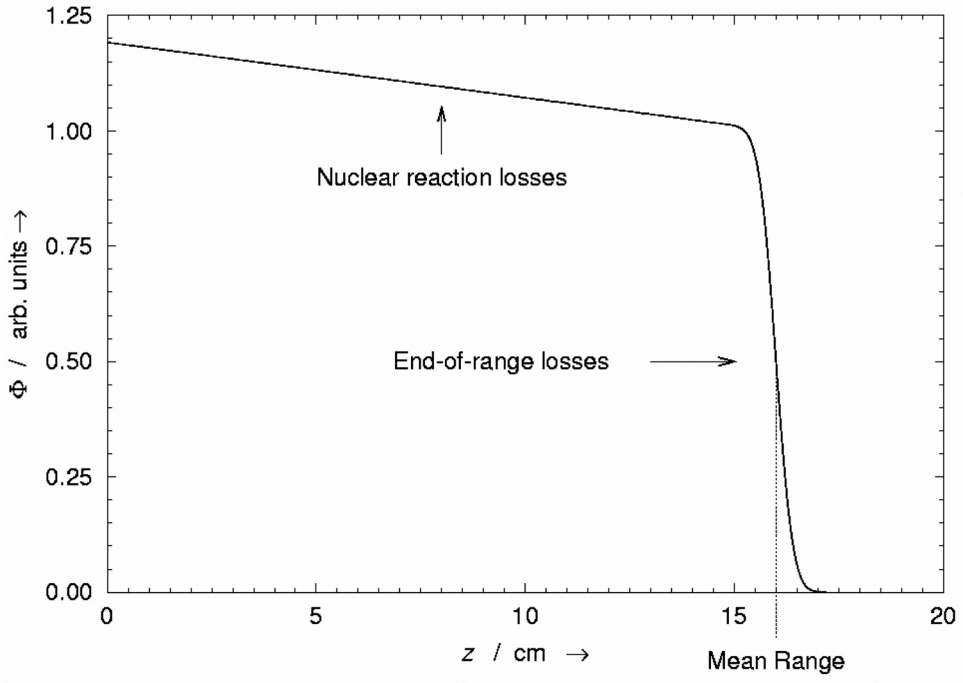

Figure 3.

Relative fraction of the fluence Φ in a broad beam of protons remaining as a function of depth z in water. The gradual depletion of protons from entrance to near the end of range is caused by removal of protons from nuclear reactions. The rapid falloff in the number of protons near the end of range is caused by ions running out of energy and being absorbed by the medium. The sigmoid shape of the distal falloff is caused by range straggling or by stochastic fluctuations in the energy loss of individual protons.

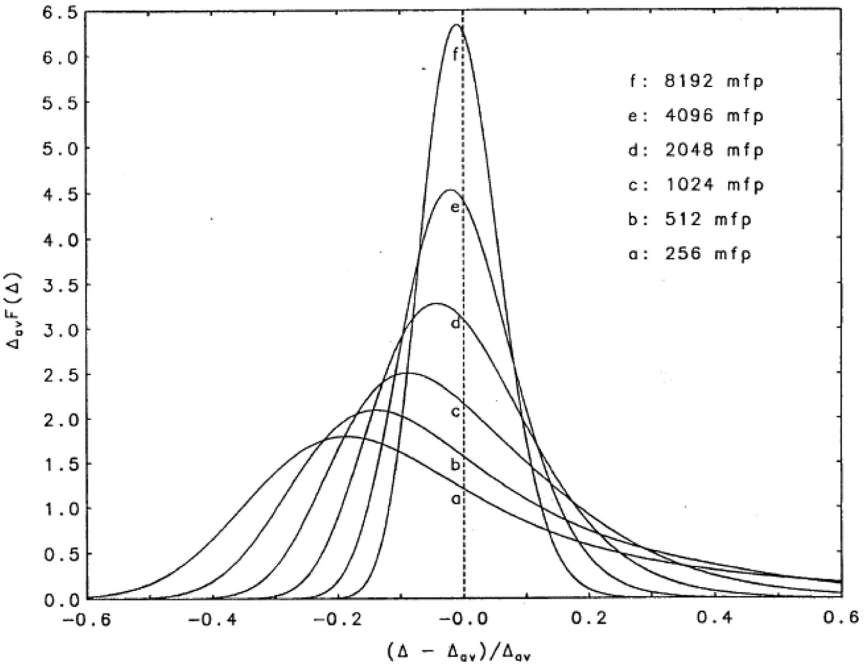

Figure 4.

Energy loss probability density functions (PDF) are plotted for various thicknesses of water absorbers, where the thickness is expressed in units of mean free path (mfp). For visual clarity, the energy-loss PDFs have been scaled on both the abscissa and ordinate. The single event energy loss is expressed as a fraction of the mean energy lost in the entire absorber thickness, or $(\Delta-\Delta_{av})/\Delta_{av}$. Each PDF was scaled so that the integral over all energy-loss values yields unit value. For thin absorbers (curves a-e), the PDFs are broader and asymmetric and are modeled with the Vavilov (1957) or Landau (1944) theories. For thick absorbers (curve f), the PDFs are symmetric and well-approximated with Bohr's theory (1915), *i.e.*, a Gaussian distribution. (ICRU, 1993)

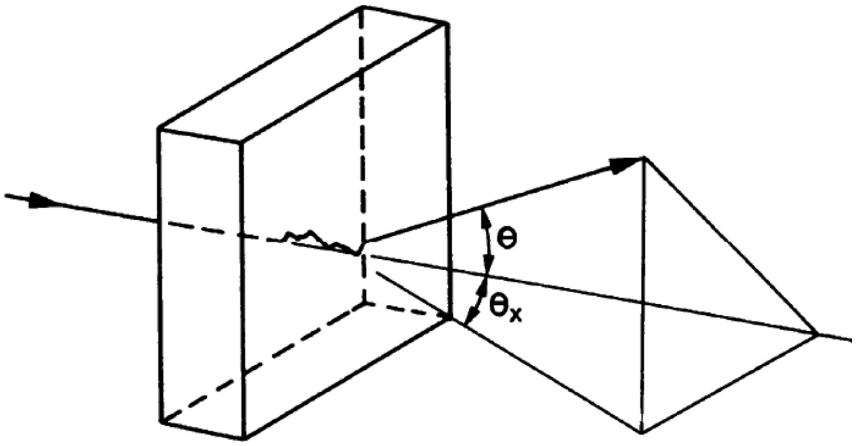

Figure 5.

Schematic diagram showing the trajectory of a proton undergoing multiple Coulomb scattering events. θ is the root mean square (rms) space scattering angle and θ_x is the projected rms scattering angle. (Leo, 1994)

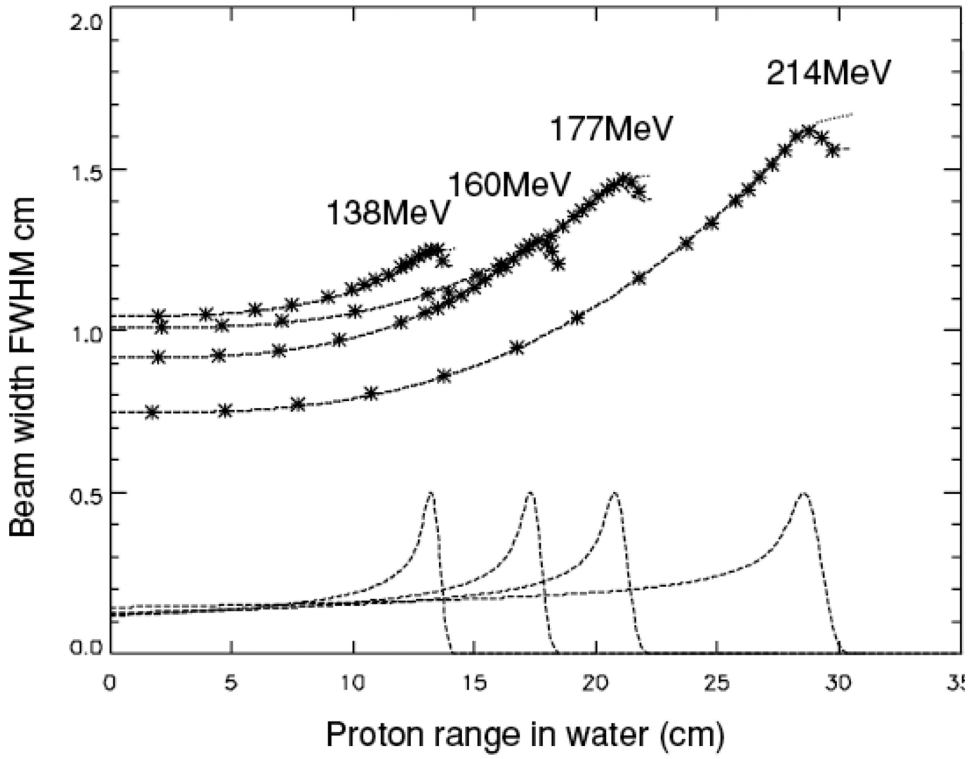

Figure 6.
Broadening of the beam width in water due to multiple Coulomb scattering. (Pedroni *et al*, 2005)

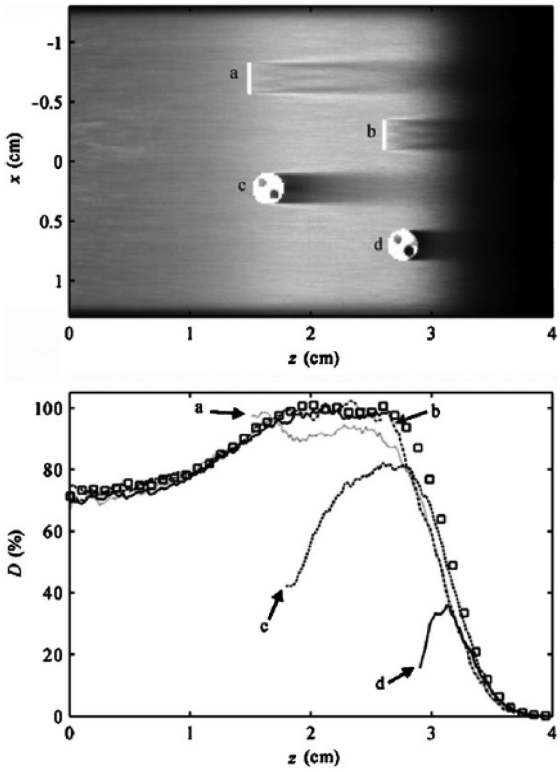

Figure 7.

Small implanted fiducial markers can create clinically significant dosimetric cold spots in proton therapy beams. (Upper) two-dimensional dose distribution as a function of depth in water (*z*) and crossfield position (*x*) from a Monte Carlo simulation of range-modulated proton beam incident on a water phantom containing tantalum localization markers oriented (a, b) parallel to the beam axis and (c, d) perpendicular to the beam axis. The range and modulation width are typical for uveal melanoma treatments. (Lower) simulated absorbed dose (*D*) as a function of depth (*z*) in the water phantom at various off-axis positions. The perturbed depth dose profiles are parallel to the beam axis and pass through the center of markers a–d in the plot above. For visual clarity, portions of the perturbed dose profiles upstream of the markers are not shown. An unperturbed beam is plotted with open squares. (Newhauser *et al*, 2007c)

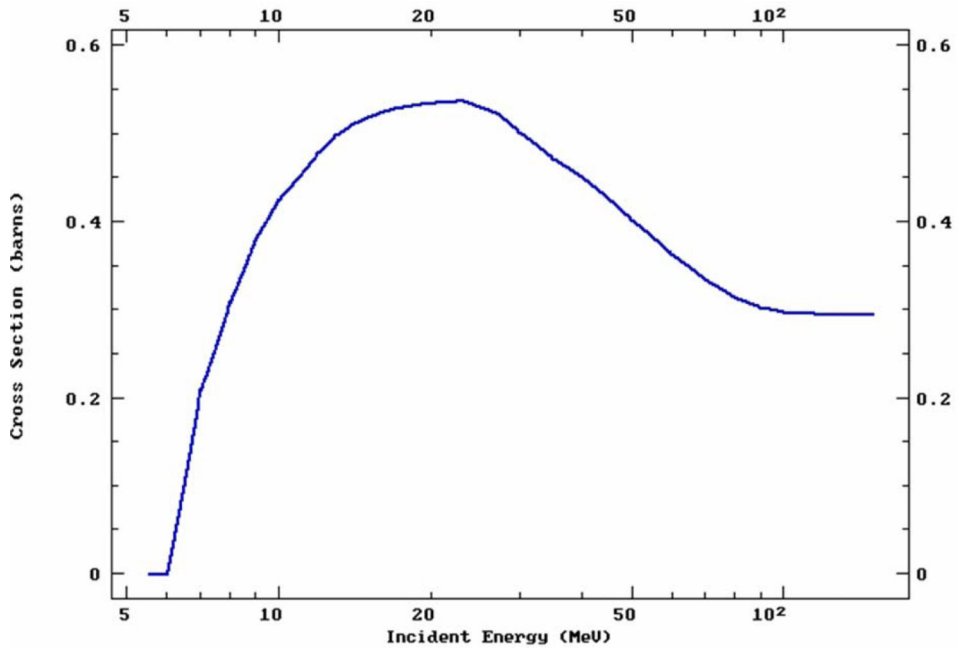

Figure 8.

The total proton-induced non-elastic nuclear reaction versus proton energy, showing a threshold corresponding to the Coulomb barrier at approximately 6 MeV. (ENDF, 2013)

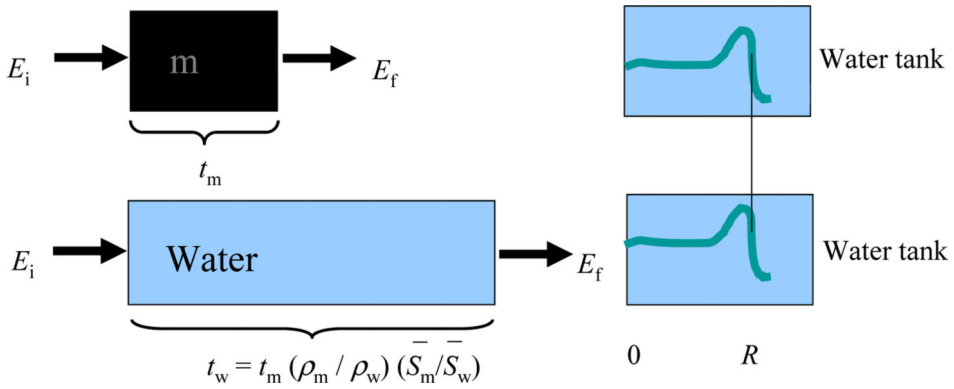

Figure 9.

Schematic illustration of the concept of water equivalent thickness (WET) and how it can be calculated or measured by observing changes in the depth of a proton Bragg peak in a water tank. (Zhang and Newhauser, 2009)

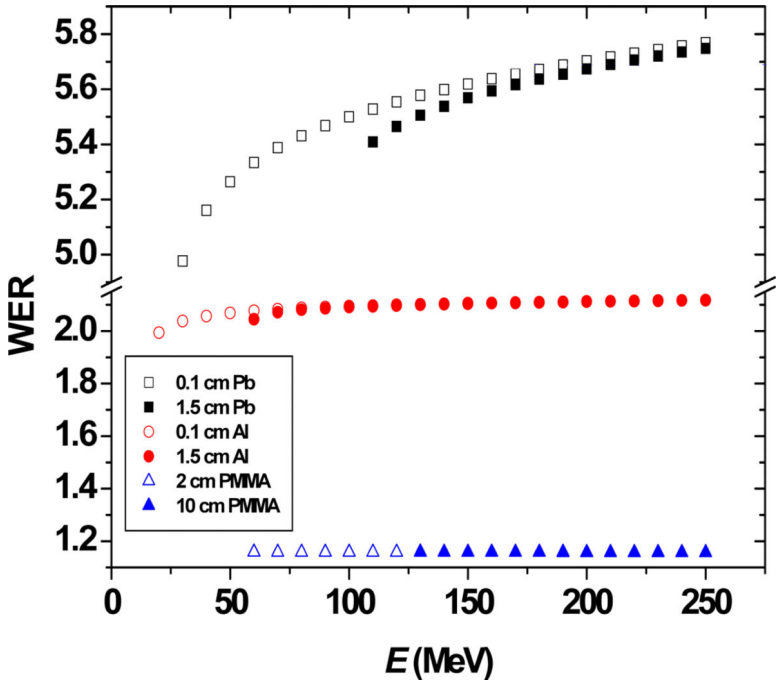

Figure 10.

Calculated water-equivalent ratio (WER) values as a function of proton beam energy. This plot illustrates the dependence of WER value on the target material, the beam energy, and the target thickness. (Zhang and Newhauser, 2009)

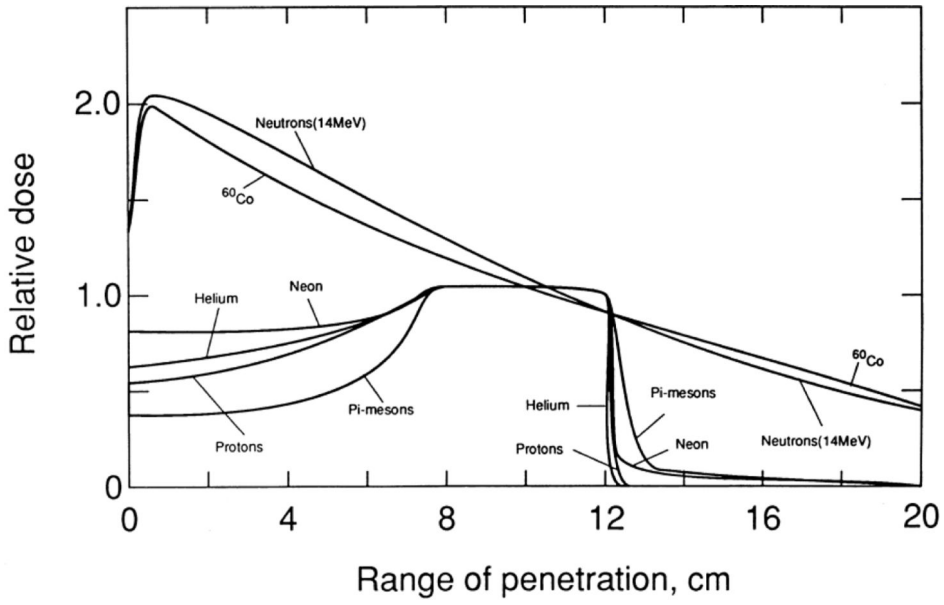

Figure 11.

Central axis depth dose profiles from several particle beams. Note that these distributions are from solitary beams in order to clearly compare the differences in the physical properties of various radiations. The important features are that proton beams offer relatively low entrance dose and virtually no exit dose. However, many clinical treatment techniques exploit multiple field directions to enhance the uniformity of tumor coverage and to spare sensitive healthy tissues. In fact, in some cases proton treatments provide inferior skin sparing to photons and/or inferior target coverage, e.g., because of proton beams' sensitivity to range errors. Nonetheless, beam for beam, proton beams provide excellent tissue sparing, especially beyond the end of range. (Larsson, 1993)

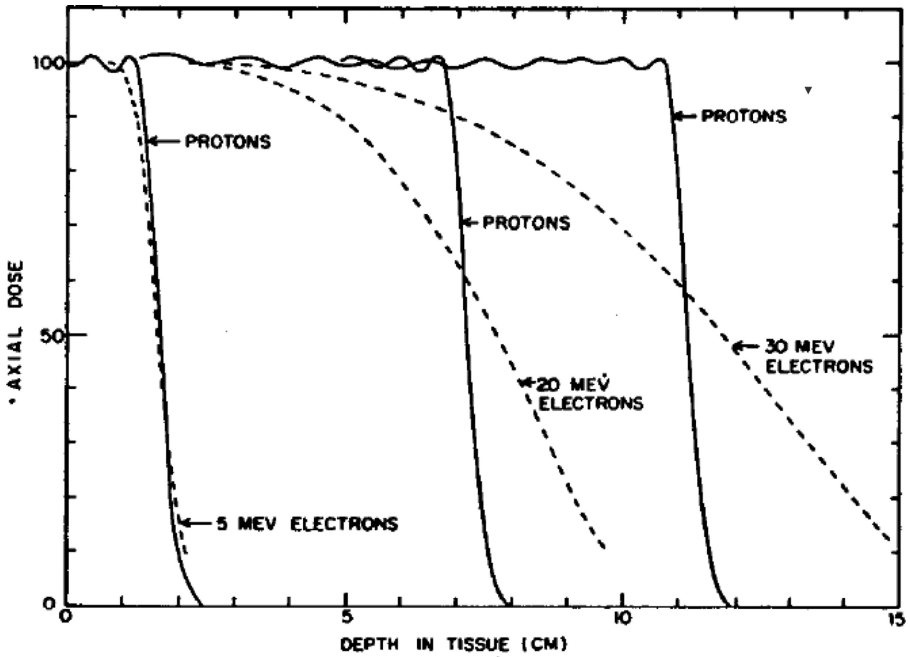

Figure 12.

Comparison of depth-dose curves from proton SOBPs and from electron beams. Because the proton mass is nearly 2000 times that of an electron, proton scattering interactions (individual angular deflections and variations in collisional energy losses) are much smaller, leading to sharper lateral and distal falloff distances. (Koehler and Preston, 1972)

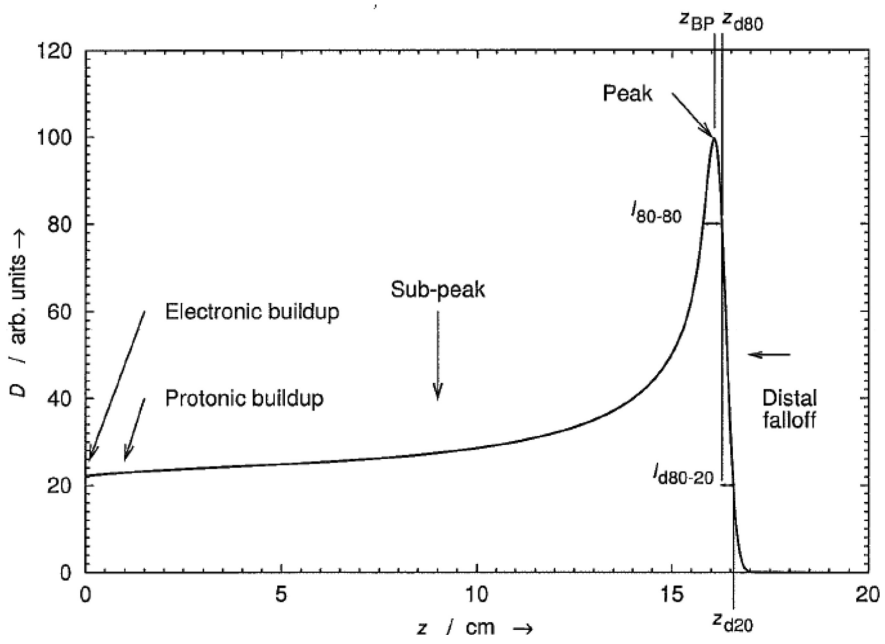

Figure 13.

Absorbed dose *D* as a function of depth *z* in water from an unmodulated (pristine) proton Bragg peak produced by a broad proton beam with an initial energy of 154 MeV. The various regions, depths, and lengths that are labeled are defined in the text. (The electronic buildup is not visible in this plot.) This type of dose distribution is useful clinically because of the relatively low doses delivered to normal tissues in the sub-peak and distal-falloff regions relative to the target dose delivered by the peak.

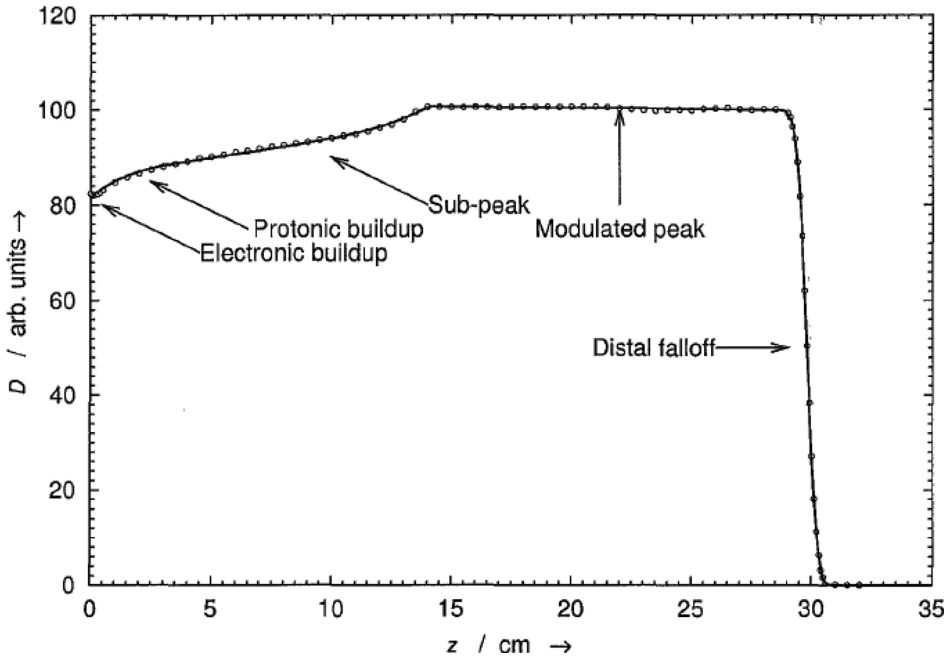

Figure 14.

Absorbed dose *D* as a function of depth *z* in water from a spread-out proton Bragg peak (SOBP). Various locations and regions that are indicated on the plot are defined in the text. This peak was measured with a Markus-type parallel-plate ionization chamber in the Northeast Proton Therapy Center (NPTC) gantry. The measured data are plotted with open circles and the model-fit as a solid line. Note that the electronic buildup region, which spans only a few millimeters, is not visible in this plot.

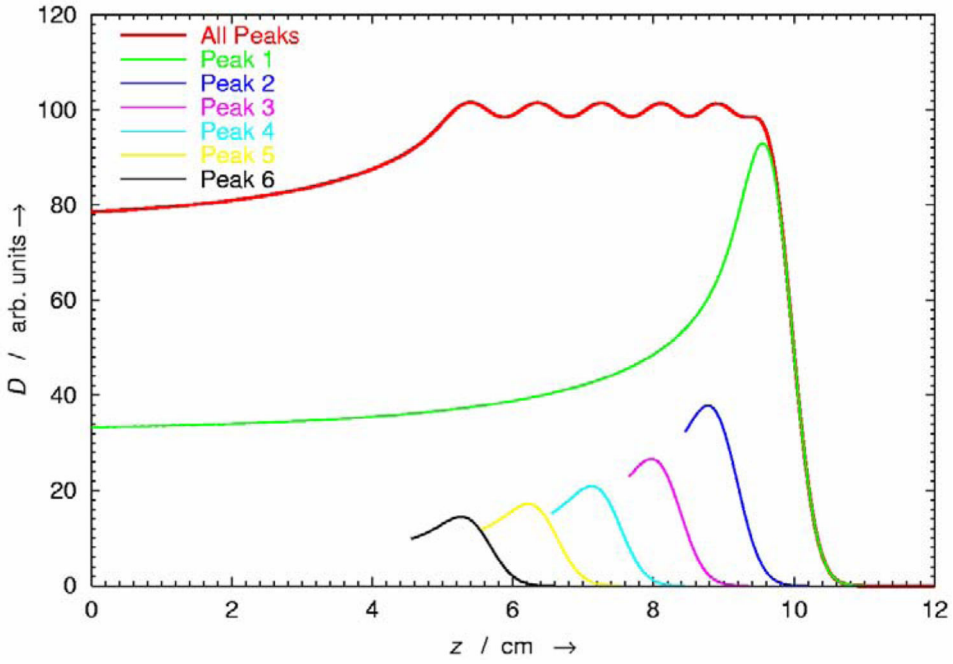

Figure 15.

Absorbed dose *D* as a function of depth *z* in water from a spread-out Bragg peak (SOBP) (uppermost curve) and its constituent pristine Bragg peaks (lower curves; for clarity, all but the deepest pristine Bragg peak are only partly drawn). In many cases, the clinical target volume is larger than the width of a pristine Bragg peak. By appropriately modulating the proton range and fluence of pristine peaks, the extent of the high-dose region can be widened to cover the target volume with a uniform dose.

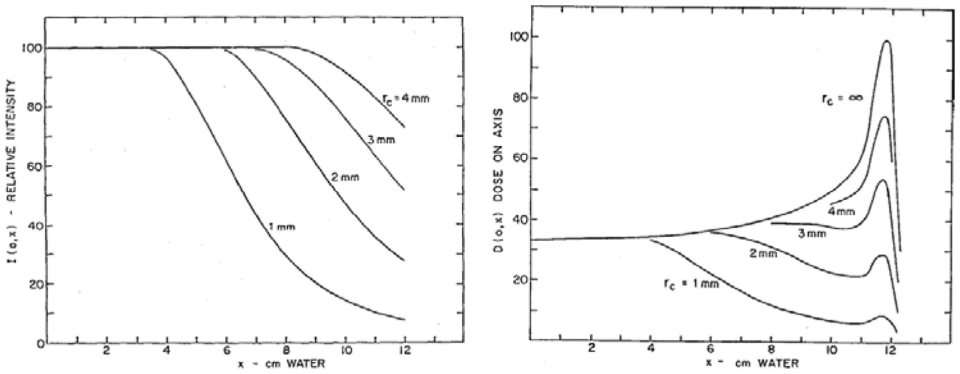

Figure 16.

(Left) Proton fluence $I(0; x)$ along the beam central axis vs. depth x in water. Curves are shown for beams with circular cross sections and radii of 1 mm to 4 mm. Some of the protons are lost because of scattering events that deflect them from the central axis. This is increasingly observed for small beams and at large depths. (Right) The corresponding central-axis absorbed-dose curves. Note how the fluence depletion reduces the absorbed dose at the peak relative to the entrance dose. (Preston and Koehler, 1998)

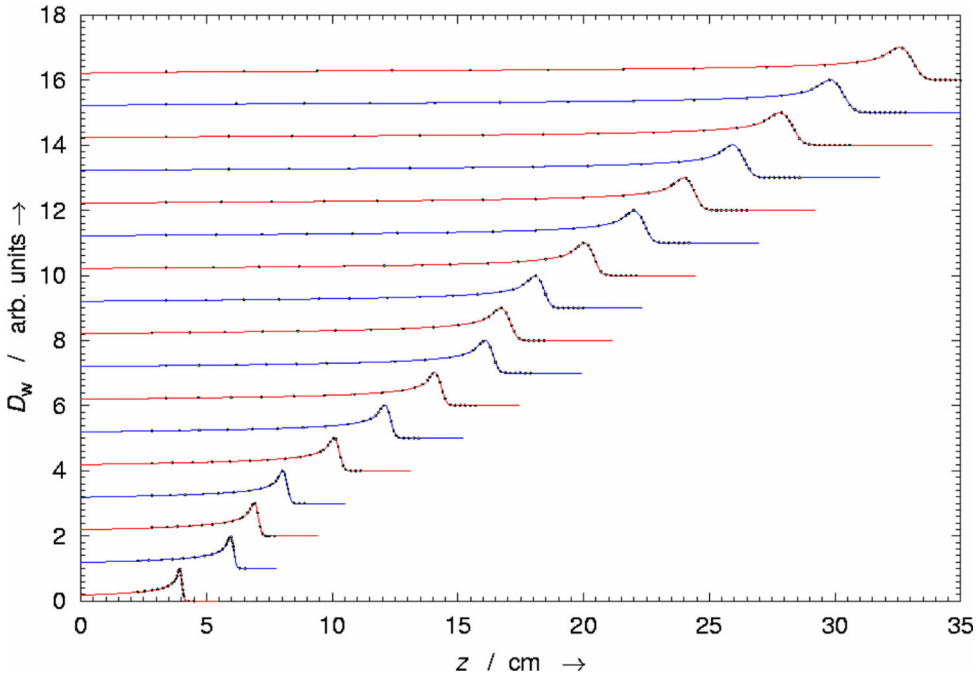

Figure 17.

Absorbed dose *D* as a function of depth *z* in water from unmodulated (pristine) proton Bragg peaks produced by a broad proton beam with an initial energy of up to 235 MeV. With increasing depth, the accumulation of range straggling tends to broaden the peak. Beams that are more penetrating therefore have larger distal falloff distances.

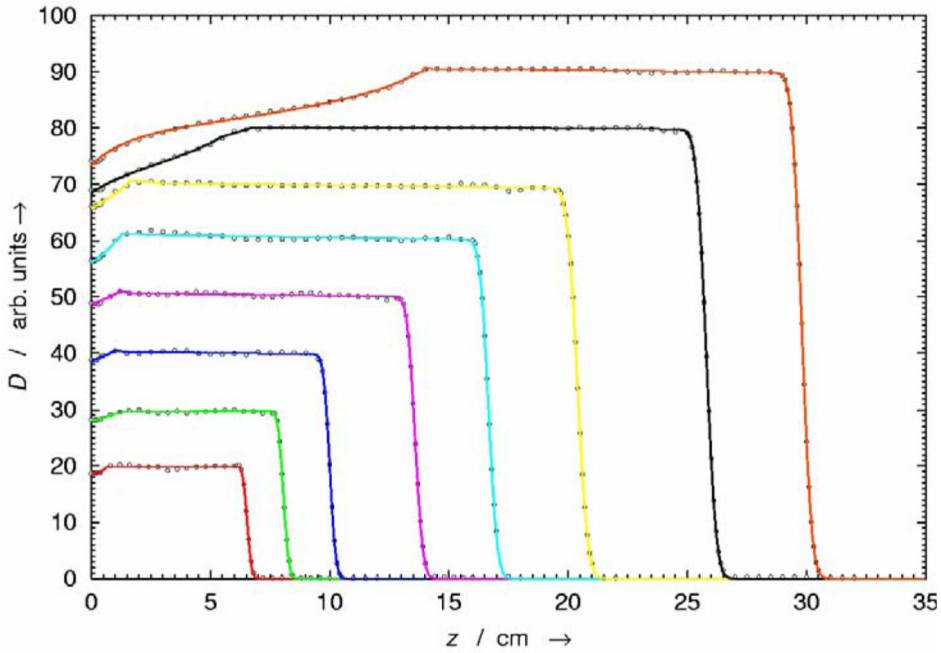

Figure 18.

Absorbed dose *D* as a function of depth *z* in water from various spread out Bragg peaks (SOBP) from the Northeast Proton Therapy Center (NPTC) nozzle. Open- beam central-axis depth-dose curves are plotted for each of the eight range modulator wheel tracks. The experimental values (open circles) are from charge measurements with an air-filled ionization chamber, and the model fits are shown with solid lines. Each range modulation track was designed to work over an interval of proton energies. The flat modulated-peak region was achieved by modulating the proton-beam current synchronously with the modulator wheel rotation.

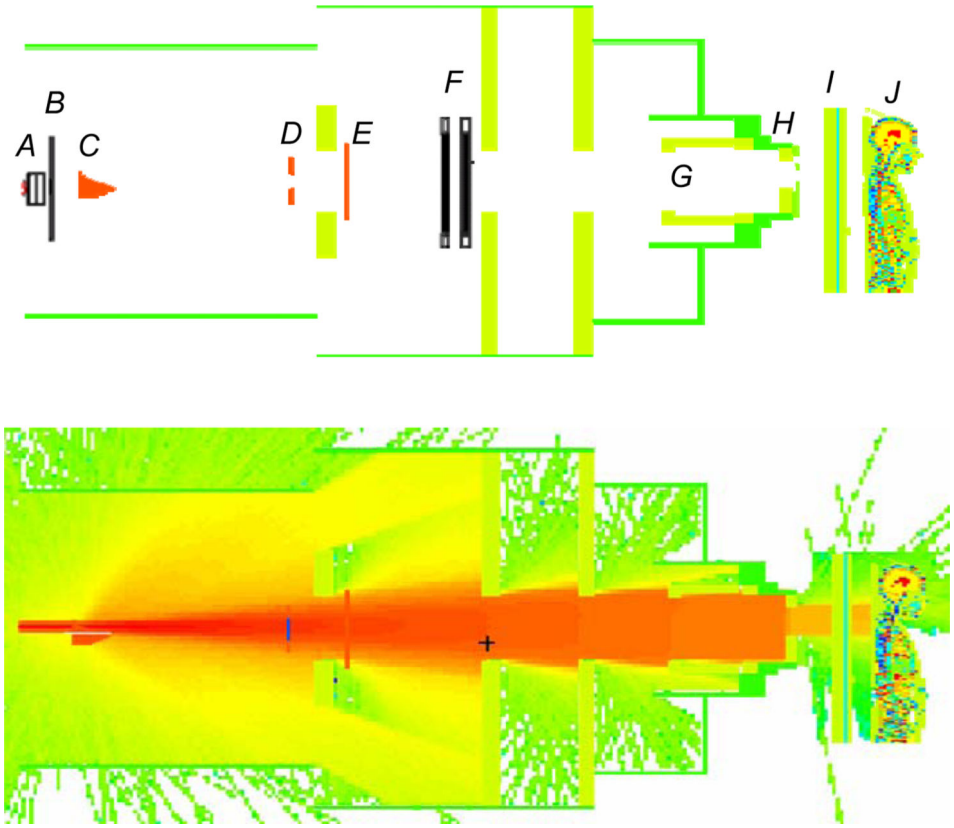

Figure 19.

(Upper) Geometric model of proton therapy unit and the voxelized phantom oriented for the superior spinal proton field. The beam delivery system includes a vacuum window (A), a beam profile monitor (B), a range modulator wheel (C), a second scatterer (D), a range shifter assembly (E), backup and primary monitors (F), the snout (G), the range compensator (H), the treatment couch (I), and the patient (J). (Zhang *et al*, 2013a) (Lower) Simulated proton transport through the proton therapy unit and the patient.

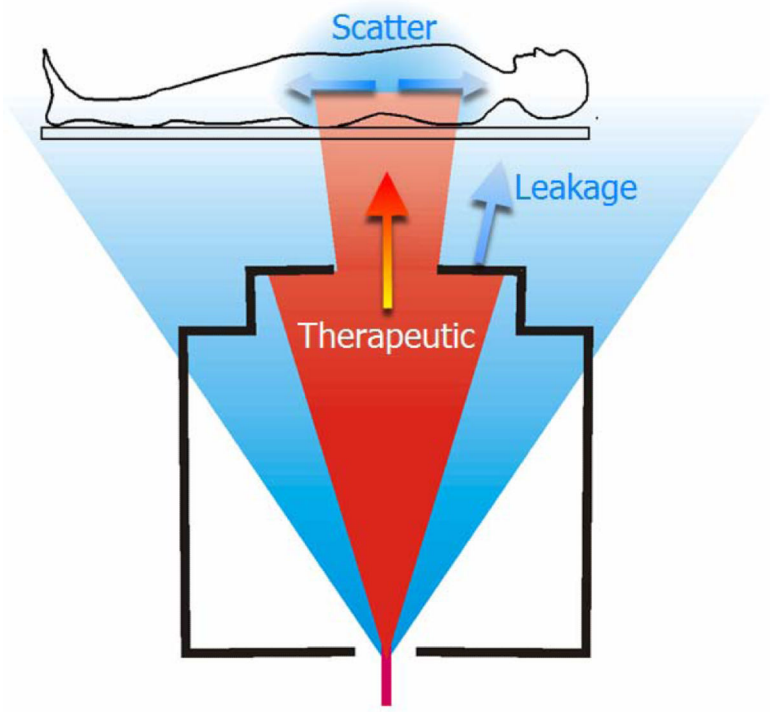

Figure 20.

Schematic diagram of proton beam irradiation of the spine. There are several distinct sources of radiation exposure, including therapeutic protons (red), stray neutrons emanating from the treatment apparatus (blue), and neutrons produced by therapeutic proton radiation inside the body. A small-diameter beam of protons enters the treatment apparatus, which spreads the beam to a clinically useful size and collimates it to spare healthy tissues. The stray neutron is created by proton-induced nuclear reactions inside the treatment unit, some of which leak out and irradiate the patient. The stray radiation exposures provide no therapeutic benefit but increase the predicted risk that a patient will develop a radiogenic side effect, such as a second cancer, later in life. (Newhauser and Durante, 2011)

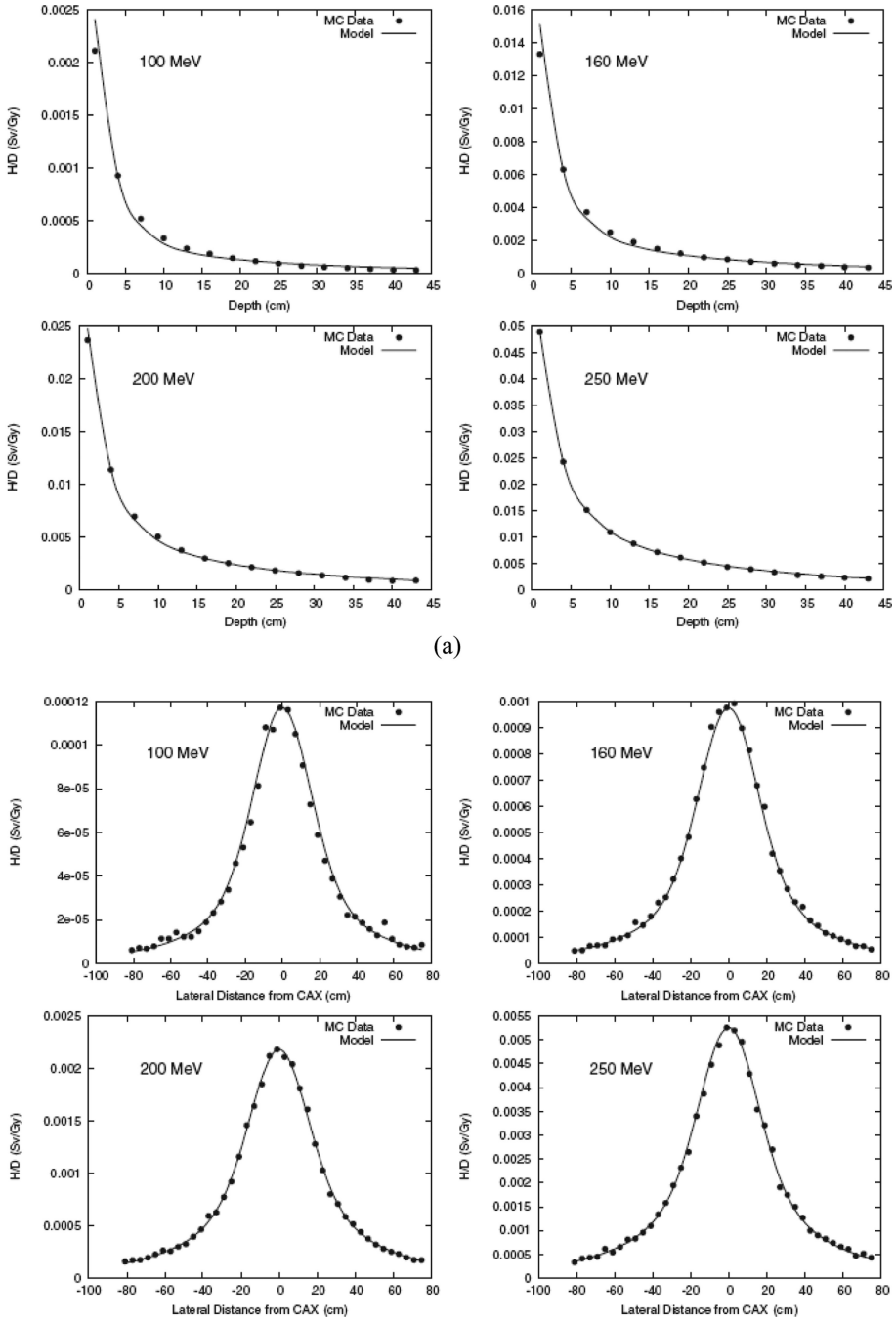

1530

(a)

Figure 21.

Results from Monte Carlo simulations and analytical model predictions of equivalent per therapeutic dose (*H/D*) for proton beams with various energies in the water phantom as a function of vertical depth (a) and lateral distance (b) (Perez-Andujar *et al*, 2013b).

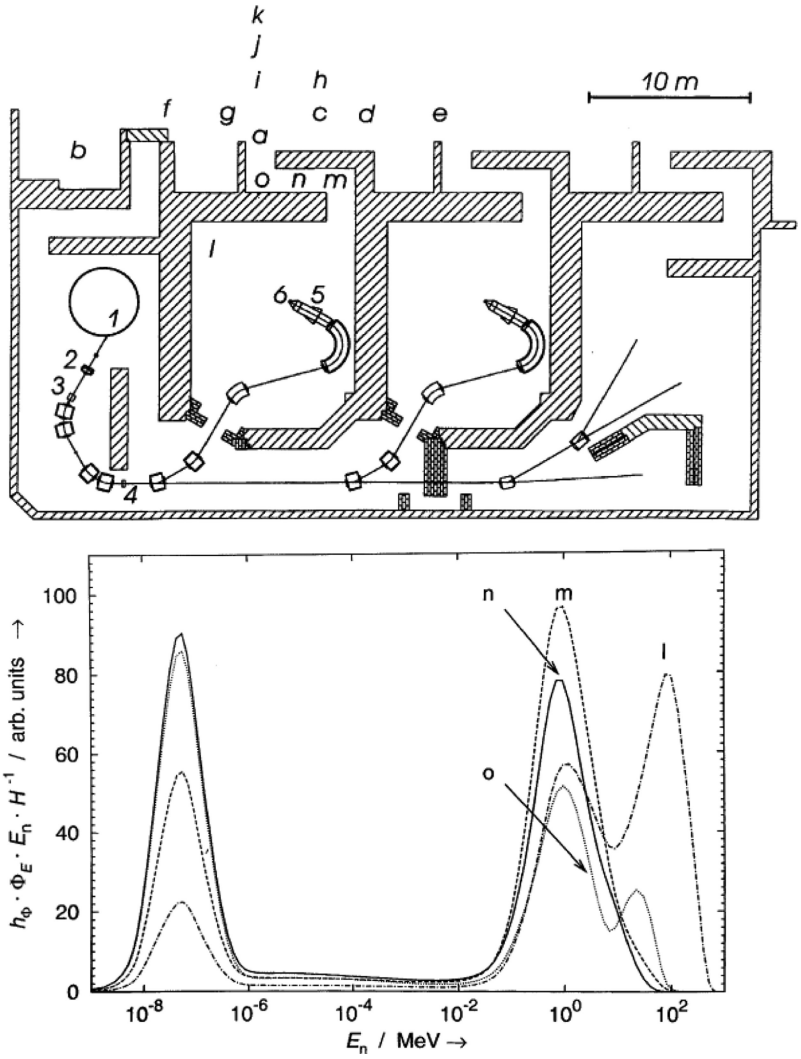

Figure 22.

(Upper) The proton therapy facility treatment level: 235-MeV cyclotron (1), variable-thickness graphite energy degrader (2), momentum analysis magnets (3), slits (4), brass aperture (5), and beamstop at isocenter (6). Plan also shows the main control room (b), treatment room maze exit (m, n, o, a), and various corridors and occupied rooms on the level above (c–k). (Newhauser *et al*, 2002c) (Lower) Calculated neutron dose equivalent spectra at locations l–o in the gantry room and its maze (see Fig. 1) produced by a 235-MeV proton beam. The ordinate corresponds to the product of the neutron fluence-to-dose-equivalent conversion coefficient h_Φ, the neutron spectral fluence Φ_E, and the neutron energy E_n, where the product is normalized to the total neutron dose equivalent H. These spectra reveal differences in the shape due to the relative contributions from peaks due to thermal neutrons, evaporation neutrons, and cascade neutrons. The region between 10^{-6} and 10^{-2} MeV, corresponding to $1/E_n$ behavior of the spectral fluence, contributes relatively little to the total dose equivalent. (Newhauser *et al*, 2002c)

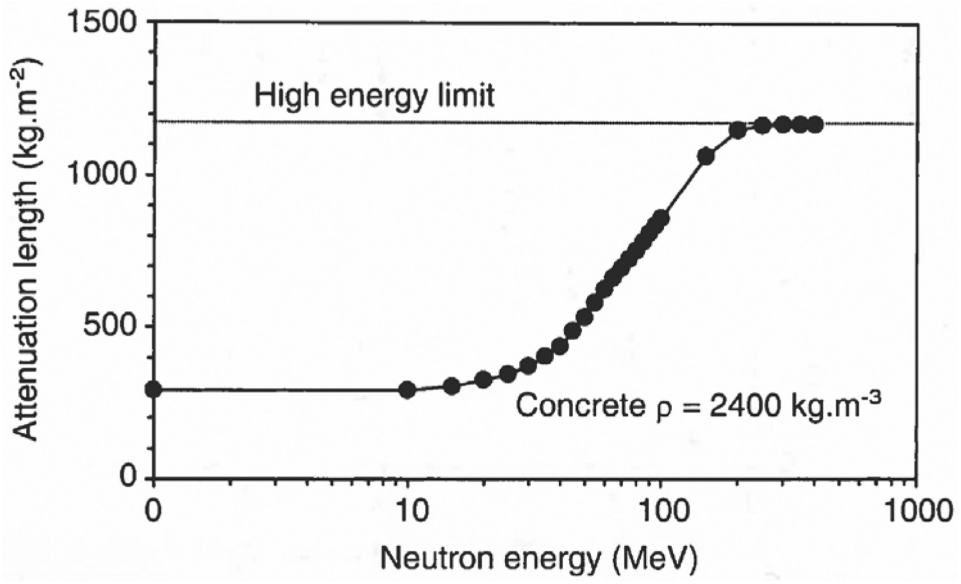

Figure 23.
The attenuation length of neutrons in concrete *versus* neutron energy (Moritz, 2001).

Table 1

Summary of proton interaction types, targets, ejectiles, influence on projectile, and selected dosimetric manifestations

Interaction Type	Interaction Target	Principal Ejectiles	Influence on Projectile	Dosimetric Manifestation
Inelastic Coulomb scattering	Atomic electrons	Primary proton, ionization electrons	Quasi-continuous energy loss	Energy loss determines range in patient
Elastic Coulomb scattering	Atomic nucleus	Primary proton, recoil nucleus	Change in trajectory	Determines lateral penumbral sharpness
Non-elastic nuclear reactions	Atomic nucleus	Secondary protons and heavier ions, neutrons, and gamma rays	Removal of primary proton from beam	Primary fluence, generation of stray neutrons, generation of prompt gammas for *in vivo* interrogation
Bremsstrahlung	Atomic nucleus	Primary proton, Bremsstrahlung photon	Energy loss, change in trajectory	Negligible

Table 2

Common materials (lung substitute plastic, high-density polyethylene (HDPE), water, polystyrene, polymethylmethacrylate (PMMA), polycarbonate resin (Lexan), bone substitute plastic, aluminum, titanium, stainless steel, lead and gold) used in heavy charged particle beams, with their mass densities ρ, values of $(Z/A)_{\text{eff}}$, mole fractions and fitting parameters of α and p for these materials when applying the BK rule (The energies used in the fit were from 10 to 250 MeV).

Material	ρ (g/cm^3)		Mole fraction (%)	α	p
Lung substitute	0.3	0.537	H 55.577, C 32.738, N 0.927, O 7.508, Cl 0.019, Si 0.184, Mg 3.048	8.994×10^{-3}	1.735
HDPE	0.964	0.570	H 66.717, C 33.283	2.541×10^{-3}	1.737
Water	1.0	0.555	H 66.667, O 33.333	2.633×10^{-3}	1.735
Polystyrene	1.06	0.538	H 49.851, C 50.149	2.545×10^{-3}	1.735
PMMA	1.185	0.539	H 53.333, C 33.333, O 13.333,	2.271×10^{-3}	1.735
Lexan	1.20	0.527	H 42.424, C 48.485, O 9.091	2.310×10^{-3}	1.735
Bone substitute	1.829	0.516	H 35.215, C 29.592, N 0.803, O 26.695, Cl 0.16, Ca 7.679	1.666×10^{-3}	1.730
Aluminum	2.698	0.482	Al 100	1.364×10^{-3}	1.719
Titanium	4.519	0.459	Ti 100	9.430×10^{-4}	1.710
Stainless steel	7.85	0.466	C 0.045, N 0.045, Si 0.450, Cr 18.150, Mn 1.250, Fe 71.460, Ni 8.550, Mo 0.050	5.659×10^{-4}	1.706
Lead	11.322	0.396	Pb 100	6.505×10^{-4}	1.676
Gold	19.311	0.401	Au 100	3.705×10^{-4}	1.677